Lattice QCD Calculations of Hadron Spectra and Spectral Functions in the Vacuum and in a Thermal Heat Bath

Dissertation

zur Erlangung des Doktorgrades
an der Fakultät für Physik
der Universität Bielefeld

vorgelegt von
Ines Wetzorke

September 2001

Contents

List of Figures

Introduction

Two aspects of the strong interaction between quarks and gluons are investigated in the present thesis. On the one hand it covers the exploration of the H-dibaryon stability, a six quark state with equal content of the light u, d and s quarks. In cold and dense matter this particle may be formed as a condensate of two Λ baryons due to strong attractive interactions between quarks with maximal symmetry in the flavor, spin and color quantum numbers. On the other hand changes of meson properties in a thermal medium are investigated for a large temperature range. This constitutes the first application of the Maximum Entropy Method in the spectral analysis of thermal meson correlators.

The phase diagram of QCD at vanishing baryon density is already well explored by lattice simulations. Starting at low temperature in the confined hadronic phase and increasing the temperature, a phase transition to the deconfined quark-gluon plasma (QGP) phase can be observed. Recent experiments at CERN SPS gave first evidence that such a new state of almost freely propagating quarks and gluons might exist. In the near future the colliders RHIC in Brookhaven and LHC at CERN will hopefully open the possibility to explore the features of this plasma phase in more detail. Experimental signatures at high temperature like dilepton production rates are directly related to meson spectral functions, in this case to the vector channel. The spectral analysis of meson correlation functions became recently accessible with the Maximum Entropy Method (MEM), which permits to study the temperature dependent modifications of the spectral shape from first principles.

A similarly detailed theoretical understanding of the high density region of the QCD phase diagram at low temperature is of physical relevance in heavy ion collisions as well as in astrophysics. An interesting phase structure is expected to arise in this case from quantum statistic effects, which e.g. favor bosonic forms of matter over fermionic states. At high densities the $SU(3)$ color symmetry might be spontaneously broken, giving rise to a color superconducting phase characterized by the formation of diquark condensates. Furthermore dibaryons or even larger quark clusters may play an important role as Bose condensates in hypernuclear matter at increasing density. In the current analysis previously obtained diquark correlators are explored more precisely with the Maximum Entropy Method, whereas the stability of larger quark clusters is examined in a detailed analysis of the smallest object of this kind, the H-dibaryon.

The investigation of these phenomena in lattice QCD is at present restricted to simulations at an average baryon density of zero, since the probabilistic interpretation of the QCD partition function in the path integral representation breaks down for non-zero chemical potential. Such calculations provide nevertheless an insight to the dominant quark-quark interactions in this region.

In the first chapter QCD is described as $SU(3)$ gauge theory in the Euclidean path integral formalism. The current knowledge about the QCD phase diagram at finite temperature and density is summarized with the focus on the changes of hadronic properties at the different phase boundaries. After a short introduction to the relevant aspects of strange matter in the cold and dense region of the phase diagram the previous experimental and theoretical searches for a stable H-dibaryon are reviewed.

The second chapter describes the lattice regularization of the Euclidean path integral which includes the specification of the improved discretizations of the gauge and fermion action used for the Monte Carlo simulation in the present thesis. In the following some numerical details of the lattice calculation are explained, which includes the generation of gauge field configurations, the inversion of the fermion matrix, the gauge fixing procedure for gauge-variant observables as well as the error analysis for correlated data sets.

The lattice study of the strange hadron spectrum and the investigation on the stability of the H-dibaryon is the content of the third chapter. After a few general considerations about the hadron multiplet structure and the underlying interactions between quarks the lattice setup is illustrated with the appropriate observables for the investigated hadron channels. Moreover the extrapolation of the particle masses to physical quark masses is explained. Finally results obtained on four different lattice sizes are presented for several strange hadron masses as well as for the H-dibaryon mass.

The fourth chapter gives an introduction to the Maximum Entropy Method and describes the actual numerical implementation in the QCD context. After the exploratory study of the (in-)dependence of the approach under changes of the input parameters the spectral analysis is performed for meson and diquark correlation functions at zero temperature. Furthermore the applicability of the approach at finite temperature is tested with free meson spectral functions. Finally, a lattice investigation of the scalar, pseudo-scalar and vector meson correlators at finite temperature and their spectral analysis with the Maximum Entropy Method is presented.

Chapter 1

QCD and the Phase Diagram

The starting point of the present investigation is the formulation of QCD as a non-abelian $SU(3)$ gauge theory, which is presented in the first section 1.1. The current knowledge about the QCD phase diagram and the properties of hadronic matter at finite temperature are summarized in section 1.2, while the rich phase structure at finite density is described in section 1.3. This paragraph is followed by some considerations about the H-dibaryon in the context of strange quark matter and a short review of previous investigations on the stability of such a particle in section 1.4.

1.1 Quantum Chromo Dynamics

In the framework of the Standard Model of elementary particle physics **Quantum Chromo Dynamics (QCD)** is the fundamental theory of the strong interaction. As a non-abelian gauge theory it is locally gauge invariant under $SU(3)$ color transformations. The basic constituents, namely the two light u and d quarks, the s quark with intermediate mass as well as the heavier c, b and t quarks interact through the exchange of gluons, the gauge bosons of the theory. This is reflected in the fermionic and gluonic part of the gauge-invariant QCD Lagrangian for N_f quark flavors with mass m_f

$$\begin{aligned} \mathcal{L}_{QCD}(x) &= \mathcal{L}_F(x) + \mathcal{L}_G(x) \\ \mathcal{L}_F(x) &= \sum_{f=1}^{N_f} \bar{\Psi}^f_\alpha(x)(i\gamma^\mu D_\mu - m_f)_{\alpha\beta}\Psi^f_\beta(x) \\ \mathcal{L}_G(x) &= -\frac{1}{2}\,\mathrm{Tr}\, F_{\mu\nu}(x)F^{\mu\nu}(x), \end{aligned} \tag{1.1}$$

where the Greek letters denote the Dirac indices of the quark fields Ψ. The covariant derivative D_μ as well as the field strength tensor $F_{\mu\nu}$ involve the bare gauge coupling g

$$\begin{aligned} D_\mu &\equiv \partial_\mu + igA_\mu(x) \\ F_{\mu\nu}(x) &\equiv \partial_\mu A_\nu(x) - \partial_\nu A_\mu(x) + ig\,[A_\mu(x), A_\nu(x)]. \end{aligned} \tag{1.2}$$

The gauge fields A_μ are related to the $N_c^2 - 1 = 8$ generators λ^a of the gauge group $SU(3)$

$$A_\mu(x) = \sum_{a=1}^{8} A_\mu^a(x)\frac{\lambda^a}{2}. \tag{1.3}$$

Due to the non-abelian character of QCD the gauge fields do not commute, which is manifest in the self-interaction between the gluons.

The quantization of the field theory is realized in the Euclidean path integral formulation. The QCD partition function explicitly depends on the volume and the temperature

$$Z^E(V,T) = \int \mathcal{D}A\mathcal{D}\Psi\mathcal{D}\bar{\Psi}\; e^{-S^E_{QCD}(V,T,A,\Psi,\bar{\Psi})}, \tag{1.4}$$

while a possible dependence on a non-zero chemical potential μ is neglected herein. The thermal expectation value of an observable $\mathcal{O}$ in the Euclidean representation can be calculated as follows

$$\langle\, \mathcal{O} \,\rangle = \frac{1}{Z^E(V,T)} \int \mathcal{D}A\mathcal{D}\Psi\mathcal{D}\bar{\Psi}\; \mathcal{O}(A,\Psi,\bar{\Psi})\; e^{-S^E_{QCD}(V,T,A,\Psi,\bar{\Psi})}. \tag{1.5}$$

The Euclidean action S^E_{QCD} at finite temperature is defined through the integral over the QCD Lagrangian in imaginary time τ

$$\begin{aligned} S^E_{QCD}(V,T) &= \int_0^{1/T} d\tau \int_V d^3x\; \mathcal{L}^E_{QCD} \qquad \text{with} \\ \mathcal{L}^E_{QCD} &= \sum_{f=1}^{N_f} \bar{\Psi}^f_\alpha(x)(\gamma^\mu_E D_\mu + m_f)_{\alpha\beta}\Psi^f_\beta(x) + \frac{1}{2}\,\mathrm{Tr}\; F_{\mu\nu}(x)F^{\mu\nu}(x). \end{aligned} \tag{1.6}$$

The Euclidean γ matrices, which fulfill the anti-commutation relation $\{\gamma_\mu, \gamma_\nu\} = 2\delta_{\mu\nu}$, are given in appendix A. Note that the index E will be omitted from now on, since only quantities in the Euclidean metric are utilized.

Apart from the local $SU(3)$ color gauge symmetry, the QCD Lagrangian possesses additional global symmetries. In the massless continuum theory, the chiral symmetry for N_f quark flavors is described classically by $SU_L(N_f) \times SU_R(N_f) \times U_V(1) \times U_A(1)$. The axial $U_A(1)$ symmetry is explicitly broken already at quantum level, whereas the preserved $U_V(1)$ symmetry implies the global baryon number conservation due to Noether's Theorem. The chiral $SU_L(N_f) \times SU_R(N_f)$ symmetry for the two lightest quark flavors $m_{u,d} \simeq 0$ is spontaneously broken at zero temperature, which is associated with the appearance of $(N_f^2 - 1)$ nearly massless Goldstone bosons, the pseudo-scalar isospin triplet (π^+, π^0, π^-).

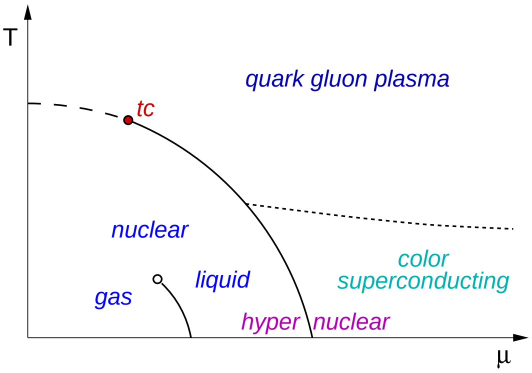

Figure 1.1: Schematic QCD phase diagram.

The strong interaction is characterized by two general features: Quarks and gluons are very weakly coupled at small distances and thus behave as freely propagating particles (**asymptotic freedom**), whereas the coupling gets strong for large separations and small momenta. As a consequence quarks have only been observed in hadronic bound states (**confinement**). These properties are reflected in our basic picture of the QCD phase diagram in figure 1.1. When increasing the temperature T and/or the baryon chemical potential μ the non-perturbative structure of the QCD vacuum, which is characterized by confinement and chiral symmetry breaking, gets lost and eventually will end in an asymptotically free quark gluon plasma.

1.2 Phenomena at Finite Temperature

In lattice simulations the phase diagram has quite successfully been explored by varying the temperature T at vanishing baryon chemical potential μ. The chiral symmetry is broken in the confinement phase at low temperature, where the quarks and gluons form bound states within a hadron gas. A phase transition to a plasma phase with restored chiral symmetry is observed by increasing the temperature. Strictly speaking, one has to distinguish between the deconfinement and the chiral symmetry restoring phase transition. In the quenched limit with infinite quark masses the Polyakov loop expectation value is an order parameter for the deconfinement transition, whereas the chiral condensate is the order parameter for the chiral symmetry restoration in the limit of vanishing quark masses. In QCD, where the fermions belong to the fundamental representation of the $SU(3)$ color group, these two phase transitions seem to occur simultaneously at a common critical temperature T_c [1]. However, they are well separated in theories where the fermions belong to the adjoint representation [2].

The critical temperature as well as the order of the phase transition depend on the number of colors N_c and quark flavors N_f, respectively. Furthermore, the occurrence of a transition depends on the magnitude of the quark masses. In the quenched theory ($N_c = 3$, $N_f = 0$) with infinitely heavy quarks the deconfinement phase transition is first order [3] and occurs at about T_c=270 MeV [4]. For two massless quark flavors, the chiral phase transition is second order at $T_c \simeq$175 MeV [5]. It is expected to change with increasing chemical potential to first order at a tricritical point (tc) as indicated in figure 1.1. Introducing a small quark mass $m_{ud} > 0$, the second order transition turns into a smooth crossover and the tricritical point becomes a critical endpoint, which may be determined quantitatively in heavy ion collision experiments [6]. A more realistic strange quark mass $m_s < \infty$ results in a shift of the tricritical point towards the temperature axis. As a consequence the chiral phase transition becomes first order even at zero chemical potential in the limit of three massless quark flavors. The critical temperature $T_c \simeq 155$ MeV in the case $N_f = 3$ was obtained in a recent lattice simulation [5].

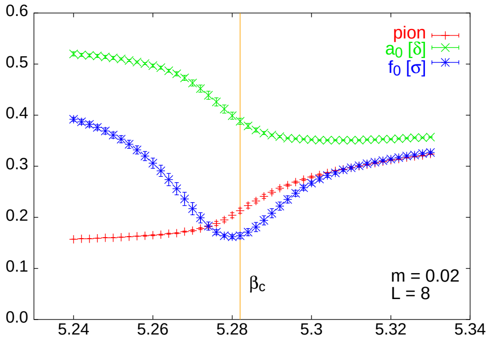

Figure 1.2: $U_A(1)$ and chiral symmetry restoration of (pseudo-)scalar mesons [7].

The light hadron spectrum is sensitive to the changes of the chiral condensate and the chiral symmetry restoration in the vicinity of the critical temperature. In the chirally symmetric phase above the critical temperature the pseudo-scalar meson is no longer a Goldstone boson. For $N_f = 2$ the thermal correlation function in this quantum number channel should coincide with that of the isospin singlet scalar meson σ. Such a behavior is similarly anticipated for the (axial-) vector mesons a_1 and ρ. On the other hand an effective restoration of the $U_A(1)$ symmetry would involve a degeneracy of the flavor triplet (pseudo-)scalar π and δ as well as of the singlet σ and η' meson correlators [8]. Figure 1.2 shows results of (pseudo-)scalar susceptibilities, i.e. integrated meson correlation functions in the Euclidean time interval [0,1/T] obtained in a lattice simulation with staggered fermions [9] (similar in [10]). The inverse of these susceptibilities may be viewed as the square of effective thermal masses. The π and σ meson masses become degenerate near T_c, while the δ approaches the other masses slowly with increasing temperature, which implies that the $U_A(1)$ symmetry remains broken at T_c. This behavior was confirmed by recent lattice simulations with overlap [11] and domain wall fermions [12].

So far information on thermal masses has either been obtained from susceptibilities like those in figure 1.2 or from spatial correlators which define screening masses. Both approaches do not yield direct information about thermal hadron masses. In particular the effective masses extracted from susceptibilities have no well-defined counterpart in the continuum limit. In order to get access to the temperature dependence of pole masses one has to analyze thermal correlators in Euclidean time. Information on masses is then encoded in the respective spectral functions, where a dominant ground state mass is manifest as a sharp δ-function like peak. Moreover, the spectral representation allows the distinction between pole and continuum contributions, which becomes increasingly important at finite temperature. A detailed investigation of hadronic correlators and spectral functions at several temperatures below and above the phase transition is presented in chapter 4.

Previous lattice simulations with staggered [13] as well as Wilson fermions [14] gave no evidence for significant changes of the meson masses below the critical temperature. Due to the limited extent of the lattice in the Euclidean time direction $\tau \in [0, 1/T]$ most of the mentioned studies investigated only spatial correlation functions. The screening and pole masses are expected to coincide below the critical temperature, if the $T = 0$ dispersion relation still holds true at $T < T_c$. At temperatures well above T_c the behavior of the spatial meson correlators can be explained by the propagation of two weakly interacting quarks in the plasma. Thus the screening masses will approach the lowest Matsubara frequency $2\pi T$, induced by the anti-periodic boundary conditions for fermions in the temporal direction. Nevertheless, collective phenomena may still be present in the plasma phase for temperatures close to T_c [15].

In a recent simulation with Wilson fermions on anisotropic lattices [16] it has been observed that the pole masses are considerably smaller than the screening masses above T_c, which led to the interpretation that mesonic excitations or metastable bound states persist up to at least 1.5 T_c. These conclusions, however, have been obtained by using standard exponential fitting procedures, which are suitable at zero temperature. At $T > 0$ such an approach should be applied carefully, because the continuum contributions may have a considerable influence on the resulting pole masses in the short temporal direction. Since the spectral representation allows to distinguish between the different contributions, the analysis of correlation functions with the Maximum Entropy Method (MEM) [17, 18] will provide new insight in the temperature dependence of pole masses. A first application of MEM for pseudo-scalar, scalar and vector meson correlators at finite temperature is presented in section 4.7.

1.3 Phases at Finite Density

Now the focus is on the conjectured phase diagram (fig. 1.1) at low temperatures and high densities. Moving away from the temperature axis towards larger densities an additional first order phase transition line is observed, separating the hadron gas with zero baryon density from a nuclear liquid phase with density $n_0 = 0.17/fm^3$. At zero temperature this jump in the density is expected to occur at a baryon chemical potential of the nucleon mass minus its binding energy [19]. The endpoint of this first order phase transition line was estimated experimentally at GSI [20] to lie in the region of 0.15-0.3 times the nuclear density and a temperature of $\mathcal{O}(10\text{ MeV})$, which is characteristic for the binding energy of nuclei.

At even higher densities an additional color superconducting phase is indicated in figure 1.1. In the theory of superconductivity the BCS-mechanism [21] leads to the formation of a Bose condensate of electron Cooper pairs for an arbitrarily weak attractive interaction. A phonon-induced interaction is needed in this case to reduce the repulsive electrostatic force between the electrons. In QCD the occurrence of a BCS-like mechanism is even more straightforward. Since quark momenta are large in the region of high density, asymptotic freedom implies that the coupling between the particles is weak. Unlike in the case of electrons the fundamental interaction between quarks is already attractive for u and d quarks with different color and anti-parallel spin. This can be deduced from the perturbative one-gluon-exchange [22] as well as from the instanton liquid model [23, 24]. At high densities it is thus energetically favorable for the weakly coupled quarks to form a diquark Bose condensate. In this color superconducting phase the local $SU(3)$ color gauge symmetry is broken to $SU(2)$ [25]. Since the chiral symmetry is restored and none of the global symmetries of QCD is broken, no order parameter distinguishes the two flavor color superconducting phase from the quark gluon plasma.

In the case of three massless quarks such diquark condensates cannot be flavor singlets. In addition to a condensate of ud quark pairs also us and ds Cooper pairs may occur, which are only invariant under a correlated color/flavor symmetry. Such a superconducting color-flavor locked (CFL) phase [26] is thus characterized by the broken baryon number and chiral symmetry

$$SU(3)_C \times SU(3)_L \times SU(3)_R \times U_V(1) \longrightarrow SU(3)_{C+L+R}.$$

This allows a distinction to the other phases, since the breaking of global symmetries provides an order parameter for the phase transition. Such an order parameter for the baryon number symmetry breaking would carry the quantum numbers of the H-dibaryon [27]. The symmetries of the CFL phase are the same as expected for hypernuclear matter, where hyperons (strange baryons) are expected to pair into a SU(3) flavor singlet state like the H-dibaryon ($\Lambda\Lambda$), ($\Sigma\Sigma$) or ($N\Xi$). Different from the phase transition at high temperatures and low baryon density where many new degrees of freedom arise, their number may remain the same with increasing baryon density at low temperature. The hadronic degrees of freedom might be followed continuously from hypernuclear matter to the CFL phase of quark matter without a phase transition. Such a behavior has been recently described as quark-hadron continuity [27].

1.4 Strange Matter and the H-Dibaryon

A somewhat different context, in which the H-dibaryon might be important, is the physics of strange quark matter [28, 29]. At very high density and low temperature the properties of quarks and gluons in the deconfined phase are expected to differ from those of the quark gluon plasma at high temperature, therefore this state was given the name quark matter. Since the pressure gets higher at increasing density, the quarks have to occupy higher energy states due to the Pauli exclusion principle. Then it could be energetically favorable for u and d quarks to convert into s quarks via weak interaction processes. After such an equilibration process of the quark flavor content a finite number of strange quarks is left, which motivated the name strange quark matter, or simply strange matter. It is suspected that such a state of matter could exist in the core of neutron stars, where ordinary quark matter built from neutrons may be converted to strange quark matter under the influence of the enormous pressure [30].

It was suggested by Witten in 1984 [31] that strange matter might be more stable than ordinary nuclei. Strange matter could exist in small lumps called strangelets, having lower energy than a nucleus with the same amount of quarks. This was the starting point for the disaster scenarios for the new relativistic heavy ion collider (RHIC) in Brookhaven. Concerns were raised that a transition to a lower vacuum state could be initiated due to the formation of stable strangelets. The arguments against such a scenario were summarized in a recent review article [32] and were not proven false by the actual experiments at RHIC in the meanwhile.

In the context of strange quark matter the H-dibaryon is the lightest possible strangelet [28, 29]. Such a six quark state (*udsuds*) is the lightest SU(3) flavor singlet state with spin zero, strangeness -2 and $J^P = 0^+$. It has the smallest energy per baryon number, since both color and spins cancel pairwise to the greatest possible extent. A stable H-dibaryon was first predicted in 1977 by Jaffe [33] in a bag model calculation. He obtained a mass of m_H=2150 MeV, which is 81 MeV below the $\Lambda\Lambda$ threshold for strong decay. This observation had inspired many theoretical and experimental searches for a stable H-dibaryon during the following decades.

Various QCD motivated models were applied in the theoretical search for a stable H-dibaryon. Calculations were performed in the bag model, the non-relativistic quark cluster model, the Skyrme model and with QCD sum rules. References on all of these investigations can be found in a recent review article [34]. In general perturbative calculations of the hadron mass splittings are based on spin-dependent quark-quark interactions, which includes color-spin coupling for the one-gluon-exchange (OGE) and flavor-spin coupling for instanton induced interactions (III) and Goldstone-boson-exchange (GBE). This is illustrated more explicitly in the first section of chapter 3.

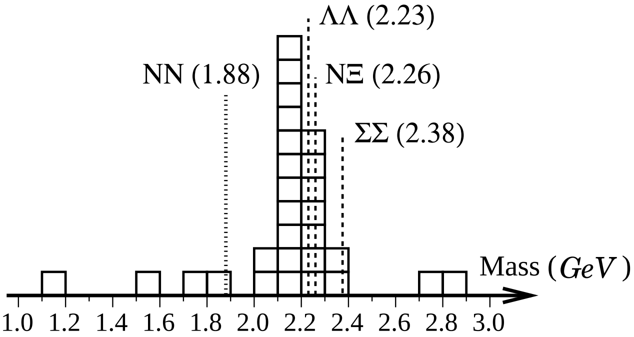

Figure 1.3: Theoretical predictions of the H-dibaryon mass [35].

Combining the previous theoretical investigations a slightly bound or unbound H-dibaryon is predicted. This is visualized in figure 1.3, where the thresholds for strong $(\Sigma\Sigma, N\Xi, \Lambda\Lambda)$ and weak decay (NN) are indicated in addition. In the case of a bound state a definite confirmation could be expected from experimental searches in a range of a few hundred MeV below the 2231 MeV $\Lambda\Lambda$ threshold for strong decay. The H-dibaryon may be produced in several processes, such as heavy ion collisions, (K^-, K^+) reaction or Ξ^--capture. The presence of a bound state can only be detected from the products of the weak decay, for example $H \to \Sigma^- p$, $H \to \Sigma^0 n$ or $H \to \Lambda n$. The key reaction processes for each of the several experiments are listed in the review article of Sakai et. al. [34], while the details about the experimental setup can be found in the references therein. Most of the reported investigations provided no evidence for a stable H-dibaryon. Nevertheless, a few candidate events for a slightly bound H-dibaryon were detected, but it remained unclear if these observations could be explained by other than the expected processes.

Finally, the previous attempts to calculate the H-dibaryon mass on the lattice should be reviewed. The simulation parameters chosen by the different groups are summarized

Ref.	Gauge/Fermion Action	a[fm]	m_q[MeV]	Lattice Size	N_C	m_H[MeV]
[36]	standard	0.13	90-200	6^2x12x18	20	unbound
[37]	RG-imp./standard	0.11	105-590	16^3x48	15	1450-1710
[38]	standard			16^3x48	15	larger
[39]	standard	0.13	30-300	16^3x32	56	1950(60)
				24^3x32	40	2340(20)

Table 1.1: Summary of simulation parameters for the previous attempts to determine the mass of the H-dibaryon on the lattice.

in table 1.1. The two earlier investigations of Mackenzie and Thacker [36] and Iwasaki et. al. [37] gave contradicting results on the basis of limited statistics and relatively large quark masses. Moreover, deviations could be observed for different discretizations of the gauge action [38]. A more precise study of Negele et. al. [39] provided recently some insight in the volume dependence of the obtained results. Considerable finite size effects could not be ruled out by the authors for the smaller lattice size. The subsequent analysis on a larger lattice led to the conclusion that the H-dibaryon is unbound in the infinite volume limit.

In the present study the volume dependence of the H-dibaryon mass is investigated on several lattices sizes with a relatively large lattice spacing, which opens the possibility to examine a physical volume comparable and even larger than in the recent study of Negele et. al. [39]. Preliminary results on two of the lattice sizes were already reported in [40]. They have indicated an unbound H-dibaryon state with the mass of two Λ baryons. The detailed analysis of the strange hadron spectrum and in particular the H-dibaryon stability is provided in chapter 3.

Chapter 2

Lattice Gauge Theory

Having illustrated QCD in the Euclidean path integral formulation in the first chapter, we can now proceed to the representation as a regularized gauge theory on the lattice. The basic aspects of lattice QCD are introduced in section 2.1 including an overview of improved discretizations of the gauge and fermion actions. This section is completed by a paragraph about the continuum limit of the lattice formulation. For a general overview of lattice gauge theories the interested reader is referred to the textbooks of Rothe [41] and Montvay/Münster [42].

The following sections deal with the numerical details of the simulation. First of all this is the Monte Carlo integration method in section 2.2, which enables us to carry out the high dimensional QCD path integral. An efficient inversion of the fermion matrix is important in order to calculate the hadronic operators (see sec. 2.3). For some gauge-variant observables a gauge fixing of the gauge field configurations is necessary. This procedure is explained in section 2.4. The last section 2.5 of this chapter contains a short description of the error analysis for correlated data sets.

2.1 Lattice Regularization

Since the Euclidean path integral introduced in formula (1.4) is mathematically not well defined, a regularization scheme has to be implemented. Perturbative methods usually limit the magnitude of the momenta through the cut-off parameter Λ. Another possibility is to ensure the regularization in coordinate space by introducing a four dimensional space-time lattice of size $N_\sigma^3 \times N_\tau$ with a small, but finite lattice spacing a. The volume as well as the temperature on this hyper-cubic lattice are determined through its spatial and temporal extents in terms of the lattice cut-off a

$$V = (N_\sigma a)^3 \qquad \text{and} \qquad T = \frac{1}{N_\tau a}. \tag{2.1}$$

The lattice regularization requires the discretization of integrals and derivatives, which transform into finite sums and differences. The fermion fields, which are positioned on the lattice points, and observables like the string tension and particle masses can be rescaled to dimensionless quantities via the lattice spacing (see 2.1.3 for details). The gauge fields are identified with the link matrices $U_\mu \in SU(3)_C$, which are defined between neighboring lattice sites in the $\hat{\mu}$ direction by the parallel transporter

$$U_\mu(x = na) = \exp\,[\; ig \int_x^{x+\hat{\mu}a} dy^\mu A_\mu(y)]. \tag{2.2}$$

The discretized formulas for the gluon and fermion sector of the Euclidean action on the lattice are provided in the following two sections. Moreover, the construction of improved actions with reduced cut-off effects will be illustrated for both parts.

2.1.1 Gluonic Part of the Action

The lattice gauge action should be gauge-invariant like the respective continuum expression. The simplest object on the lattice which fulfills this requirement is the plaquette, i. e. the closed loop of four link variables around a square

$$U_{\mu\nu}(x) \equiv U_\mu(x) U_\nu(x+\hat{\mu}) U_\mu^\dagger(x+\hat{\nu}) U_\nu^\dagger(x) = \square_{\mu\nu}(x). \tag{2.3}$$

The gluonic part of the action can thus be written in terms of $U_{\mu\nu}(x)$

$$S_G(U) = \beta \sum_{x,\mu<\nu} \left(1 - \frac{1}{N_c} \text{Re Tr}\; U_{\mu\nu}(x)\right), \tag{2.4}$$

where the coupling $\beta = \frac{2N_c}{g^2}$ is related to the gauge coupling and the number of colors N_c.

In the limit of vanishing lattice spacing $a \to 0$, the gluon action (2.4) should reproduce the continuum representation. In order to show that this is indeed the case an expansion with respect to the lattice spacing a is necessary. After the application of the Baker-Hausdorff formula and a Taylor expansion around the center of the plaquette, the following equation is obtained

$$\begin{aligned} S_G &= \lim_{a\to 0} a^4 \sum_{x,\mu<\nu} \left[\text{Tr}\; F_{\mu\nu}F^{\mu\nu} + \mathcal{O}(a^2)\right] + \mathcal{O}(g^2a^2) \\ &= \frac{1}{2}\int_0^{1/T} d\tau \int_V d^3x \;\; \text{Tr}\; F_{\mu\nu}F^{\mu\nu} + \mathcal{O}(g^2). \end{aligned} \tag{2.5}$$

It can easily be observed that this simple parametrization of the gluonic action reproduces the continuum expression correctly up to $\mathcal{O}(g^2)$, but nevertheless yields cut-off effects of $\mathcal{O}(a^2)$ on the lattice. Following the Symanzik scheme [43], these deviations can be eliminated by additional gauge-invariant terms. For instance the (1×2)-improved lattice gauge action is correct to $\mathcal{O}(a^4)$

$$\begin{aligned} S_G^{(1,2)} = \beta \sum_{x,\mu<\nu} &\;\frac{5}{3}\left(1 - \frac{1}{N_c} \text{Re Tr}\; \square_{\mu\nu}(x)\right) \\ &- \frac{1}{6}\left(1 - \frac{1}{2N_c} \text{Re Tr}\left\{ \boxed{\quad\quad}_{\mu\nu}(x) + \boxed{\begin{matrix} \\ \\ \end{matrix}}_{\mu\nu}(x)\right\}\right). \end{aligned} \tag{2.6}$$

The coefficients of the 1 × 1 plaquette term and the additional 1 × 2 and 2 × 1 loop contribution are chosen such that the $\mathcal{O}(a^2)$ deviations eliminate each other. By adding further terms consisting of larger loops, the cut-off effects can be reduced up to any desirable order.

2.1.2 Fermionic Part of the Action

The naive discretization of the fermionic part of the Euclidean action (1.6) can be obtained simply by substituting the derivative with a finite difference of the rescaled fermion fields Ψ^i_α. Moreover one introduces the link matrices U^{ij}_μ instead of the gauge fields (2.2), which yields the following form of the fermion action

$$\begin{aligned} S_F^N &= \sum_{x,y,i,j,\alpha,\beta} \bar{\Psi}^i_\alpha(x) M^N_{\alpha\beta,ij}(x,y) \Psi^j_\beta(y) \qquad \text{with the fermion matrix} \\ M^N_{\alpha\beta,ij}(x,y) &= \sum_\mu \frac{1}{2} (\gamma_\mu)_{\alpha\beta} \left[U^{ij}_\mu(x)\, \delta_{x+\hat{\mu},y} - U^{\dagger ij}_\mu(x-\hat{\mu})\, \delta_{x-\hat{\mu},y} \right] + ma\, \delta_{xy}\delta_{\alpha\beta}\delta_{ij}, \end{aligned} \tag{2.7}$$

where i, j refer to the color degrees of freedom. By expanding this discretized expression in powers of the lattice spacing and the coupling constant, it can be verified that the naive fermion action reproduces its continuum counterpart up to $\mathcal{O}(a^2)$ corrections.

Since the fermion fields Ψ^i_α obey the anti-commutation relation, they are realized as Grassmann variables living on the lattice sites. The calculation of expectation values of fermionic observables involves the evaluation of the path integral over these Grassmann fields, which can be easily performed by means of the Grassmann integration rules

$$\begin{aligned} \langle \Psi_{y_1}\bar{\Psi}_{x_1} \dots \Psi_{y_n}\bar{\Psi}_{x_n} \rangle &= \frac{1}{Z} \int DU D\Psi D\bar{\Psi}\, (\Psi_{y_1}\bar{\Psi}_{x_1} \dots \Psi_{y_n}\bar{\Psi}_{x_n})\, e^{-\bar{\Psi}M\Psi - S_G} \\ &= \frac{1}{Z} \int DU\, \Big(\sum_{z_1 \dots z_n} \epsilon^{z_1 \dots z_n}_{y_1 \dots y_n}\, M^{-1}_{z_1 x_1} \dots M^{-1}_{z_n x_n} \Big)\, \det M\, e^{-S_G}, \end{aligned} \tag{2.8}$$

where ϵ denotes the total anti-symmetric tensor. The integral of the n-particle observable $\Psi_{y_1}\bar{\Psi}_{x_1} \dots \Psi_{y_n}\bar{\Psi}_{x_n}$ leads to a product of the inverse fermion matrix components, while the integration of the fermionic part of the action $S_F = \bar{\Psi}M\Psi$ results in the determinant of the fermion matrix M.

Setting this determinant equal to one is a simplification commonly used for the computation of expectation values. The so-called **Quenched Approximation** neglects the contributions of internal quark loops and thus considers static quarks and dynamical gluon background fields. This procedure appears to be very restrictive at first sight, but it could be demonstrated that most of the properties of QCD can be investigated qualitatively in this approximation. For instance, the obtained hadron masses agree with the experimental spectrum in an average 10% range [44]. Since the path integral (2.8) can now be evaluated in updating only the dynamical gauge fields, an enormous amount of computer time can be saved by the application of fast local algorithms (see section 2.2 for details).

A severe problem of the naive discretization (2.7) becomes obvious in the momentum space representation of the free fermion action for one quark flavor

$$S_F^N = \int_{-\frac{\pi}{a}}^{+\frac{\pi}{a}} \frac{d^4p}{(2\pi)^4}\, \bar{\Psi}(p) \left(\sum_\mu i\gamma_\mu \frac{1}{a} \sin(p_\mu a) + m \right) \Psi(p). \tag{2.9}$$

The free quark propagator can thus be obtained by employing the Grassmann integration rules (2.8) as the inverse of the above fermion matrix

$$\begin{aligned} \langle \bar{\Psi}(p) \Psi(q) \rangle &= \left(\sum_\mu i\gamma_\mu \frac{1}{a} \sin(p_\mu a) + m \right)^{-1}_{\alpha\beta} \delta(p-q) \\ &= \frac{\left(-i \sum_\mu \gamma_\mu \tilde{p}_\mu + m \right)_{\alpha\beta}}{\sum_\mu \tilde{p}_\mu^2 + m^2}\, \delta(p-q) \qquad \text{with} \qquad \tilde{p}_\mu = \frac{1}{a} \sin(p_\mu a). \end{aligned} \tag{2.10}$$

It can easily be observed that this propagator has poles not only at zero momentum but also at all other corners of the Brillouin zone. This phenomenon is referred to as fermion doubler problem, since a doubling of the particle content occurs in every dimension d. In the continuum limit this yields $2^d - 1 = 15$ unwanted particles in addition to the physically relevant one. Hence the naive fermion discretization would produce $2^d \cdot N_f$ particles for N_f quark flavors, which do not vanish in the limit $a \to 0$.

In a No-Go theorem [45] Nielsen and Ninomiya have shown that a lattice regularization of QCD with exact chiral symmetry but without fermion doublers cannot be achieved. The next few paragraphs deal with various methods which were developed to circumvent or at least reduce the fermion doubler problem through the sacrifice of the exact chiral symmetry.

Wilson Fermions

The aim of the Wilson fermion formulation is to increase the masses of the unwanted doublers in a way which ensures that they diverge in the continuum limit. This can be reached by adding a term proportional to the second derivative of the quark field to the naive fermion action

$$S_F^W = S_F^N - \frac{r}{2} \sum_{x,\alpha,i} \bar{\Psi}_\alpha^i(x) \Box \Psi_\alpha^i(x) = \sum_{xy,\alpha\beta,ij} \bar{\Psi}_\alpha^i(x) M^W_{\alpha\beta,ij}(x,y) \Psi_\beta^j(y), \tag{2.11}$$

which breaks explicitly the chiral symmetry. The parameter r controls the strength of this auxiliary term. In the following $r = 1$ will be chosen for convenience, since this yields the projection operators $(\mathbb{1} \pm \gamma_\mu)$ in the Wilson fermion matrix

$$\begin{aligned} M^W_{\alpha\beta,ij}(x,y) &= (ma+4)\, \delta_{xy} \delta_{\alpha\beta} \delta_{ij} - \frac{1}{2} \sum_\mu [\, (\mathbb{1} - \gamma_\mu)_{\alpha\beta}\, U_\mu^{ij}(x)\, \delta_{x+\hat{\mu},y} \\ &\qquad + (\mathbb{1} + \gamma_\mu)_{\alpha\beta}\, U_\mu^{\dagger ij}(x-\hat{\mu})\, \delta_{x-\hat{\mu},y}], \end{aligned} \tag{2.12}$$

which results in advantages in the explicit numerical implementation.

The free quark propagator in the momentum space can be calculated similarly to (2.10) as inverse of the Wilson fermion matrix, which leads to the momentum dependent mass defined below

$$\begin{aligned}\langle\bar{\Psi}(p)\Psi(q)\rangle &= \frac{\left(-i\sum_\mu \gamma_\mu \tilde{p}_\mu + m(p)\right)_{\alpha\beta}}{\sum_\mu \tilde{p}_\mu^2 + m(p)^2}\;\delta(p-q) \\ m(p) &\equiv m + \frac{2}{a}\sum_\mu \sin^2(p_\mu a/2). \end{aligned} \tag{2.13}$$

This mass term ensures the divergence of the redundant particle masses in the limit $a \to 0$ for non-zero momenta. For instance a fermion with $p = (0,0,0,\pi/a)$ would acquire a mass $m(p) = m + \frac{2}{a}$, while the mass of the physical particle at $p = (0,0,0,0)$ remains the same.

In the Wilson formulation the bare quark mass experiences an additive renormalization through the introduction of the chiral symmetry breaking term. Therefore the quark mass is controlled by the hopping parameter $\kappa = \frac{1}{2(ma+4)}$. This causes a severe tuning problem, since the quark mass now vanishes at varying κ-values for different couplings. In the case of the free theory ($g \to 0$) this occurs at $\kappa_c = 1/8$, while the critical value is reached at $\kappa_c = 1/4$ in the strong coupling limit.

In the intermediate coupling range κ_c has to be determined with the aid of other observables in the numerical simulation. In leading order perturbation theory the quark mass on the lattice

$$\hat{m}_q = m_q a = \frac{1}{2}\left(\frac{1}{\kappa} - \frac{1}{\kappa_c}\right) \tag{2.14}$$

can be related to the square of the pion mass $m_q \sim m_\pi^2$ by the PCAC hypothesis in chiral perturbation theory. The value of κ at which the pion becomes the massless Goldstone boson thus defines the point of zero bare quark mass. An alternative definition can be established on the basis of the axial Ward identity. The quark mass is then obtained from the ratio of the axial vector current combined with the pseudo-scalar density and the pion correlator $\mathcal{M}_{PS}(x,\tau)$ (see sec. 3.2) through

$$\frac{2m_q}{Z_A} = \frac{\sum_x \langle \partial_\mu A_\mu(x,\tau)\mathcal{M}_{PS}^\dagger(0)\rangle}{\sum_x \langle \mathcal{M}_{PS}(x,\tau)\mathcal{M}_{PS}^\dagger(0)\rangle}, \tag{2.15}$$

where Z_A is a multiplicative renormalization factor for the axial current. Having obtained the bare quark masses for different κ-values, they have to be extrapolated to zero again. Note that these two estimates of κ_c can differ by $\mathcal{O}(a)$ corrections.

Finally the remark should be added that the auxiliary Wilson term changes the discretization errors from $\mathcal{O}(a^2)$ in the naive formulation to $\mathcal{O}(a)$ corrections for free Wilson fermions. The previous situation can be restored by introducing the Clover fermion formulation.

Clover Fermions

A further supplementary term proportional to the field strength tensor was added to the Wilson fermion action by Sheikholeslami and Wohlert [46] in order to ensure that the Clover action shows only $\mathcal{O}(a^2)$ discretization errors. Rescaling the fermion fields with respect to the hopping parameter $\Psi'(x) = \frac{1}{\sqrt{2\kappa}}\Psi(x)$ yields

$$\begin{aligned} S_F^C &= S_F^W - ig\, c_{SW}\, \frac{\kappa}{2} \sum_{x,\alpha,i} \bar{\Psi}'_{\alpha,i}(x) F_{\mu\nu}(x) \sigma_{\mu\nu} \Psi'_{\alpha,i}(x) \\ &= \frac{1}{2\kappa} \sum_{xy,\alpha\beta,ij} \bar{\Psi}'_{\alpha,i}(x) M^{ij}_{\alpha\beta}(x,y) \Psi'_{\beta,j}(y). \end{aligned} \tag{2.16}$$

The Clover fermion matrix is defined through the Clover term A and the Δ-operator

$$M^{ij}_{\alpha\beta}(x,y) = A^{ij}_{\alpha\beta}(x)\, \delta_{xy} - \kappa\, \Delta^{ij}_{\alpha\beta}(x,y) \tag{2.17}$$

$$A^{ij}_{\alpha\beta}(x) = \mathbb{1} - ig\, c_{SW} \frac{\kappa}{2}\, F_{\mu\nu}(x)\, \sigma_{\mu\nu}$$

$$\Delta^{ij}_{\alpha\beta}(x,y) = \sum_{\mu} [\, (\mathbb{1} - \gamma_\mu)_{\alpha\beta}\, U^{ij}_\mu(x)\, \delta_{x+\hat{\mu},y} + (\mathbb{1} + \gamma_\mu)_{\alpha\beta}\, U^{\dagger ij}_\mu(y)\, \delta_{x-\hat{\mu},y}\,], \tag{2.18}$$

where the field strength tensor on the lattice is given by $F_{\mu\nu}(x) = \frac{1}{8ig} \sum_j [U^j_{\mu\nu}(x) - U^{\dagger,j}_{\mu\nu}(x)]$. The sum is defined over the four plaquettes in the $\mu\nu$-plane around the site x, the so-called Clover term. The numerical processing of the fermion matrix (2.17) is described in detail in section 2.3. Altogether the $\mathcal{O}(a)$ improved Clover fermion action can be visualized in the following way

$$S_F^C = \frac{1}{2\kappa} \sum_{x,y} \bar{\Psi}'(x) \left\{ \left[\mathbb{1} - c_{SW} \frac{\kappa}{2} \sum_{\mu,\nu} \mathrm{Im}\right.\right.$$

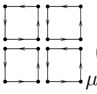

$$\left.\left.{}_{\mu\nu}(x)\, \sigma_{\mu\nu} \right] \delta_{x,y} - \kappa\, \Delta^{ij}_{\alpha\beta}(x,y) \right\} \Psi'(y). \tag{2.19}$$

The clover coefficient c_{SW} in the action has to be chosen appropriately. For the tree-level improved gauge action it is simply set to one [46], but this parameter can also be optimized in a non-perturbative way. Simulations with different clover coefficients and couplings g should obey the PCAC relation up to order a^2 corrections. This leads to the following expression for c_{SW} in the quenched approximation obtained with the Wilson plaquette gauge action [47]

$$c_{SW} = \frac{1 - 0.656\, g^2 - 0.152\, g^4 - 0.054\, g^6}{1 - 0.922\, g^2} \qquad \text{for} \qquad 0 \leq g \leq 1. \tag{2.20}$$

An analogous result for simulations with dynamical fermions was reported in [48]. The calculations for this thesis were performed with the (1×2)-improved gauge action and the Clover fermion action with a tree-level clover coefficient at zero temperature, while the simulations at finite temperature were carried out with the plaquette gauge action and the non-perturbatively improved Clover fermion action.

Staggered Fermions

Another commonly used fermion discretization is the Kogut-Susskind [49] or staggered fermion formulation, where the spinor degrees of freedom are distributed over hypercubes of the lattice. This reduces the fermion doubler problem, but four degenerate quark flavors are still included in the continuum limit. The advantage of staggered fermions is manifested in the preserved $U(1) \times U(1)$ symmetry as remnant of the global chiral symmetry. Therefore the chiral condensate serves as an order parameter of the phase transition at finite temperature. This is the reason why the staggered formulation is mostly used for the calculation of thermodynamic observables in the vicinity of the critical temperature.

Chiral Fermions

In recent years fermion discretizations with approximate chiral symmetry became available. The starting point is the Ginsparg-Wilson relation $\gamma_5 D + D\gamma_5 = aD\gamma_5 D$ [50] for the Dirac operator D, which implies that the chiral symmetry as well as the axial $U_A(1)$ anomaly are preserved for vanishing quark mass m_q on a lattice with finite lattice spacing [51]. This general idea led to two different formulations, known as domain wall [52] and overlap discretization [53, 54] of the fermion matrix. The domain wall approach is based on the introduction of a fifth dimension in addition to the four dimensional space-time lattice. Then the chiral symmetry breaking is suppressed exponentially with the extent L_s of this extra dimension. Exact chiral symmetry can thus be obtained theoretically with an infinite extent L_s. The overlap formulation however works in an infinite flavor space, which is equivalent to the domain wall approach in the limit $N_s \to \infty$. Although these realizations of chiral fermions in lattice simulations seem very promising, the actual calculations suffer nevertheless from the increase in the required computer time, which rises linearly with the extent of the fifth dimension.

2.1.3 Continuum Limit

As already addressed before the observables on the lattice $\mathcal{O}\left(g(a), a\right)$ can be rescaled to dimensionless quantities $\hat{\mathcal{O}}$ through the lattice spacing in the appropriate dimension $dim(\mathcal{O})$. They are related to their corresponding physical value $\mathcal{O}_{phys}$ in the continuum limit via

$$\mathcal{O}\left(g(a), a\right) = a^{-dim(\mathcal{O})} \hat{\mathcal{O}}\left(g(a), a\right) \underset{a\to 0}{\longrightarrow} \mathcal{O}_{phys}. \tag{2.21}$$

This relation is only valid if the coupling on the lattice $g(a \to 0)$ approaches the critical coupling g^*, which is defined at the point of diverging correlation length $\xi \sim \frac{1}{m}$ in analogy to statistical models. In QCD the limit $\xi \to \infty$ is reached with increasing β, or equivalently $g \to 0$ due to the asymptotic freedom. In this weak coupling regime perturbative methods provide the dependence between the lattice spacing and the coupling

$$a(\frac{\partial g}{\partial a}) = b_0 g^3 + b_1 g^5 + \mathcal{O}(g^7) \tag{2.22}$$

with the universal coefficients

$$b_0 = \frac{1}{16\pi^2}\left(\frac{11}{3}N_c - \frac{2}{3}N_f\right) \qquad \text{and} \qquad b_1 = \frac{1}{(16\pi^2)^2}\left(\frac{34}{3}N_c^2 - N_f[\frac{10}{3}N_c + \frac{N_c^2-1}{N_c}]\right)$$

The integration of the function (2.22) then yields directly the lattice spacing in terms of the coupling

$$a(g) = \frac{1}{\Lambda_L}(b_0 g^2)^{-\frac{b_1}{2b_0^2}} \exp(-\frac{1}{2b_0 g^2}). \tag{2.23}$$

Here the integration constant Λ_L defines the invariant scale for the lattice theory, which is related by a multiplicative factor to the scale parameter in other regularization schemes, like $\Lambda_{\overline{MS}}$ or Λ_{MOM} [55].

Given the dimensionless results from lattice simulations, they have to be properly rescaled in terms of the lattice spacing. The physical scale can be inferred from the determination of the string tension or hadron masses on the lattice, which are related to their well-known experimental values

$$m_\rho = \hat{m}_\rho\, a^{-1} = 770\ MeV \qquad \text{or} \qquad \sqrt{\sigma} = \sqrt{\hat{\sigma}}\, a^{-1} = 420\ MeV. \tag{2.24}$$

Alternatively the ratio of two physical quantities can be used to set the scale. This approach is employed in section 3.3 in order to obtain the physical quark mass values κ_u and κ_s in the Wilson quark formulation.

2.2 Monte Carlo Integration

After the basic concepts of lattice QCD the focus is now on the numerical implementation of the formerly described methods. The Euclidean path integral formalism was already introduced in section 1.1. After the analytic integration over the fermion fields (equation 2.8), the expectation value of an operator $\mathcal{O}$ in the quenched approximation is given by

$$\langle \mathcal{O} \rangle = \frac{1}{Z}\int \prod_{x,\mu} dU_\mu(x)\mathcal{O}[U]e^{-S_G[U]}. \tag{2.25}$$

Nevertheless this leaves us with a high dimensional integral of order $\mathcal{O}(10^6)$, which can only be evaluated approximately by **Monte Carlo integration**.

In generating gauge field configurations with the Boltzmann distribution in the thermal equilibrium, one can ensure to consider the most significant contributions to the path integral (**importance sampling**). A new configuration U' is produced from its predecessor U in a so-called **Markov chain** with a certain transition probability. The following approximate expression for the expectation value is thus valid for a large number of configurations N_C

$$\langle \mathcal{O} \rangle \simeq \frac{1}{N_C}\sum_{i=1}^{N_C} \mathcal{O}[U_i]. \tag{2.26}$$

The **detailed balance** condition is required to obtain the equilibrium probability distribution:

$$e^{-S[U]}P(U \to U') = e^{-S[U']}P(U' \to U). \tag{2.27}$$

Furthermore **ergodicity** is needed, which means that any possible configuration U' should be obtainable with finite probability from every configuration U.

The first and simplest algorithm which fulfills these requirements was the one developed by Metropolis et. al. [56]. For the simulations reported in this thesis the pseudo-heatbath update method [57, 58] was utilized, improved by 4-5 overrelaxation steps [59, 60] after each heatbath step. Both are local update routines which produce a new configuration by a sweep over all lattice sites. The pseudo-heatbath algorithm consists of the successive application of the heatbath algorithm on all $SU(2)$ subsets, where the local equilibration resembles the contact with an infinite heatbath.
The overrelaxation update is an efficient method to reduce the correlations between the generated configurations. Since it is desirable to analyze nearly uncorrelated gauge field configurations, the observables are measured only on configurations separated by several hundred sweeps.

2.3 Inversion of the Fermion Matrix

The most fundamental fermionic observable in lattice QCD is the expectation value of the quark propagator $G(x, y)$, which can be calculated using the analytic integration over the fermion fields (see formula (2.8)):

$$\begin{aligned} G(x,y) &= \langle \Psi(x)\bar{\Psi}(y)\rangle \\ &= \frac{1}{Z}\int DUD\Psi D\bar{\Psi}\ \ \Psi(x)\bar{\Psi}(y)\ \ e^{-\bar{\Psi}M\Psi - S_G} \\ &= \frac{1}{Z}\int DU\ M^{-1}(x,y)\ \det M\ e^{-S_G}. \end{aligned} \tag{2.28}$$

The important quantity which is thus needed, is the inverse of the fermion matrix $M^{-1}(x, y)$ evaluated on every gauge field configuration in the quenched approximation ($\det M = 1$). This requires the solution of the inhomogeneous equation

$$M(x,y)\psi(y) = \phi(x) \tag{2.29}$$

with point-like sources $\phi(x)$ for every color-spin combination of the quark fields.

Since the fermion matrix is a very large* but particularly sparse matrix, the above equation (2.29) can only be solved approximately with an iterative method. The rapidness of convergence is determined by the distribution of the eigenvalues of this matrix. The number of iterations needed for the inversion is proportional to the ratio of the largest to

---

* $N \times N$ fermion matrix with $N =$ (lattice size) × (color) × (spinor) degrees of freedom $\approx \mathcal{O}(10^5 - 10^6)$

the smallest eigenvalue, which is divergent for vanishing quark mass $m_q \to 0$, respectively $\kappa \to \kappa_c$ below the critical temperature. An optimized inversion of the fermion matrix can be reached in a twofold way. On the one hand a fast and efficient algorithm should be used to solve the equation (2.29) within a minimum of iteration steps, on the other hand a preconditioning procedure can further reduce the number of steps required for convergence.

Most of the common algorithms developed for the inversion of the fermion matrix stem from the conjugate residual method [61, 62]. For the simulations described in this thesis the BiCGstab algorithm [63] was employed. It was developed and improved from the Conjugate Gradient (CG) method [64], which guarantees convergence in N iteration steps for a $N \times N$ fermion matrix. It could be shown [65] that the BiCGstab converges much faster than other algorithms, in particular in the region of small quark masses.

The even-odd preconditioning technique [66] uses the property of the Clover fermion matrix (2.17), that it only connects lattice sites of opposite parity. The equation $M\psi = \phi$ (2.29) decouples into separate parts for the (e)ven and the (o)dd sites

$$\begin{aligned} \tilde{M}_{ee}\,\psi_e &= \phi_e + \kappa\,\Delta_{eo}\,A_{oo}^{-1}\,\phi_o = \tilde{\phi}_e && (2.30)\\ \psi_o &= A_{oo}^{-1}\,(\phi_o + \kappa\,\Delta_{oe}\psi_e) && (2.31) \end{aligned}$$

with a different source vector $\tilde{\phi}_e$ and a modified fermion matrix $\tilde{M}_{ee} = A_{ee} - \kappa^2\,\Delta_{eo}\,A_{oo}^{-1}\,\Delta_{oe}$ on the even sites of the lattice. After the BiCGstab inversion on the even sites (2.30), the solution for the odd sites can simply be obtained by a back substitution in (2.31). The major advantage of this preconditioning procedure is the new matrix $\tilde{M}_{ee}$, which is now second order in κ. Approaching the chiral limit ($\kappa \to \kappa_c$), the number of required iteration steps is considerably lower, since the κ-dependent smallest eigenvalue of $\tilde{M}_{ee}$ is about two times larger than the one of the original fermion matrix M.

2.4 Gauge Fixing

Some of the interesting operators in lattice QCD, like the quark or diquark propagators, are gauge-variant quantities. They form color (anti-)triplet or sextet states in contrast to the color singlet mesons and baryons. Therefore it is necessary to perform gauge fixing in order to calculate quark and diquark correlation functions.

The invariance of the gluonic action under local gauge transformations $U_\mu^G = G(x)U_\mu(x)\, G^\dagger(x+\hat{\mu})$ with a matrix $G(x) \in SU(3)$ is the basis for the gauge fixing procedure in lattice QCD. After the generation of the gauge field configurations with the Monte Carlo method they can be transformed separately into the desired gauge [67]. A whole bunch of gauges is defined through the λ-gauges [68]. The λ-gauge condition in the continuum requires

$$\sum_{\mu=1}^{4} \lambda_\mu \partial_\mu A_\mu(x) = \lambda \partial_4 A_4(x) + \sum_{\mu=1}^{3} \partial_\mu A_\mu(x) = 0 \qquad (2.32)$$

with the definition $\lambda_\mu \equiv \lambda$ for $\mu = 4$ and $\lambda_\mu \equiv 1$ for $\mu = 1 \ldots 3$. The gauge independence of the observables can thus be studied by varying the λ parameter. $\lambda = 1$ corresponds to the **Landau gauge**, whereas $\lambda \to 0$ yields the **Coulomb gauge**.

Evaluating the gauge condition on the lattice corresponds to minimizing the following functional [69]

$$\mathcal{F}_U^\lambda[G] \equiv -\ \mathrm{Tr} \sum_{x,\mu} \lambda_\mu U_\mu^G(x) = -\ \mathrm{Tr} \sum_{x,\mu} \lambda_\mu G(x) U_\mu(x) G^\dagger(x+\hat{\mu}). \tag{2.33}$$

After choosing the gauge transformation matrix $G(x)$ appropriately, the functional $\mathcal{F}$ can be driven to a minimum in an iterative process. Two common algorithms developed for this purpose are the Cornell [70] and the Los Alamos method [71, 72]. Both algorithms suffer from a considerable slowing down effect: The more precisely the gauge condition is fulfilled the nearer the transformation $G(x)$ resembles the unitary transformation, which makes the algorithm less and less efficient.

Various methods have been proposed to speed up the convergence, for example the overrelaxation procedure [73] or the time-consuming Fourier acceleration [70]. In contrast to all other algorithms mentioned above, the Fourier acceleration is a non-local procedure which involves wide range communications on parallel machines. Therefore the numerically optimized fast Fourier transformation (FFT) is commonly used for the implementation.

For the previous simulations at zero temperature, which were already reported in [74, 75], the Landau gauge was used. It was implemented with the Cornell method and accelerated by a FFT procedure. For the new configurations above the critical temperature the Coulomb gauge condition was applied, realized through the Los Alamos algorithm combined with the overrelaxation method. The Coulomb gauge was chosen with regard to the maximum entropy method (MEM), which is described in detail in chapter 4. The aim was to yield a positive definite spectral function for the quark propagator, respectively a plateau for the effective quark mass which is reached from above (see section 3.3). This is definitely not the case for the Landau gauge, where no transfer matrix can be constructed.

2.5 Error Analysis

The gauge field configurations generated by Monte Carlo integration (sec. 2.2) are not completely uncorrelated. The **Jackknife procedure** takes the autocorrelation between the observables on different configurations into account and provides an improved estimate of the mean values and errors.

For this purpose the complete data set is divided into N subsamples of equal length. Leaving out one subsample respectively, the mean value on each reduced sample D_k can be calculated. The improved mean value and the corresponding error are then obtained by the statistical average

$$\begin{aligned} \mathcal{O} &\simeq J = \frac{1}{N}\sum_{k=1}^{N} J_k \qquad \text{with} \qquad J_k = ND - (N-1)D_k \\ \delta\mathcal{O} &\simeq \sigma_J = \sqrt{\frac{\sum_{k=1}^{N}(J_k - J)^2}{N(N-1)}}\,, \end{aligned} \tag{2.34}$$

where D denotes the mean value on the whole sample.

Furthermore strong correlations between different time slices τ_i are observed for hadronic correlation functions. The standard χ^2-fit for a function $F(\tau_i, \vec{p})$ which depends on the parameters $\vec{p}$,

$$\chi^2 = \sum_i \left[\frac{F(\tau_i,\vec{p}) - D(\tau_i)}{\sigma(\tau_i)}\right]^2, \tag{2.35}$$

includes only the standard deviation $\sigma(\tau_i)$ for each time slice independently and neglects the correlations among them completely. Therefore it is essential to take the inverse of the covariance matrix C_{ij} into consideration, which results in a modified fit ansatz

$$\chi^2 = \sum_{i,j} [F(\tau_i,\vec{p}) - D(\tau_i)]\; C^{-1}_{ij}\; [F(\tau_j,\vec{p}) - D(\tau_j)], \tag{2.36}$$

where the symmetric covariance matrix is given by

$$C_{ij} = \frac{1}{N_C(N_C-1)} \sum_{m=1}^{N_C} [D^m(\tau_i) - D(\tau_i)]\; [D^m(\tau_j) - D(\tau_j)]. \tag{2.37}$$

This approach is contained in the Likelihood function of the Maximum Entropy Method, which will be described in chapter 4. Setting all off-diagonal components of the covariance matrix to zero then corresponds to the uncorrelated χ^2-fit in (2.35).

In the case of a limited number of configurations one is sometimes confronted with very small or nearly zero eigenvalues of the covariance matrix, which results in unreasonable large eigenvalues of the inverse. One solution is to calculate the inverse with a singular value decomposition (SVD), which corresponds to omitting the smallest eigenvalues. A less restrictive procedure, the **eigenvalue smoothing**, was proposed by Michael and McKerrel [76]. Thereby the smaller eigenvalues are replaced by the average of them, whereas the larger ones remain the same. The eigenvectors of the covariance matrix and thus of its inverse are kept unchanged.

Considering N_τ eigenvalues λ_i of the covariance matrix with $\lambda_i \geq \lambda_{i+1}$, the smoothing method can be implemented as follows

$$\lambda'_i = \max\,(\lambda_i, \lambda_{min}) \qquad \text{with} \qquad \lambda_{min} = \frac{1}{N_\tau - N_R} \sum_{i=N_R+1}^{N_\tau} \lambda_i, \tag{2.38}$$

where N_R denotes the number of retained large eigenvalues. This procedure often provides a more stable model of the correlation matrix from the sample data (see section 4.6).

Chapter 3

Strange Hadron Spectrum

After a short introduction to the symmetries of the particle spectrum and the underlying quark interactions in section 3.1 the appropriate operators and correlation functions for the simulations are summarized in 3.2. The subsequent paragraph 3.3 explains how the particle masses are extracted from the correlation function, while section 3.4 describes the extrapolation to physical quark masses. The following section 3.5 illustrates the improvement through the application of the fuzzing technique. The last part 3.6 of this chapter describes the present lattice simulation and provides the results obtained for the strange hadron masses and the H-dibaryon stability.

3.1 Hadron Multiplets

Considering the three lightest quark flavors to be mass degenerate $m_u \simeq m_d \simeq m_s$, the $SU(3)$ isospin symmetry accounts for the multiplet structure of the observed light hadron spectrum. The three (anti-)quarks u, d and s form a flavor (anti-)triplet in the framework of the $SU(3)$ symmetry group, which is generated by the eight Gell-Mann matrices λ^a, $a = 1 \ldots 8$.

In order to construct a meson $(q\bar{q})$ the product of a $SU(3)$ triplet and an anti-triplet has to be evaluated. It separates into irreducible singlet and octet representation

$$\mathbf{3} \times \bar{\mathbf{3}} \;=\; \mathbf{1} + \mathbf{8}. \tag{3.1}$$

In figure 3.1 the octets of the pseudo-scalar and vector mesons are visualized, where I_3 denotes the third component of the isospin and S is the strangeness quantum number. The pseudo-scalar singlet is approximately the η' meson, whereas a mixing of singlet and octet states contributes to the vector mesons ω and ϕ.

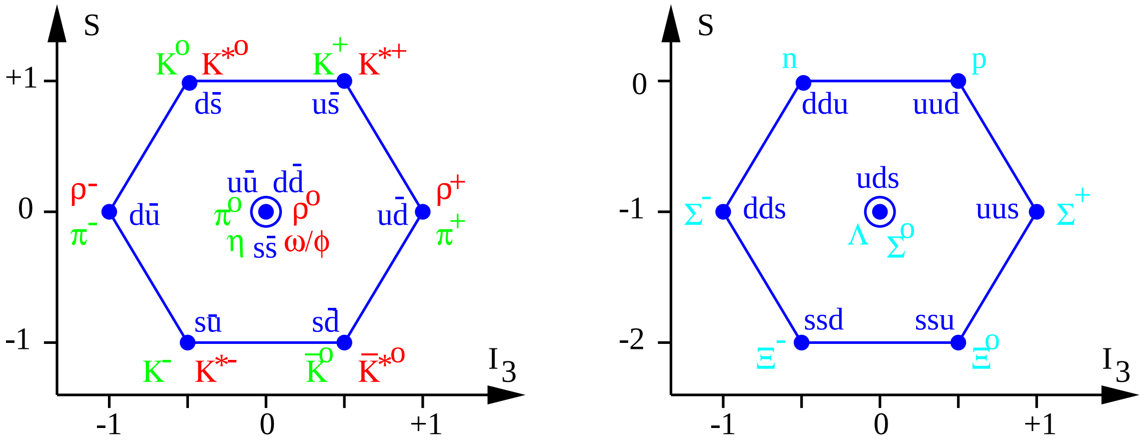

Figure 3.1: Multiplet structure for the pseudo-scalar and vector mesons (left) as well as for the spin $\frac{1}{2}$ baryons (right).

Alternatively two quarks can be assembled in a diquark state. The nine possible (qq) combinations group themselves into an anti-triplet and a sextet according to

$$\mathbf{3} \times \mathbf{3} \;=\; \bar{\mathbf{3}} + \mathbf{6}. \tag{3.2}$$

This leads to the anti-symmetric anti-triplet states and the symmetric sextet states shown in figure 3.2. The splitting in irreducible representations works similarly in the $SU(3)$ color group. Combining two color triplets results likewise in a color anti-triplet and a sextet. Note that in contrast to the ordinary mesons and baryons no color singlet is obtained for such a two quark state. Therefore the diquarks are color carrying objects, which may only occur in the color superconducting phase of QCD at high densities (see fig. 1.1).

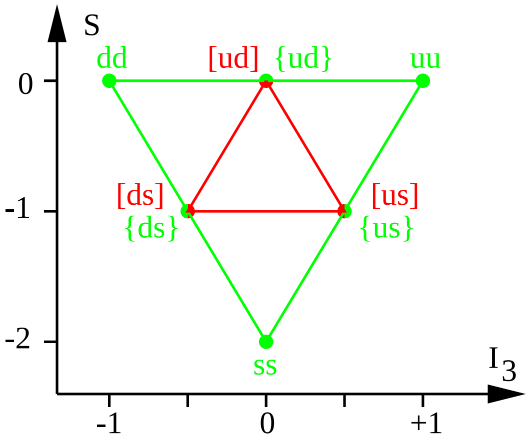

Figure 3.2: Multiplet structure for the flavor anti-triplet and sextet diquarks.

In order to construct a total anti-symmetric wave function for the diquark state, the color and flavor representations have to be combined appropriately with a total spin zero or one of the two quarks. The possible diquark states are summarized in table 3.1. The last two columns give the relative strength of the q-q interaction due to a flavor-spin or a color-spin coupling, which can be calculated via two-body matrix elements with the potential [77, 78]

$$V \sim (\lambda_i^a \lambda_j^a)(s_i s_j). \tag{3.3}$$

The λ_i^a denote the generators of the $SU(3)$ flavor or color symmetry group, respectively. The q-q interaction is attractive for the flavor anti-triplet diquarks considering the color-spin coupling, which arises in perturbative QCD from one-gluon-exchange (OGE) [22]. In contrast to that the instanton liquid model predicts an attractive interaction in the color

(F,S,C)	diquark state	FS coupling	CS coupling
$(\bar{3},0,\bar{3})$	$\epsilon_{abc}(C\gamma_5)_{\alpha\beta}\ u^{\dagger}_{a,\alpha}d^{\dagger}_{b,\beta}$	-2	-2
$(6,1,\bar{3})$	$\epsilon_{abc}\ u^{\dagger}_{a,\alpha}u^{\dagger}_{b,\alpha}$	-1/3	2/3
$(\bar{3},1,6)$	$u^{\dagger}_{c,\alpha}d^{\dagger}_{c,\alpha}$	2/3	-1/3
$(6,0,6)$	$(C\gamma_5)_{\alpha\beta}\ u^{\dagger}_{c,\alpha}u^{\dagger}_{c,\beta}$	1	1

Table 3.1: Diquark states in the color anti-triplet and sextet representation.

anti-triplet channel [23, 24]. Such a spin and flavor dependent coupling between the constituent quarks is needed to describe the fine structure of the experimentally observed hadron spectrum correctly [78].

Our previous analysis of diquark correlation functions in lattice QCD [74, 75] provided evidence that the diquark splitting at zero temperature and density follows the order given by the flavor-spin interaction. For the lightest $\bar{3}0\bar{3}$ state a mass compatible with twice the constituent quark mass was found. A more sophisticated investigation of the diquark correlators will be given in section 4.6 by applying the Maximum Entropy Method. Since the one-gluon-exchange (CS coupling) gains in importance at increasing baryon density, a reversal of the order for the spin 1 states and a slightly bound $\bar{3}0\bar{3}$ diquark state seems possible, which would support the existence of a color superconducting diquark phase at high density (see section 1.3).

Adding a further quark (q) to the diquark state (qq) leads to the formation of the baryons (qqq), which belong to the following multiplets [79]

$$(\mathbf{3}\times\mathbf{3})\times\mathbf{3} \;=\; (\bar{\mathbf{3}}+\mathbf{6})\times\mathbf{3} \;=\; \mathbf{1_A}+\mathbf{8_M}+\mathbf{8_M}+\mathbf{10_S}. \tag{3.4}$$

The spin $\frac{3}{2}$ baryons build the symmetric decuplet, while the spin $\frac{1}{2}$ baryon octet (see figure 3.1) is described by a mixed representation. The anti-symmetric singlet state can be identified with the heavier $\Lambda(1405)$ baryon. In the lattice simulation reported in this thesis, the correlation functions for the nucleon, sigma and lambda baryons as well as for the pion, rho, K and K^* mesons were calculated. The particles in the same isospin multiplet are mass degenerate, since the states carry no charge quantum number on the lattice.

As already discussed in section 1.4 the main purpose of the analysis of the strange hadron spectrum is to examine the stability of the six quark state called H-dibaryon. This particle is built of two quarks of each light flavor u, d and s and forms the anti-symmetric $SU(3)_F$ flavor singlet state. In order to obtain a total anti-symmetric wave function, color and spin have to be symmetrized in the combined $SU(6)_{CS}$ group. The H-dibaryon belongs to the **490** representation of this group, which contains the anti-symmetric color and spin singlets. This is the most attractive channel for the q-q interaction in formula (3.3) arising from one-gluon-exchange [33, 80].

3.2 Hadron Operators and Correlation Functions

In lattice calculations the particle masses can be obtained from the exponential decay of the two-point correlation functions. This paragraph provides the appropriate operators and corresponding correlators for mesons, diquarks, baryons and finally the H-dibaryon.

A general meson operator is constructed from the quark and anti-quark fields with the desired quantum numbers combined with one of the matrices $\Gamma = \mathbb{1}, \gamma_5, \gamma_\mu, \gamma_5\gamma_\mu$ or $\sigma_{\mu\nu}$

$$\mathcal{M}(\vec{x},\tau) = \bar{\Psi}^{c,f_1}_{\alpha}(\vec{x},\tau)\ (\Gamma)_{\alpha\beta}\ \Psi^{c,f_2}_{\beta}(\vec{x},\tau). \tag{3.5}$$

Given the operator, the connected flavor non-singlet part of the two-point correlation function $G(\vec{x},\tau) = \langle \mathcal{M}(\vec{x},\tau)\mathcal{M}^\dagger(0)\rangle$ can be evaluated according to (2.8) in analogy to the quark propagator in formula (2.28). Moreover, the anti-commutation relations of the fermion fields and the γ-matrices have to be taken into account. The specific operators and resulting correlators for the scalar, pseudo-scalar and vector mesons are summarized below:

Scalar Meson ($J^{PC} = 0^{++}$) $\mathcal{M}_S(\vec{x},\tau) = \bar{\Psi}^{c,f_1}_{\alpha}(\vec{x},\tau)\Psi^{c,f_2}_{\beta}(\vec{x},\tau)$

$$G_S(\vec{x},\tau) = \langle\ (\gamma_5)_{\alpha\beta}U^{c_1c_2}_{\beta\gamma}(\gamma_5)_{\gamma\delta}D^{*c_1c_2}_{\alpha\delta}\ \rangle_U, \tag{3.6}$$

where $U \equiv M^{-1}(\kappa_u, x, 0)$ and $D \equiv M^{-1}(\kappa_d, x, 0)$ denote the inverse fermion matrix for the quark flavors $f_1 = u$ and $f_2 = d$, which are usually chosen to be degenerate. The expression $\langle\ \rangle_U$ should be understood as average over the gauge field configurations U according to (2.25), respectively (2.26).

Pseudo-scalar Meson ($J^{PC} = 0^{-+}$) $\mathcal{M}_{PS}(\vec{x},\tau) = \bar{\Psi}^{c,f_1}_{\alpha}(\vec{x},\tau)\ (\gamma_5)_{\alpha\beta}\ \Psi^{c,f_2}_{\beta}(\vec{x},\tau)$

Here the additional γ_5-matrix is eliminated in the correlator via the relation $D^\dagger = \gamma_5 D\gamma_5$, which was already used for the scalar meson

$$\begin{aligned} G_\pi(\vec{x},\tau) &= \langle\ U^{c_1c_2}_{\beta\gamma}D^{*c_1c_2}_{\beta\gamma}\ \rangle_U \\ G_K(\vec{x},\tau) &= \langle\ U^{c_1c_2}_{\beta\gamma}S^{*c_1c_2}_{\beta\gamma}\ \rangle_U, \end{aligned} \tag{3.7}$$

Hence the choice of the quark flavors $f_{1,2}$ determines the particle described with the above correlation function, which is the pion for u and d and the K meson for u and s quark flavors, where $S \equiv M^{-1}(\kappa_s, x, 0)$.

Vector Meson ($J^{PC} = 1^{--}$) $\mathcal{M}_V(\vec{x},\tau) = \bar{\Psi}^{c,f_1}_{\alpha}(\vec{x},\tau)\ (\gamma_k)_{\alpha\beta}\ \Psi^{c,f_2}_{\beta}(\vec{x},\tau)$

For u and d quark flavors this operator characterizes the ρ meson, while the K^* meson is given by u/d and s quark content. Since the operator includes the matrices γ_1, γ_2 or γ_3, the total correlator is obtained by summing over all three combinations

$$\begin{aligned} G_\rho(\vec{x},\tau) &= \frac{1}{3}\sum_{k=1}^{3}\langle\ (\gamma_k\gamma_5)_{\alpha\beta}U^{c_1c_2}_{\beta\gamma}(\gamma_k\gamma_5)_{\gamma\delta}D^{*c_1c_2}_{\alpha\delta}\ \rangle_U \\ G_{K^*}(\vec{x},\tau) &= \frac{1}{3}\sum_{k=1}^{3}\langle\ (\gamma_k\gamma_5)_{\alpha\beta}U^{c_1c_2}_{\beta\gamma}(\gamma_k\gamma_5)_{\gamma\delta}S^{*c_1c_2}_{\alpha\delta}\ \rangle_U. \end{aligned} \tag{3.8}$$

The four possible diquark states with a total anti-symmetric wave function were already introduced in table 3.1. Instead of the γ-matrices appearing in the meson operators the spin zero diquark states involve the combination of the charge conjugation matrix C with γ_5, which ensures the appropriate combination of the spinor indices. The ϵ-tensor provides the anti-symmetric color distribution for two quarks in the anti-triplet representation. In the following the fermion field notation is abbreviated according to the flavor content as $u^a_\alpha(x) \equiv \Psi^{a,u}_\alpha(\vec{x},\tau)$. The diquark correlators can be obtained in analogy to those for mesons, but unlike in the case of color singlet states they are gauge-variant observables. Therefore these correlation functions have to be calculated on gauge fixed configurations (see section 2.4). Note that for the flavor sextet diquarks with two u quarks two possible combinations for the quark propagator arise. This leads to a second term with negative sign due to the anti-commutation relation for the quark fields. The resulting correlation functions are listed below:

Diquark (Flavor $\bar{3}$, Spin 0, Color $\bar{3}$) $\mathcal{D}_{\bar{3}0\bar{3}}(\vec{x},\tau) = \epsilon_{abc}(C\gamma_5)_{\alpha\beta}u^a_\alpha(x)d^b_\beta(x)$

$$G_{\bar{3}0\bar{3}}(\vec{x},\tau) \;=\; \langle\ \epsilon_{abc}\epsilon_{def}(C\gamma_5)_{\alpha\beta}(C\gamma_5)_{\gamma\delta}U^{ad}_{\alpha\gamma}D^{be}_{\beta\delta}\ \rangle_U \tag{3.9}$$

Diquark (Flavor 6, Spin 1, Color $\bar{3}$) $\mathcal{D}_{61\bar{3}}(\vec{x},\tau) = \epsilon_{abc}u^a_s(x)u^b_s(x)$

$$G_{61\bar{3}}(\vec{x},\tau) \;=\; \langle\ \epsilon_{abc}\epsilon_{def}(U^{ad}_{s_1s_2}U^{be}_{s_1s_2} - U^{ae}_{s_1s_2}U^{bd}_{s_1s_2})\ \rangle_U \tag{3.10}$$

Diquark (Flavor $\bar{3}$, Spin 1, Color 6) $\mathcal{D}_{\bar{3}16}(\vec{x},\tau) = u^c_s(x)d^c_s(x)$

$$G_{\bar{3}16}(\vec{x},\tau) \;=\; \langle\ U^{c_1c_2}_{s_1s_2}D^{c_1c_2}_{s_1s_2}\ \rangle_U \tag{3.11}$$

Diquark (Flavor 6, Spin 0, Color 6) $\mathcal{D}_{606}(\vec{x},\tau) = (C\gamma_5)_{\alpha\beta}u^c_\alpha(x)u^c_\beta(x)$

$$G_{606}(\vec{x},\tau) \;=\; \langle\ (C\gamma_5)_{\alpha\beta}(C\gamma_5)_{\gamma\delta}(U^{c_1c_2}_{\alpha\gamma}U^{c_1c_2}_{\beta\delta} - U^{c_1c_2}_{\alpha\delta}U^{c_1c_2}_{\beta\gamma})\ \rangle_U\,. \tag{3.12}$$

Combining the $\bar{3}0\bar{3}$ diquark operator with an additional quark field yields the general form for the spin $\frac{1}{2}$ baryon operator

$$\mathcal{B}(\vec{x},\tau) = \epsilon_{abc}\Psi^{a,f_1}_\alpha(\vec{x},\tau)[\Psi^{b,f_2}_\beta(\vec{x},\tau)(C\gamma_5)_{\beta\gamma}\Psi^{c,f_2}_\gamma(\vec{x},\tau)]. \tag{3.13}$$

As described before, the anti-symmetric ϵ-tensor takes care of the color neutrality of the baryon, while the $(C\gamma_5)$-matrix ensures the correct spinor distribution of the quarks fields. Accordingly, the operators of the nucleon and the strange sigma baryon together with the corresponding correlators can be written as

Nucleon $\mathcal{B}_N(\vec{x},\tau) = \epsilon_{abc}u^a_\alpha(x)[u^b_\beta(x)(C\gamma_5)_{\beta\gamma}d^c_\gamma(x)]$

$$G_N(\vec{x},\tau) \;=\; \langle\ \mathrm{Tr}_{\alpha\delta}[\epsilon_{abc}\epsilon_{def}(C\gamma_5)_{\beta\gamma}(C\gamma_5)_{\epsilon\phi}\ (U^{ad}_{\alpha\delta}U^{be}_{\beta\epsilon}D^{cf}_{\gamma\phi} - U^{ae}_{\alpha\epsilon}U^{bd}_{\beta\delta}D^{cf}_{\gamma\phi})]\ \rangle_U \tag{3.14}$$

Sigma $\mathcal{B}_\Sigma(\vec{x},\tau) = \epsilon_{abc} u^a_\alpha(x)[u^b_\beta(x)(C\gamma_5)_{\beta\gamma} s^c_\gamma(x)]$

$$G_\Sigma(\vec{x},\tau) \;=\; \langle\ \mathrm{Tr}_{\alpha\delta}[\epsilon_{abc}\epsilon_{def}(C\gamma_5)_{\beta\gamma}(C\gamma_5)_{\epsilon\phi}\ (U^{ad}_{\alpha\delta}U^{be}_{\beta\epsilon}S^{cf}_{\gamma\phi} - U^{ae}_{\alpha\epsilon}U^{bd}_{\beta\delta}S^{cf}_{\gamma\phi})]\ \rangle_U. \tag{3.15}$$

The lambda baryon consists of the three light quark flavors u, d and s. Hence the operator contains the three possibilities to combine the spin of a quark pair to zero

Lambda $\mathcal{B}_\Lambda(\vec{x},\tau) = \epsilon_{abc}(C\gamma_5)_{\beta\gamma}[u^a_\alpha(x)d^b_\beta(x)s^c_\gamma(x)+d^a_\alpha(x)s^b_\beta(x)u^c_\gamma(x)-2s^a_\alpha(x)u^b_\beta(x)d^c_\gamma(x)]$

$$\begin{aligned}
G_\Lambda(\vec{x},\tau) \;=\; & \langle\ \mathrm{Tr}_{\alpha\delta}[\epsilon_{abc}\epsilon_{def}(C\gamma_5)_{\beta\gamma}(C\gamma_5)_{\epsilon\phi} \\
& \quad * (U^{ad}_{\alpha\delta}D^{be}_{\beta\epsilon}S^{cf}_{\gamma\phi} + D^{ad}_{\alpha\delta}U^{be}_{\beta\epsilon}S^{cf}_{\gamma\phi} + 4S^{ad}_{\alpha\delta}U^{be}_{\beta\epsilon}D^{cf}_{\gamma\phi} \\
& \quad - U^{ad}_{\alpha\epsilon}D^{be}_{\beta\delta}S^{cf}_{\gamma\phi} - D^{ad}_{\alpha\epsilon}U^{be}_{\beta\delta}S^{cf}_{\gamma\phi} - 2U^{ad}_{\alpha\epsilon}D^{be}_{\beta\phi}S^{cf}_{\gamma\delta} \\
& \quad -2D^{ad}_{\alpha\epsilon}U^{be}_{\beta\phi}S^{cf}_{\gamma\delta} - 2S^{ad}_{\alpha\epsilon}D^{be}_{\beta\phi}U^{cf}_{\gamma\delta} - 2S^{ad}_{\alpha\epsilon}U^{be}_{\beta\phi}D^{cf}_{\gamma\delta})]\ \rangle_U \\
\;=\; & \langle\ \mathrm{Tr}_{\alpha\delta}[\epsilon_{abc}\epsilon_{def}(C\gamma_5)_{\beta\gamma}(C\gamma_5)_{\epsilon\phi}(2U^{ad}_{\alpha\delta}U^{be}_{\beta\epsilon}S^{cf}_{\gamma\phi} + 4S^{ad}_{\alpha\delta}U^{be}_{\beta\epsilon}U^{cf}_{\gamma\phi} \\
& \quad -2U^{ad}_{\alpha\epsilon}U^{be}_{\beta\delta}S^{cf}_{\gamma\phi} - 4U^{ad}_{\alpha\epsilon}U^{be}_{\beta\phi}S^{cf}_{\gamma\delta} - 4S^{ad}_{\alpha\epsilon}U^{be}_{\beta\phi}U^{cf}_{\gamma\delta})]\ \rangle_U .
\end{aligned} \tag{3.16}$$

It is obvious from the above correlation function that the nine original components reduce to only five if the masses of the light quark flavors u and d are degenerate.

Finally, the H-dibaryon correlator is needed for the investigation of this particle on the lattice. As $SU(3)_F$ flavor singlet this six quark state contains two of each light quark flavors u, d and s. The explicit construction of the operator requires the symmetrization of the color and spinor indices of two triplets of quarks in order to obtain color and spin singlets as described in the last section. This procedure can be illustrated most suitable with the following operator notation for the different six quark combinations

$$(\mathsf{abcdef}) = \epsilon_{abc}\epsilon_{def}(C\gamma_5)_{\alpha\beta}(C\gamma_5)_{\gamma\delta}(C\gamma_5)_{\epsilon\phi}\mathsf{a}^a_\alpha(x)\mathsf{b}^b_\beta(x)\mathsf{c}^c_\epsilon(x)\mathsf{d}^d_\gamma(x)\mathsf{e}^e_\delta(x)\mathsf{f}^f_\phi(x).$$

The quark pairs ab, de and cf couple to spin zero, while the first three quarks (abc) and the last three ones (def) form each a colorless state. Using this notation the H-dibaryon operator can be written as [81]

$$\begin{aligned}
\mathcal{H}(\vec{x},\tau) \;&=\; (udsuds) + (usdusd) + (dsudsu) - 2(ussudd) - 2(dssduu) - 2(usudsd) \\
&=\; 3(udsuds) - 3(ussudd) - 3(dssduu),
\end{aligned}$$

where the additional relations

$$\begin{aligned}
(usdusd) \;&=\; (udsuds) - (dssduu) + (usudsd) \\
(dsudsu) \;&=\; (udsuds) - (ussudd) + (usudsd)
\end{aligned}$$

were employed to reduce the number of contributions to the H-dibaryon operator. Since two quarks fields of each flavor are contained in each part, the corresponding correlation function $G_H(\vec{x},\tau) = \langle \mathcal{H}(\vec{x},\tau)\mathcal{H}^\dagger(0)\rangle$ involves terms of the structure

$$(U_{11}U_{22} - U_{12}U_{21})(D_{11}D_{22} - D_{12}D_{21})(S_{11}S_{22} - S_{12}S_{21}). \tag{3.17}$$

Each quark can be combined with the first or the second one of the same flavor in the conjugate operator. The second term gets a minus sign due to the anti-commutation relations of the quark fields as already shown in the simple case of the diquarks. Taking the symmetry properties of the ϵ-tensor and the $(C\gamma_5)$-matrix under the interchange of two indices into account and considering only degenerate u and d quark flavors then yields the H-dibaryon correlation function in the compactified representation

$$\begin{aligned}
G_H(\vec{x},\tau) \;=\; & \langle\, \epsilon_{abc}\epsilon_{def}\epsilon_{ghi}\epsilon_{jkl}(C\gamma_5)_{\alpha\beta}(C\gamma_5)_{\gamma\delta}(C\gamma_5)_{\epsilon\phi}(C\gamma_5)_{\lambda\mu}(C\gamma_5)_{\rho\sigma}(C\gamma_5)_{\nu\tau} \\
& * \{\, (U^{ag}_{\alpha\lambda}U^{dj}_{\gamma\rho} - U^{aj}_{\alpha\rho}U^{dg}_{\gamma\lambda})\, [\, (U^{bh}_{\beta\mu}U^{ek}_{\delta\sigma} - U^{bk}_{\beta\sigma}U^{eh}_{\delta\mu})(S^{ci}_{\epsilon\nu}S^{fl}_{\phi\tau} - S^{cl}_{\epsilon\tau}S^{fi}_{\phi\nu}) \\
& \qquad +2\, (U^{bk}_{\beta\sigma}U^{el}_{\delta\tau} - U^{bl}_{\beta\tau}U^{ek}_{\delta\sigma})(S^{ch}_{\epsilon\mu}S^{fi}_{\phi\nu} - S^{ci}_{\epsilon\nu}S^{fh}_{\phi\mu}) \\
& \qquad +2\, (U^{eh}_{\delta\mu}U^{fk}_{\phi\sigma} - U^{ek}_{\delta\sigma}U^{fh}_{\phi\mu})(S^{bi}_{\beta\nu}S^{cl}_{\epsilon\tau} - S^{bl}_{\beta\tau}S^{ci}_{\epsilon\nu}) \\
& \qquad +2\, (U^{ek}_{\delta\sigma}U^{fl}_{\phi\tau} - U^{el}_{\delta\tau}U^{fk}_{\phi\sigma})(S^{bh}_{\beta\mu}S^{ci}_{\epsilon\nu} - S^{bi}_{\beta\nu}S^{ch}_{\epsilon\mu})\,] \\
& +2\, (U^{aj}_{\alpha\rho}U^{dl}_{\gamma\tau} - U^{al}_{\alpha\tau}U^{dj}_{\gamma\rho})(U^{eg}_{\delta\lambda}U^{fk}_{\phi\sigma} - U^{ek}_{\delta\sigma}U^{fg}_{\phi\lambda})(S^{bh}_{\beta\mu}S^{ci}_{\epsilon\nu} - S^{bi}_{\beta\nu}S^{ch}_{\epsilon\mu})\, \}\, \rangle_U\,.
\end{aligned}$$

Note that the actual calculation of this correlator in a lattice simulation involves loops over all the color and spinor indices, which is naturally very time consuming. Therefore it is absolutely necessary to consider that three out of four combinations of the spinor indices give no contribution to the correlation function due to the structure of the $(C\gamma_5)$-matrix (see appendix A). Moreover only 6 of 27 possible combinations of the color indices in the ϵ-tensor yield a non-zero result. Nevertheless the evaluation of the H-dibaryon correlation function involves the calculation of $\mathcal{O}(10^8)$ independent terms and requires a factor 150 more CPU-time than the calculation of a lambda baryon correlator.

3.3 Extracting Masses from Correlation Functions

As mentioned before particle masses can be obtained from the long range behavior of the correlation functions. In the case of the temporal correlator this yields the pole mass, while the exponential decay of the spatial correlator (usually in the z direction) determines the screening mass

$$\begin{aligned}
G(\tau) &= \int dx\; dy\; dz\; G(x,y,z,\tau) \\
G(z) &= \int_0^{1/T} d\tau \int dx\; dy\; G(x,y,z,\tau). \qquad (3.18)
\end{aligned}$$

The following considerations about the temporal correlation function and the pole mass can also be translated correspondingly for the spatial correlator and the screening mass.

Once the correlation function is calculated, a first estimate of the particle mass can be obtained from its effective mass at Euclidean time τ, which is defined as

$$m_{eff}(\tau) = \log\left(\frac{G(\tau)}{G(\tau{+}1)}\right). \qquad (3.19)$$

For small time separations the effective mass usually shows contributions of excited states, while it turns into a plateau of a constant ground state mass at larger times. For this reason one usually defines correlations functions which project onto states with definite momentum. Performing a Fourier transformation one obtains

$$\begin{aligned} G(\vec{p},\tau) &= \sum_x G(\vec{x},\tau) e^{-i\,\vec{p}\,\vec{x}} \\ &= \sum_n \left(A_n(\vec{p}) e^{-E_n(\vec{p})\tau} + B_n(\vec{p}) e^{-E_n(\vec{p})(N_\tau-\tau)} \right) . \end{aligned} \tag{3.20}$$

At large time separations this correlator at fixed momentum is dominated by the ground state energy $E_0(\vec{p}) = \sqrt{m_0^2 + \vec{p}^2}$. The projection onto zero momentum then yields simply the reduction to the ground state mass $E_0(0) = m_0$. The amplitudes obey the relation $B_n(\vec{p}) = \pm A_n(\vec{p})$ if the correlator $G(\vec{p},\tau)$ is even (odd) in the temporal direction. Hence the correlation function for $\vec{p} = 0$ is (anti-)symmetric around $N_\tau/2$, which is expressed in the different functional forms

$$G_{sym}(\tau) = 2A_0 \, e^{-m_0 \frac{N_\tau}{2}} \cosh\left(m_0 \left(\frac{N_\tau}{2} - \tau \right) \right) \tag{3.21}$$

$$G_{asym}(\tau) = 2A_0 \, e^{-m_0 \frac{N_\tau}{2}} \sinh\left(m_0 \left(\frac{N_\tau}{2} - \tau \right) \right) . \tag{3.22}$$

By using the appropriate ansatz as fit function, a Jackknife analysis (see section 2.5) of the particle mass can be performed. Ideally this procedure is completed by a two-mass fit according to

$$G_{sym}(\tau) = 2A_0 \, e^{-m_0 \frac{N_\tau}{2}} \cosh\left(m_0 \left(\frac{N_\tau}{2} - \tau \right) \right) + 2A_1 \, e^{-m_1 \frac{N_\tau}{2}} \cosh\left(m_1 \left(\frac{N_\tau}{2} - \tau \right) \right) ,$$

in order to eliminate efficiently the contributions of excited states at the first few time slices. Furthermore a stable plateau of the ground state mass should be obtained by leaving out successively data points at small time separations.

3.4 Extrapolation to the Physical Point

The resulting particle masses at different values of the bare quark mass have to be extrapolated to the chiral limit or to the physical quark mass value, respectively. As already introduced in section 2.1.2 the quark mass (2.14) is related to the squared mass of the pseudo-scalar meson in leading order chiral perturbation theory. Therefore a linear dependence of m_{PS}^2 on the quark mass can be assumed

$$m_{PS}^2 = b_{PS} \left(\frac{1}{\kappa} - \frac{1}{\kappa_c} \right) , \tag{3.23}$$

where κ_c is the critical hopping parameter at which the pseudo-scalar meson mass vanishes. For all other particle masses a similar relation is applicable

$$m = a + b \left(\frac{1}{\kappa} - \frac{1}{\kappa_c} \right) . \tag{3.24}$$

In the case of particles consisting of different quark flavors, like the strange hadrons investigated in the present study, the linear functions are understood in terms of the average quark mass

$$\frac{1}{\kappa} = \frac{1}{2}\left(\frac{1}{\kappa_{ud}} + \frac{1}{\kappa_s}\right). \tag{3.25}$$

This leads to a modified version of the relation (3.23) for the mass of the strange pseudoscalar K meson

$$m_K^2 = \frac{b_{PS}}{2}\left[\left(\frac{1}{\kappa_{ud}} - \frac{1}{\kappa_c}\right) + \left(\frac{1}{\kappa_s} - \frac{1}{\kappa_c}\right)\right] \tag{3.26}$$

and similarly to a modification of (3.24) for the other particles. Obviously an extrapolation to the physical values of the degenerate u and d quark mass as well as to the s quark mass is necessary. By keeping κ_s fixed, the second term in (3.26) becomes simply a constant, which allows to perform a linear fit in $1/\kappa_{ud}$ and an extrapolation to the physical bare quark mass. The latter can be determined from the ratio of two non-strange hadrons, like the pion, rho or nucleon, or alternatively from the ratio of one of these with the string tension.

Having fixed the physical κ_{ud}, the first term of the relation (3.26) is only a constant. Therefore a linear extrapolation in $1/\kappa_s$ leads to the physical point. The physical κ_s can be determined from the ratio of a strangeness carrying particle to a non-strange one. In the quenched approximation the different choices of the input particle masses produce deviations in a 10% range compared to the experimental values [44], whereas this effect can be reduced in simulations with dynamical fermions [82].

3.5 Improvement through the Fuzzing Technique

It was already mentioned that the excited states interfere with the clean exponential decay of the ground state in the correlation function. This observation inspired Gupta et. al. [83] to develop an improvement procedure, which was further explored by the *UKQCD* collaboration [84]. The so-called fuzzing technique provides a better overlap with the ground state, since it takes into account to some extent the physical size of the particle. The separation of a quark (anti-)quark pair by a suitable distance R thus will maximize the ground state contribution relative to the ones of the excited states already at small Euclidean times. The fuzzed quark field is constructed to be symmetric in all space directions (see figure 3.3)

$$\begin{aligned}\Psi^R(x) \quad = \quad & \frac{1}{6}\sum_{\mu=1..3} (\, U^\dagger(x-\hat{\mu}) \,..\, U^\dagger(x-R\hat{\mu})\Psi(x-R\hat{\mu}) \\ & \qquad + U(x) \,..\, U(x+(R-1)\hat{\mu})\Psi(x+R\hat{\mu}) \,). \end{aligned} \tag{3.27}$$

Such a fuzzed quark field is only used at the sink, while the one at the source remains local. For a general meson the fuzzed operator and the corresponding correlator can be written as

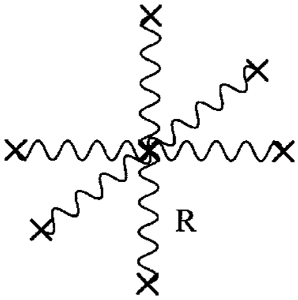

Figure 3.3: Fuzzed fermion operator with radius R.

$$\begin{aligned} G(\vec{x},\tau) &= \langle \mathcal{M}^R(\vec{x},\tau)\mathcal{M}^\dagger(0)\rangle \quad \text{with} \qquad (3.28)\\ \mathcal{M}^R(\vec{x},\tau) &= \bar{\Psi}^R_{\alpha,c,f_1}(\vec{x},\tau)\ (\Gamma)_{\alpha\beta}\ \Psi_{\beta,c,f_2}(\vec{x},\tau). \end{aligned}$$

This combination is referred to as local-fuzzed (LF) correlator. It would not be appropriate to use a fuzzed-fuzzed (FF) correlator, since some of the fuzzed links cancel each other, which would resemble the purely local correlator [84]. For the baryons two possible combinations arise, the (LLF) single-fuzzed and the (LFF) double-fuzzed correlator. They are visualized in figure 3.4, where each of the extended links is understood as a sum over the six spatial orientations. Doubling the quark content of a baryon leads to a dibaryon operator in the (LLLLFF) and the (LLFFFF) representation.

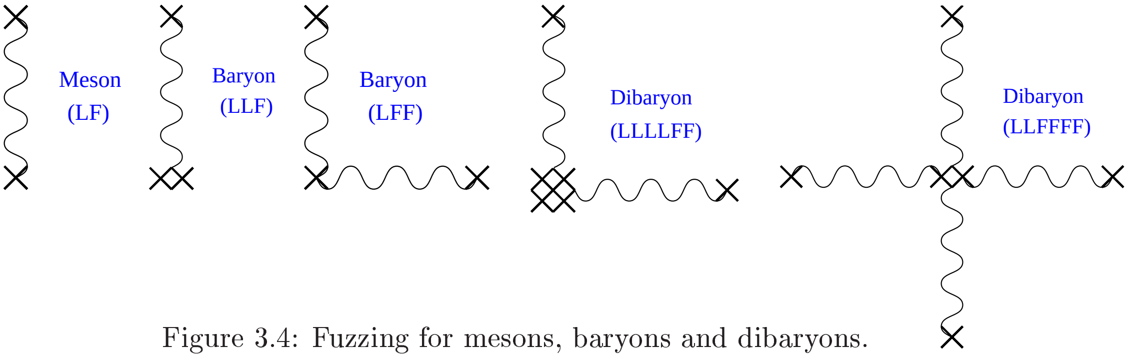

Figure 3.4: Fuzzing for mesons, baryons and dibaryons.

In addition to the quark fields also the distribution of the gluon fields can be improved. The desired approach should imitate the gluon cloud which surrounds the quark fields. This is commonly achieved by the iterative APE smearing procedure [85]

$$U_{new}(x,\mu) \;=\; \mathcal{P}_{SU(3)}\left(c\,U_{old}(x,\mu) \;+ \sum_{\pm\nu\neq\mu<4} U_{staples}(x,\nu)\right), \qquad (3.29)$$

where the staples () with three links perpendicular to the gauge field and the time direction are added to the simple link. This is followed by the back projection to the $SU(3)$ symmetry group. Some trials with different parameters c and varying number of iteration steps have shown [84], that the choice of $c = 2$ and at least eight iteration steps leads to an efficient smearing of the gauge fields.

The effect of the fuzzing and smearing procedures is now further explored for the H-dibaryon correlation function. It is obvious from the correlator as well as from the effective mass plot in figure 3.5, that already the fuzzing of two quarks yields a considerable reduction of contributions from excited states. The best results were obtained by applying the fuzzing technique for four of the six quarks, where an almost constant value for up to five time separations could be achieved. The remaining contributions of excited states at small time separations were efficiently absorbed in the fits with two exponentials.

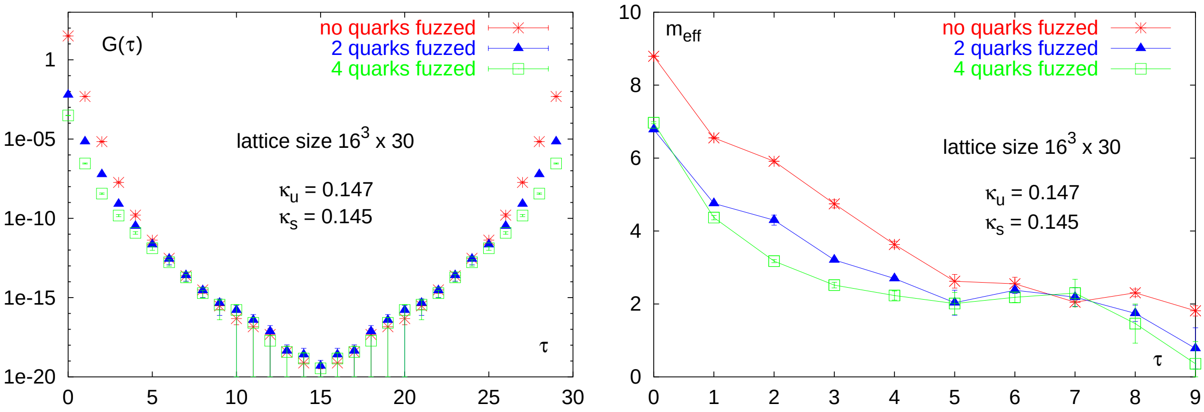

Figure 3.5: Influence of the fuzzing technique on the H-dibaryon correlation function and the effective masses.

3.6 Hadron Spectrum

For the detailed analysis of the stability of the H-dibaryon a spectrum calculation was performed in quenched QCD with improved gauge and fermion actions. In the gauge sector the (1,2) Symanzik improved action (2.6) was used with a gauge coupling $\beta = 4.1$. The lattice spacing was determined from the string tension to a=0.177(8)fm [4], or equivalently a^{-1}=1.11(5) GeV. The Clover fermion action was used with tree-level clover coefficient, since non-perturbatively improved coefficients are not yet available for the employed gauge action (see also section 2.1.2). In order to study the finite size effects, simulations of the strange hadrons as well as the H-dibaryon were performed on four lattice sizes $(8{-}24)^3 \times 30$. The number of configurations ranges from 120 for the smallest to 20 for the largest lattice. They are separated by 100 sweeps of four overrelaxation and one heatbath step each. The correlators were calculated for three different κ_{ud} and up to five κ_s values. On these fairly coarse lattices a fuzzing radius $R = 4$ has been chosen in order to obtain a broad plateau for effective masses as an approximation for the H-dibaryon ground state mass.

The physical κ_{ud} value was determined from a previous simulation of the light hadron spectrum [74, 75] with the same parameters as above, but on a $16^3 \times 32$ lattice and on the basis of in total 292 quark propagators. Adjusting the particle ratios m_π/m_N, $m_\pi/\sqrt{\sigma}$ and $m_N/\sqrt{\sigma}$ to the experimental values leads to very similar results for the hopping parameter $\kappa_{ud} = 0.1490(1)$, which corresponds to the physical value of the light quark masses.

3.6.1 Strange Particle Masses

The strange particle masses were determined with one- and two-state fits during a Jackknife analysis (see sec. 2.5) as illustrated the section 3.3. The masses obtained in this way are summarized in the tables B.1-B.4 of the appendix. The strange particle masses for all

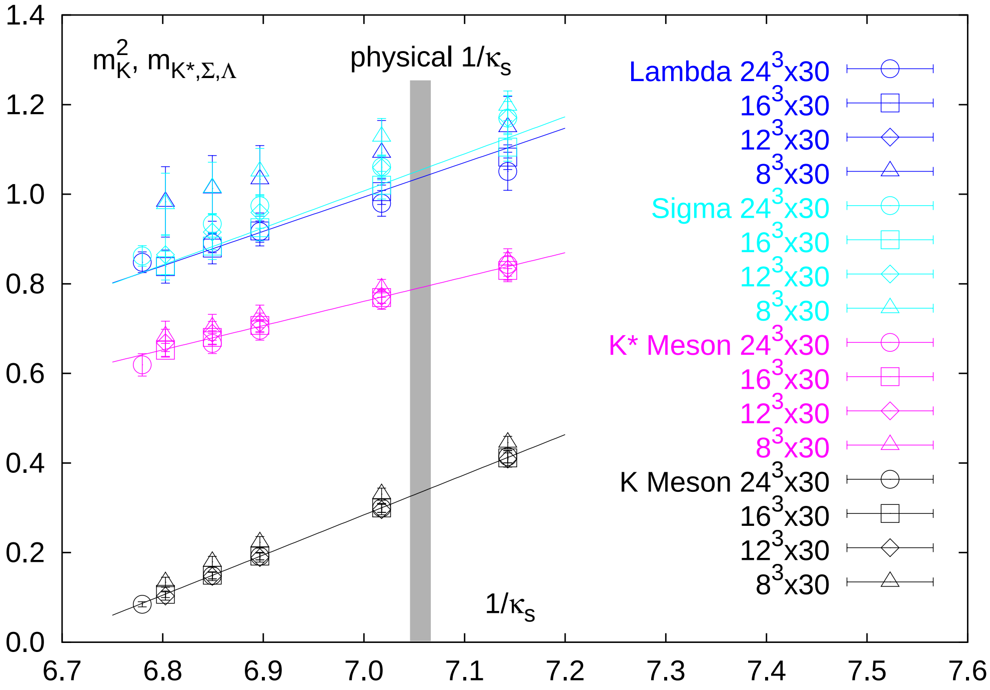

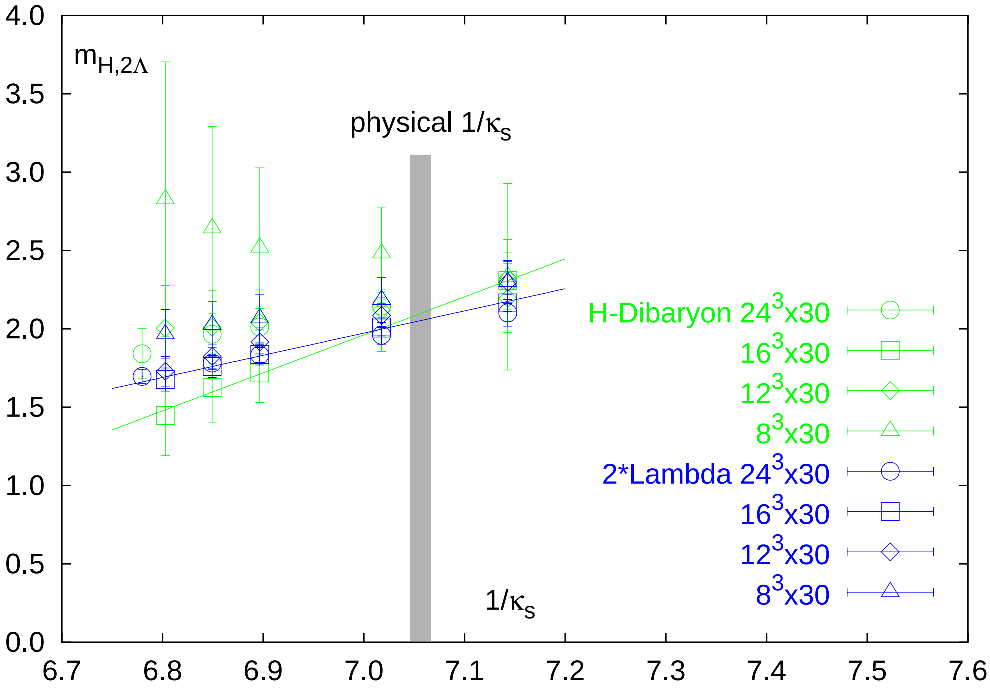

Figure 3.6: Strange hadron (top) and H-dibaryon masses (bottom) at physical κ_{ud} mass.

lattice sizes are displayed in figure 3.6, where the linear extrapolation to the physical κ_{ud}-value was already performed. Hence the particle masses depend only on the strange quark mass. The lines should guide the eye and indicate the results of linear fits for the $16^3 \times 30$ lattice data.

In general one observes a good agreement of the strange hadron masses on the different lattice sizes. Only the results of the smallest $8^3 \times 30$ lattice are slightly overestimated. This effect is more pronounced for the baryons in comparison to the mesons, since the finite size effects increase with the size of the simulated particle. That is even more obvious from figure 3.6 (bottom), where strong deviations can be observed for the H-dibaryon on the smallest lattice which has an spatial extension of only $L = 1.4$ fm.

Before the difference between the H-dibaryon and two Λ masses is investigated in detail, the plotted region for the physical s quark mass should be explained. In order to absorb as many quenching effects as possible, the physical κ_s should be set by the ratio m_Λ/m_N. Here the contact to physical units was made by the nucleon mass $m_N = \hat{m}_N a^{-1} = 939$ MeV as an input, which yields a^{-1}=1.12(1) GeV. This procedure leads to only small deviations in the range 2-5% compared to the experimental values of the Σ baryon and the K^* meson on the largest lattices, while the K meson was found to be about 20% heavier. This effect could also be observed in a similar study [39].

Inspired by the good agreement of the Σ and K^* meson masses with the experimental values, the scale was set alternatively by the ratios m_Σ/m_N and m_{K^*}/m_N. The obtained particle masses for different input choices are collected in table B.5. Since it is desirable to define a common physical κ_s-value for a comparison of the results on all lattice sizes, the average over the κ_s-values on the two larger lattices was taken, which yields deviations of no more than 5% for the non-adjusted particle masses. The mean value $\kappa_s = 0.1417(2)$ is indicated as physical κ_s-region in the plots 3.6 and 3.7. The particle masses for this mean κ_s-value can also be found in table B.5.

3.6.2 H-Dibaryon Stability

Now all prerequisites are available to discuss the investigation of the H-dibaryon stability. The difference between the H-dibaryon and twice the lambda mass is illustrated in detail in figure 3.7. The slope of a linear fit in $1/\kappa_s$ would be quite different for varying lattice sizes. For the largest lattice almost a constant behavior can be observed, whereas the values of the $16^3 \times 30$ lattice are rising with increasing strange quark mass. On the contrary the data points of the two smaller lattices exhibit a negative slope fitted linear in $1/\kappa_s$. Nevertheless the results on all lattice sizes have in common that a value around zero is expected in the physical region. This would mean that the examined H-dibaryon state is simply the unbound composition of two lambda baryons.

Finally, the dependence of this result on the different choices of the input particle mass should be investigated. Figure 3.8 shows the difference in mass $(m_H - 2m_\Lambda)/2m_\Lambda$ at the

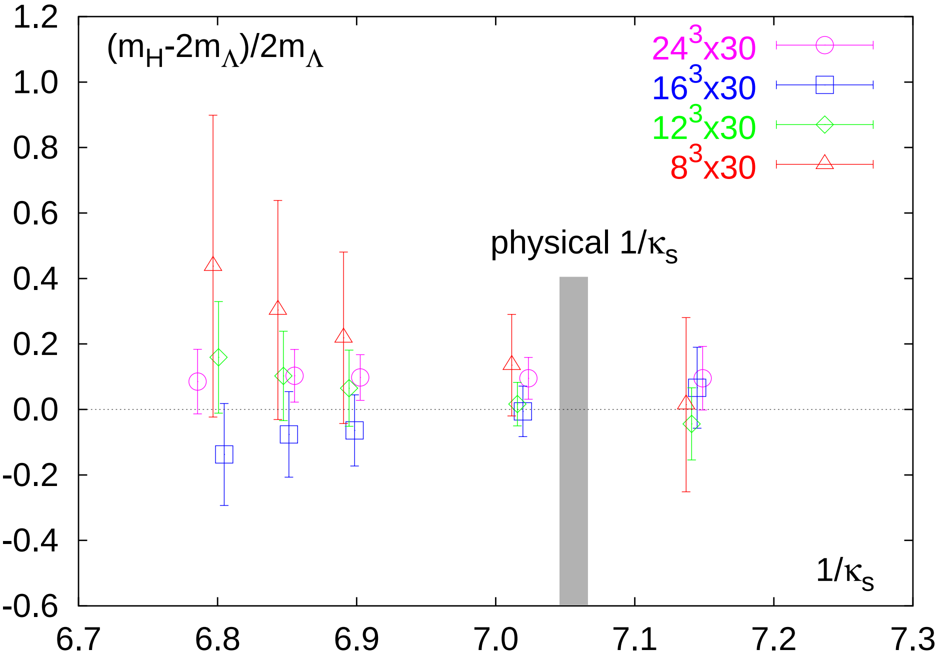

Figure 3.7: Difference of H-dibaryon and 2*lambda masses for all lattice sizes (Data points are slightly displaced in κ_s^{-1} for better visibility).

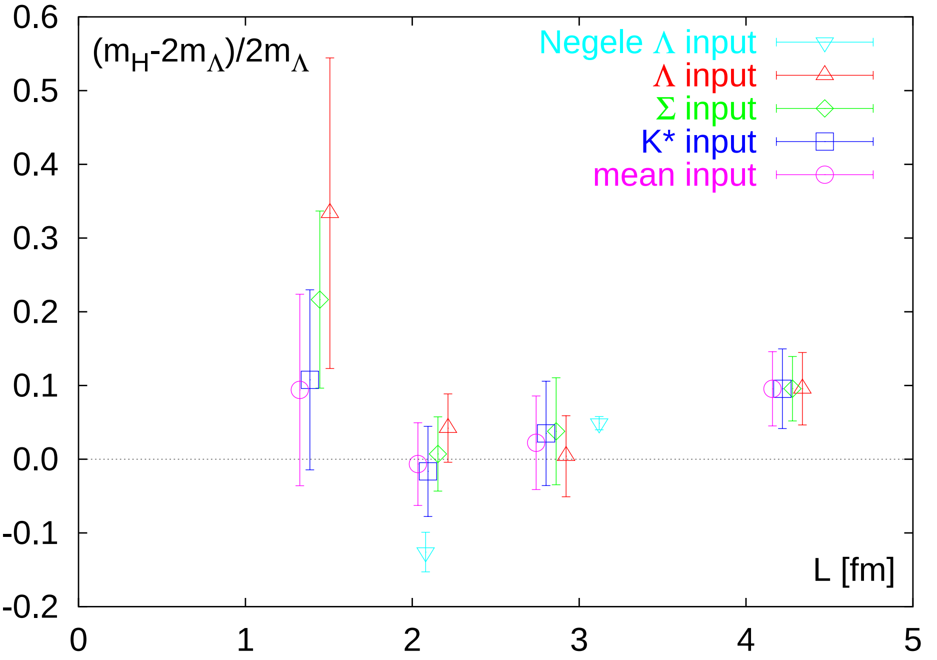

Figure 3.8: Difference of H-dibaryon and 2*lambda masses for different input (Data points are slightly displaced in L for better visibility).

physical u/d and s quark values for the experimental input of the Λ, Σ and K^* masses as well as for the formerly described mean value of κ_s. The finite size effects are obvious for the smallest lattice with $L = 1.4$ fm, especially for the Λ input. On the intermediate lattices the values scatter around zero depending on the different input masses, while the points for the largest lattice with $L = 4.2$ fm lie slightly above. Here the limited statistics of only 20 configurations on the $24^3 \times 30$ lattice should be taken into account.

Taking the results on all lattice sizes into account leads to the conclusion, that an unbound H-dibaryon state consisting of two lambda baryons has been observed. Otherwise a lighter H-dibaryon should have been found, as in the case of the smaller lattice ($L = 2.1$ fm) of the study of Negele et. al. [39], which is also indicated in figure 3.8. The authors could not rule out considerable finite size effects on this lattice. Therefore a further investigation on a larger $24^3 \times 30$ lattice with $L = 3.1$ fm had been performed, which is in much better agreement with the results of the present thesis. Hence a common conclusion arises from the recent and present studies: The H-dibaryon does not exist as stable particle in the vacuum. It seems to be unbound at least within quenched QCD.

Two previous attempts to calculate the H-dibaryon mass on the lattice were reported in the literature more than a decade ago (see also table 1.1). The first calculation of Mackenzie and Thacker [36] on a fairly small lattice resulted also in an unbound H-dibaryon, while Iwasaki et. al. [37] observed a strongly bound H-dibaryon in a further simulation with the renormalization group improved gauge action. This calculation suffered from the limited statistics of only 15 configurations and quite large bare quark masses. In a subsequent paper [38] the authors realized that the difference in mass $2m_\Lambda - m_H$ was considerably decreased in a simulation with the standard plaquette action, which sheds a different light on the observation of a strongly bound H-dibaryon.

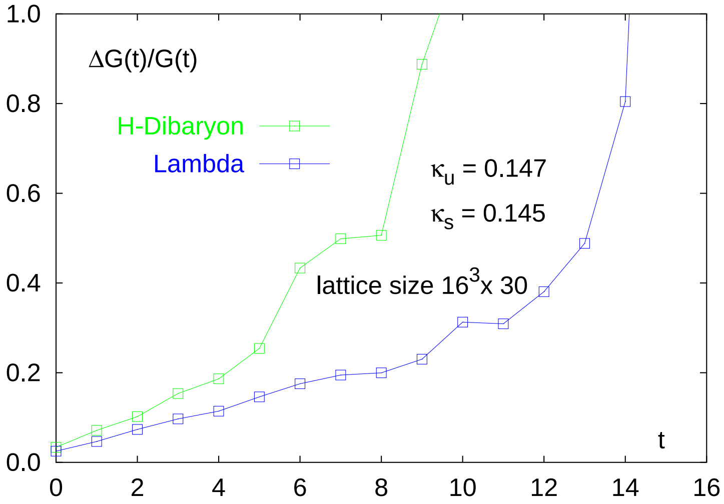

Figure 3.9: Relative error of H-dibaryon and lambda correlation functions.

In order to complete this section about strange hadronic matter, a short outlook on further lattice simulations in this field should be added. In figure 3.9 the relative error of the H-dibaryon and lambda correlators are illustrated. It can be observed that the error rises only linearly with the baryon number of the investigated state. Therefore it seems possible in the future to examine larger strangelets or even multi-quark clusters in lattice simulations, once the efficiency of the available parallel machines has increased sufficiently.

Chapter 4

Hadron Spectral Functions

So far only hadron spectra at zero temperature have been discussed. Now the focus is on the modifications of spectra which may arise from the presence of a thermal medium. In this last chapter the possibilities of the spectral analysis of hadronic correlation functions with the **M**aximum **E**ntropy **M**ethod (MEM) are described. The first section 4.1 gives an introduction into the relevance of spectral functions in QCD. After a presentation of the main principles of MEM in section 4.2, the numerical algorithm will be explained in greater detail in 4.3.

Section 4.4 shows the (in)dependence of the obtained spectral function under changes of the input parameters. The following two parts illustrate the resulting spectral functions for meson (sec. 4.5) and diquark (sec. 4.6) correlation functions at zero temperature, whereas the last section 4.7 demonstrates the applicability of this method to mesonic correlation functions at finite temperature.

4.1 Spectral Functions in QCD

Recent lattice calculations of static observables, like hadron masses and decay constants at zero temperature, have reached a quite satisfactory precision [82, 86]. At finite temperature it is desirable to get access to dynamic quantities, in particular spectral functions and real-time correlation functions, starting from the temporal correlators in Euclidean time calculated on the lattice. Furthermore modifications of hadronic properties at finite temperature and density could be studied in terms of changes of the spectral shape. The analysis of temporal as well as spatial correlation functions in the vicinity of the critical temperature gives evidence of substantial changes in the properties of hadronic states between the confined phase and the hot plasma phase of QCD [13, 14, 16, 87]. In order to judge if the observed modifications of hadron correlators are indeed related to the disappearance of hadron bound states a detailed study of the structure of spectral functions is required.

Moreover, spectral functions are directly related to the experimental annihilation cross sections. For example, a temperature dependence of the vector meson mass and width is linked to changes of the dilepton spectrum, whereas thermal effects on the pseudoscalar correlator influence the chiral condensate. These phenomena can be examined in relativistic heavy ion collisions [88, 89].

At very high temperatures beyond the phase transition thermodynamic observables can be calculated perturbatively in the framework of the hard thermal loop (HTL) resummed theory [90]. In a recent study [91] the HTL-resummed scalar spectral function was calculated for vanishing momentum. In comparison with the free thermal spectral function an enhancement at low energies as well as a suppression in the high energy regime can be observed. The former is due to the interaction between quarks and gluons in the heatbath, whereas the latter results from the influence of the thermal quark mass (Debye screening). The obtained mesonic correlation functions can be compared to lattice results for temperatures larger than $T \simeq 2T_c$. The HTL-resummed vector spectral function diverges for small energies, hence the corresponding correlator is divergent. Therefore a direct comparison of the vector correlation function calculated on the lattice with HTL-resummed perturbation theory is not possible. This makes it even more important to perform lattice calculations on large spatial lattices in order to explore the non-perturbative part of the spectral functions at low momenta.

In general the thermal two-point function for a specific hadronic observable $\mathcal{O}$ at Euclidean time $\tau \in [0, 1/T]$ in coordinate space is given by the infinite sum

$$\begin{aligned} G(\tau, \vec{x}) &= \langle \mathcal{O}(\tau, \vec{x}) \mathcal{O}^\dagger(0, \vec{0}) \rangle \\ &= T \sum_{n=-\infty}^{+\infty} \int \frac{d^3p}{(2\pi)^3} \, e^{-i(\omega_n \tau - \vec{p}\vec{x})} \, \hat{G}(\omega_n, \vec{p}). \end{aligned} \tag{4.1}$$

The Fourier transformed correlation function $\hat{G}(\omega_n, \vec{p})$ depends on the discrete Matsubara modes, i. e. $\omega_n = 2n\pi T$ for bosons. The spectral function $A(\omega, \vec{p})$ can be determined from the imaginary part of the momentum space correlator

$$\hat{G}(\omega_n, \vec{p}) = \int_{-\infty}^{+\infty} \frac{A(\omega, \vec{p})}{\omega - i\omega_n} \, d\omega \quad \Longrightarrow \quad A(\omega, \vec{p}) = \frac{1}{\pi} \, \mathrm{Im} \, \hat{G}(\omega_n, \vec{p}). \tag{4.2}$$

Using both the equations (4.1) and (4.2) together with the identity

$$T \sum_n \frac{e^{-i\omega_n \tau}}{\omega - i\omega_n} = \frac{e^{-\tau\omega}}{1 - e^{-\omega/T}} \qquad \text{with} \qquad 0 \leq \tau < \frac{1}{T} \tag{4.3}$$

for the Fourier transform of the free boson propagator, the spectral representation of the thermal correlation function in the coordinate space at fixed momentum can be written as

$$\begin{aligned} G(\tau, \vec{p}) &= T \sum_n e^{-i\omega_n \tau} \hat{G}(\omega_n, \vec{p}) \\ &= \int_{-\infty}^{+\infty} T \sum_n \frac{e^{-i\omega_n \tau}}{\omega - i\omega_n} \, A(\omega, \vec{p}) \, d\omega \end{aligned}$$

$$
\begin{aligned}
&= \int_{-\infty}^{+\infty} \frac{e^{-\tau\omega}}{1-e^{-\omega/T}}\, A(\omega,\vec{p})\; d\omega \\
&= \int_{0}^{\infty} \frac{e^{-\tau\omega}+e^{(\tau-1/T)\omega}}{1-e^{-\omega/T}}\, A(\omega,\vec{p})\; d\omega \\
&= \int_{0}^{\infty} \frac{\cosh(\omega(\tau-1/2T))}{\sinh(\omega/2T)}\, A(\omega,\vec{p})\; d\omega \\
&\equiv \int_{0}^{\infty} K(\tau,\omega)\; A(\omega,\vec{p})\; d\omega. \qquad (4.4)
\end{aligned}
$$

The function $K(\tau,\omega)$ is the integral kernel in the continuum representation, which is essential for the MEM analysis. It can easily be verified that this kernel reduces to $K(\tau,\omega) = e^{-\tau\omega}$ at zero temperature ($T \to 0$). This version will be referred to as exponential kernel. In the following only correlation and spectral functions at fixed momentum $\vec{p} = 0$ will be considered, therefore the label $\vec{p}$ is omitted from now on.

The last line of equation (4.4) shows that a given data set $D(\tau) \equiv G(\tau,0)$ for the correlator and the corresponding spectral function $A(\omega)$ are related by an inverse Laplace transform. Unfortunately lattice calculations can only provide the correlation function for a discrete set of Euclidean times τ. The number of data points is much smaller than the desired number of sampling points needed to reconstruct the spectral function. This is a typical example for an ill-posed problem, where the standard χ^2-fitting procedure is inapplicable. Furthermore the data are noisy due to the Monte Carlo sampling.

So far the analytic continuation from imaginary to real-time correlation functions was performed by strict assumptions on the spectral shape, for example a δ-function representing the pole mass plus a continuum-like structure [92, 93, 94]. Such an approach inhibits to probe the fine structure of the spectral function. Further difficulties arise at finite temperature, where very little is known about the spectral shape. The Maximum Entropy Method is a new approach to tackle this problem by use of Bayesian methods of interference. It provides a procedure to estimate suitable spectral functions from given data in Euclidean time which requires no a priori assumptions on the spectral shape.

4.2 Principles of the Maximum Entropy Method

The **M**aximum **E**ntropy **M**ethod is a well known technique in condensed matter physics, image reconstruction and astronomy [17, 95, 96]. In lattice QCD it has recently been applied to analyze meson correlation functions at zero temperature [18]. It could be demonstrated that this method correctly detects the location of poles in the correlation function and, moreover, is sensitive to the contribution of higher excited states in the correlators [97, 98]. Furthermore the spectral functions allow the determination of decay constants from the area below sharp peaks [98].

The framework of Bayesian interference in probability theory provides a powerful tool to find the most probable spectral function. The basic formula is given by the Bayes Theorem of conditional probability $P[X|Y]$ for the event X given Y

$$P[X|Y] = \frac{P[Y|X]\,P[X]}{P[Y]}. \tag{4.5}$$

The **posterior probability** for the spectral function $A(\omega)$ given the data points $D(\tau)$ for a correlation function in imaginary time is now accordingly determined as

$$P[A|DH] = \frac{P[D|AH]\,P[A|H]}{P[D|H]} \quad \text{with} \quad \begin{array}{rcl} P[D|AH] & \sim & \exp(-L) \\ P[A|H] & \sim & \exp(\alpha S), \end{array} \tag{4.6}$$

where $P[D|H]$ is only a normalization factor, which is independent of the spectral function. $P[D|AH]$ is called the **likelihood function** and $P[A|H]$ the **prior probability** [17]. H includes all prior knowledge about the spectral function, such as the positivity $A(\omega) \geq 0$ for $\omega \geq 0$ [99].

The central limit theorem provides the functional form of the likelihood function $P[D|AH]$ in (4.6) for the case of a large number of measurements. It can be expressed in terms of the usual χ^2 distribution

$$L = \frac{1}{2}\chi^2 = \frac{1}{2}\sum_{ij}(F(\tau_i) - D(\tau_i))C_{ij}^{-1}(F(\tau_j) - D(\tau_j)), \tag{4.7}$$

where $D(\tau_i)$ is the average over all measurements. C_{ij} denotes the symmetric covariance matrix, which has already been defined in equation (2.37). Employing equation (4.4), the fit function

$$F(\tau_i) = \int_0^\infty K(\tau_i,\omega)A(\omega)\,d\omega \,\hat{=} \sum_j K_{ij}A_j \tag{4.8}$$

is obtained in the discretized version by means of a predefined kernel $K_{ij} \equiv K(\tau_i,\omega_j)$ and the spectral function $A_j \equiv A(\omega_j)\Delta\omega$.

Maximizing the likelihood function $P[D|AH]$ corresponds to minimizing χ^2, which is the commonly used fitting procedure, where only a few parameters are adjusted. But for the addressed ill-posed problem, the influence of the prior probability plays an important role. At variance with the maximum likelihood method, in addition one has to maximize the prior probability $P[A|H] \sim \exp(\alpha S)$, which depends on the factor α and the entropy S.

The Shannon-Jaynes entropy can be constructed from axiomatic requirements such as subset and system independence, coordinate invariance and scaling [18, 100]. This leads to the following expression for the entropy

$$\begin{aligned} S &= \int_0^\infty \left[A(\omega) - m(\omega) - A(\omega)\log\left(\frac{A(\omega)}{m(\omega)}\right)\right] d\omega \\ &\hat{=} \sum_j \left[A(\omega_j) - m(\omega_j) - A(\omega_j)\log\left(\frac{A(\omega_j)}{m(\omega_j)}\right)\right] \Delta\omega, \end{aligned} \tag{4.9}$$

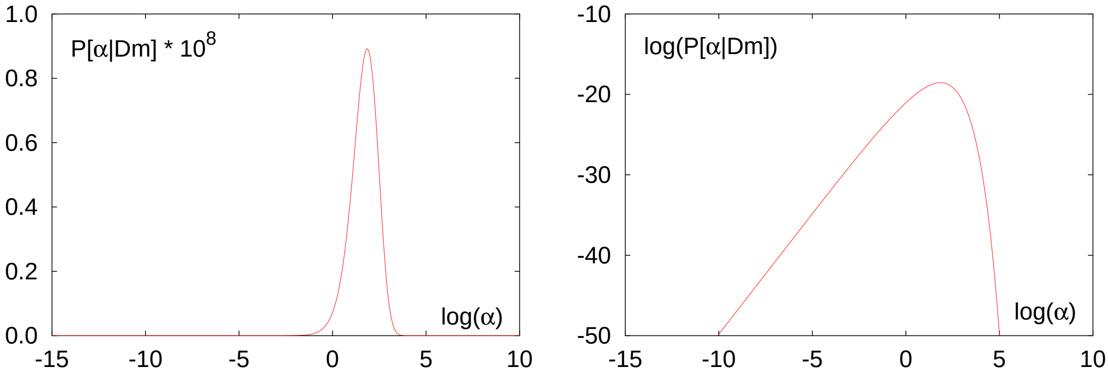

Figure 4.1: Sharply peaked posterior distribution $P[\alpha|Dm]$ of the weight factor α given the data (left) and its logarithm $\log(P[\alpha|Dm])$ (right) for the pion at 0.6 T_c at $\kappa = 0.1346$.

where the default model $m(\omega)$ incorporates any a priori knowledge about the spectral function $A(\omega)$. In the absence of any information about the data, the entropy is maximized with $A(\omega) \equiv m(\omega)$. For the studies of meson correlation functions $m(\omega) = m_0\ \omega^2$ is used as the initial ansatz for $A(\omega) \equiv \rho(\omega)\ \omega^2$. This default model is motivated by the asymptotic behavior of the spectral function at high energies, which can be studied in perturbative QCD. The influence of the choice of the model on the final spectral function is analyzed in section 4.4.

The real and positive factor α in the prior probability $P[A|H] = P[A|\alpha m] \sim e^{\,\alpha S}$ controls the relative weight between the entropy and likelihood function. For large α the fit is mostly influenced by the default model, whereas for small α the spectral function tends to fit the lattice data. The final result is independent of α because an integration over this parameter is performed.

The most probable spectral function $\hat{A}_\alpha(\omega)$ for given α is then obtained by maximizing $P[A|DH] = P[A|D\alpha m]$. It can easily be seen from (4.6) that this is equivalent to finding a maximum of $Q \equiv \alpha S - L$. The final spectral function $\bar{A}(\omega)$ is determined from a weighted average over α

$$\bar{A}(\omega) = \int \mathcal{D}A \int d\alpha\ A(\omega) P[A|D\alpha m] P[\alpha|Dm] \simeq \int d\alpha\ \hat{A}_\alpha(\omega) P[\alpha|Dm]. \tag{4.10}$$

The above approximation is valid for a sharply peaked distribution $P[A|D\alpha m]$. The weight factor $P[\alpha|Dm]$ can be obtained in applying Bayes Theorem (4.6)

$$\begin{aligned} P[\alpha|Dm] &\sim \int \mathcal{D}A\ P[D|A\alpha m]\ P[A|\alpha m]\ P[\alpha|m] \\ &\sim P[\alpha|m] \int \mathcal{D}A\ \exp(\alpha S - L) \end{aligned} \tag{4.11}$$

It usually turns out that the weight factor $P[\alpha|Dm]$ is sharply peaked around a unique value $\hat{\alpha}$ for data with a small error (see figure 4.1). Therefore a Gaussian approximation of $P[\alpha|Dm]$ can be used, which will be explained in the next section.

The most probable spectral function can be found from the condition for an extremum (maximum) making use of the Bryan algorithm ([101], see also sec. 4.3)

$$\nabla_{\!A} Q = \alpha \nabla_{\!A} S - \nabla_{\!A} L = 0. \tag{4.12}$$

The uncertainty of the solution is then contained in the second derivative of Q with respect to the spectral function A, namely $(\nabla\nabla Q)^{-1}$. Since one is interested in error bars for certain regions (peaks) of $A(\omega)$, the average spectral function in the frequency range $I = [\omega_k, \omega_l]$ must be calculated for a given α [18]

$$\langle A_\alpha \rangle_I \;\simeq\; \frac{\int_I \; A_\alpha(\omega)\; d\omega}{\int_I \; d\omega} \;=\; \frac{\sum_{j\in I} A_\alpha(\omega_j)\; \Delta\omega}{(l-k+1)\; \Delta\omega}. \tag{4.13}$$

The error in this region is then obtained from the variance

$$\langle (\delta A_\alpha)^2 \rangle_I \;\simeq\; -\frac{\int_{I\times I} \; (\nabla\nabla Q)^{-1}\; d\omega\; d\omega'}{\int_{I\times I} \; d\omega\; d\omega'}, \tag{4.14}$$

where $(\nabla\nabla Q)^{-1}$ is given by equation (4.25). Having calculated the mean and variance for the spectral function in the desired ω-ranges at every given α, the final result can be calculated via the integration over α similar to equation (4.10)

$$\begin{aligned} \langle \bar{A}(\omega) \rangle_I \;&\simeq\; \int d\alpha \; \langle A_\alpha \rangle_I \; P[\alpha|Dm] \\ \langle (\delta A)^2 \rangle_I \;&\simeq\; \int d\alpha \; \langle (\delta A_\alpha)^2 \rangle_I \; P[\alpha|Dm]. \end{aligned} \tag{4.15}$$

4.3 Details of the Algorithm

This section should serve as a guideline through the algorithmic details described in [101] by R. K. Bryan. The most complicated part of MEM is maximizing $Q = \alpha S - L$, or equivalently solving $\nabla Q = \alpha \nabla S - \nabla L = 0$ in order to obtain a global maximum. First of all, the derivatives with respect to the spectral function A can be calculated

$$\begin{aligned} \nabla S \;&=\; \sum_j -\log\left(A_j/m_j\right) \qquad \text{with} \qquad A_j/m_j \equiv A(\omega_j)/m(\omega_j) \\ \nabla L \;&=\; \frac{\partial F}{\partial A}\,\frac{\partial L}{\partial F} = K^T\,\frac{\partial L}{\partial F}. \end{aligned} \tag{4.16}$$

For the kernel K a singular value decomposition (SVD) is performed. The $N_\tau \times N_\omega$ kernel matrix can be written as product $K = V\;\Sigma\;U^T$, where U and V are orthogonal matrices and Σ is a diagonal matrix with the ordered singular values σ_i. Since some of the singular values are very small or even zero for an ill-conditioned matrix, the space can be reduced to the singular space with the dimension $N_s \le N_\tau$. Using a condition like $\sigma_{min} > 10^{-6}\;\sigma_{max}$ to determine the size of this space, one obtains the N_s singular values, the $N_\omega \times N_s$ matrix $U^{(s)}$ and $N_\tau \times N_s$ matrix $V^{(s)}$ in the reduced space.

Since the spectral function is positive semi-definite, it now can be parametrized using the orthogonal matrix $U \equiv U^{(s)}$ and a vector u in the singular space

$$A_j = m_j \ \exp \sum_{k=1}^{N_s} U_{jk} u_k. \tag{4.17}$$

This yields the enormous advantage that the $N_\omega = \mathcal{O}(10^2)$ dimensional discretized spectral function can be expressed in terms of an only N_s dimensional vector u.

Inserting the formulas (4.16) and (4.17) into equation (4.12), the condition for an extremum in the singular space can be rewritten as

$$-\alpha\, u = \Sigma\, V^T \, \frac{\partial L}{\partial F} \equiv g. \tag{4.18}$$

Now a standard Newton search can be performed for the function $f(u) = -\alpha u - g$, starting with any arbitrary u-vector

$$-\frac{\partial f(u)}{\partial u}\, \delta u = f(u) \qquad \Longrightarrow \qquad \left(\alpha\, \mathbb{1} + \frac{\partial g}{\partial u} \right) \delta u = -\alpha\, u - g. \tag{4.19}$$

The derivative of g with respect to u can be calculated by

$$\frac{\partial g}{\partial u} = \Sigma\, V^T \, \frac{\partial^2 L}{\partial F^2} \, V \, \Sigma \, U^T \, \mathrm{diag}\{A\} \, U \qquad \text{with} \qquad \frac{\partial^2 L}{\partial F^2} = C^{-1}. \tag{4.20}$$

In the context of MEM it is more suitable to set $u = 0$ in the beginning, which corresponds to a start with the default model (see equation (4.17)). In order to guarantee the lowest order approximation of the Newton search, the step size δu must be restricted. Therefore an auxiliary parameter μ is introduced in formula (4.19)

$$\left((\alpha + \mu)\, \mathbb{1} + \frac{\partial g}{\partial u} \right) \delta u = -\alpha\, u - g, \tag{4.21}$$

such as $\delta u^T \, U^T \, \mathrm{diag}\{A\} \, U \, \delta u \leq \mathcal{O}(\sum_j A_j)$ is fulfilled. The iteration starts with $\mu = 0$ and proceeds e.g. in multiplying μ by 10, beginning with $\mu = \alpha/10000$ [18]. If the norm condition is satisfied, the step size is small enough for a reasonable update of the solution vector $u' = u + \delta u$. This procedure is then iterated until the general stopping criterion for convergence is reached, which checks for equal length of the gradients

$$\frac{2 \left| \alpha \, \frac{\partial S}{\partial u} - \frac{\partial L}{\partial u} \right|^2}{\left(\left| \alpha \, \frac{\partial S}{\partial u} \right| + \left| \frac{\partial L}{\partial u} \right| \right)^2} < 10^{-5} \qquad \text{with} \qquad \begin{aligned} \frac{\partial S}{\partial u} &= -U^T \, \mathrm{diag}\{A\} \, U \, u \\ \frac{\partial L}{\partial u} &= U^T \, \mathrm{diag}\{A\} \, U \, g. \end{aligned} \tag{4.22}$$

Once the convergence is reached, the solution vector u can be substituted back in equation (4.17) in order to obtain the most probable spectral function $\hat{A}_\alpha(\omega)$ for given α.

The numerical effort can be further reduced, if the matrix $(\partial g / \partial u)$ in the Newton search (4.21) is diagonalized. The addressed procedure involves quite a number of new matrices and a subspace division, because some of the required eigenvalues can become very small or even negative. Since this section should only be an outline of the Bryan algorithm, the interested reader is referred to the detailed description in [101].

After the solution $\hat{A}_\alpha(\omega)$ was obtained, the probability $P[\alpha|Dm]$ and the covariance matrix $-\nabla\nabla Q$ are still to be calculated. Applying a Gaussian approximation to (4.11), the probability can be rewritten in terms of the eigenvectors λ_i of $\Lambda_{ij} = \sqrt{A_i}\frac{\partial^2 L}{\partial A_i \partial A_j}\sqrt{A_j}|_{A=\hat{A}_\alpha}$ (see [17] for details)

$$P[\alpha|Dm] = P[\alpha|m] \ \exp\left\{\frac{1}{2}\sum_i \log\left(\frac{\alpha}{\alpha+\lambda_i}\right) + \alpha S - L\right\}. \tag{4.23}$$

The first factor can be chosen as $P[\alpha|m] \sim 1/\alpha$, which is absorbed in the integration measure $d\alpha \to d\log(\alpha)$. The probability must be correctly normalized to $\int P[\alpha|Dm] \, d\alpha = 1$, alternatively the final spectral function in equation (4.10) can be divided by $\int P[\alpha|Dm] \, d\alpha$, which yields in the discretized version

$$\bar{A}(\omega) = \frac{\sum_{\alpha_{max}}^{\alpha_{min}} \hat{A}_\alpha(\omega) \ \exp\left\{\frac{1}{2}\sum_i \log\left(\frac{\alpha}{\alpha+\lambda_i}\right) + \alpha S - L\right\} \Delta\log(\alpha)}{\sum_{\alpha_{max}}^{\alpha_{min}} \ \exp\left\{\frac{1}{2}\sum_i \log\left(\frac{\alpha}{\alpha+\lambda_i}\right) + \alpha S - L\right\} \Delta\log(\alpha)}. \tag{4.24}$$

Numerically it is convenient to start at α_{max} with $P[\alpha|Dm] < 10^{-8} P_{max}[\alpha|Dm]$. Then the contributions $\hat{A}_\alpha(\omega) \ P[\alpha|Dm]$ for each α are summed up in steps of $\Delta\log(\alpha)$, until a similar probability as the initial one is reached for α_{min} at the other side of the sharply peaked distribution (see figure 4.1).

For the calculation of the error on the spectral function in a certain ω-range, the covariance matrix in the Gaussian approximation is needed. It can be calculated in terms of the singular space quantities [101]

$$-(\nabla\nabla Q)^{-1} = \text{diag}\{A\} \ U \ Y \ \text{diag}\left\{\frac{1}{\alpha+\lambda}\right\} \ Y^T \ U^T \ \text{diag}\{A\}, \tag{4.25}$$

where the matrix Y can be derived from the diagonalized matrix $(\partial g/\partial u)$ in the Newton search. Inserting equation (4.25) in (4.15) yields finally the desired spectral function with error bars in specific regions.

4.4 Dependence on Input Parameters

After having implemented the MEM code described in the last section it is important to examine the influence of the input parameters as well as the statistics on the resulting spectral function. Such a test was performed with a data set for the pion correlator which is described in the beginning of section 4.5. First of all a large number of almost independent gauge field configurations is needed to obtain a reliable data set for the observable. The influence of the number of configurations is displayed in figure 4.2(a) for the ground state peak of the pion at zero temperature. It can easily be seen, that an insufficient number of configurations results in a flattening and broadening of the peak. Furthermore the position of the peak is shifted slightly towards smaller masses. This can be best observed in comparison with the black line, which indicates the pion mass obtained with a conventional two-exponential fit. The masses extracted from the spectral

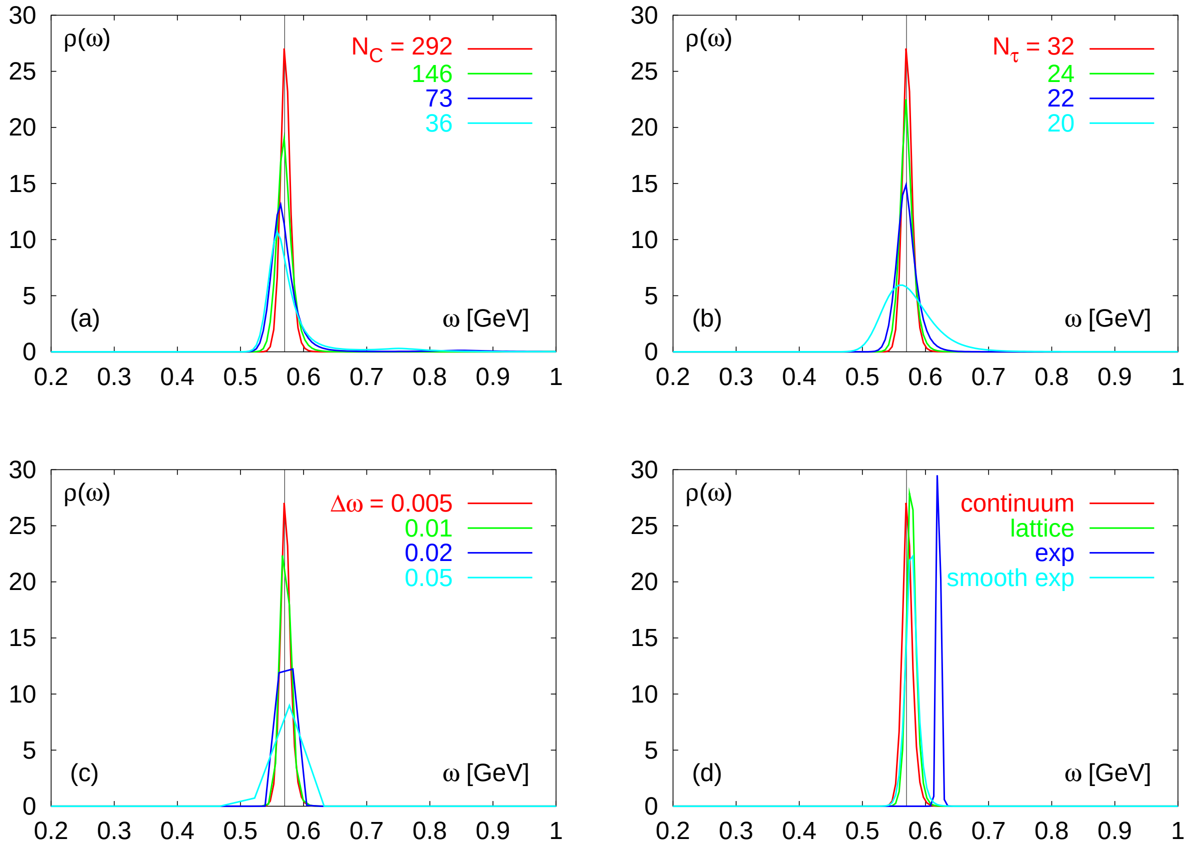

Figure 4.2: Influence of the input parameters on the spectral function, (a) number of configurations N_C, (b) number of time slices N_τ, (c) discretization interval $\Delta\omega$, (d) kernel definition, displayed for the enlarged ground state region for the zero temperature pion with $\kappa = 0.146$; the black line indicates the position obtained from the 2-exponential fit.

functions with 292 and 146 configurations clearly agree with the simple fit result, whereas both spectral functions with less statistic would lead to a somewhat smaller value.

A second parameter which is restricted by the limited available computer time is the lattice volume. It is certainly desirable to perform lattice calculations on large lattices, but in practice most of the calculations were carried out on relatively small lattices. The volume dependence on the correlation and spectral functions will be further explored in section 4.7. Here I only want to direct the attention to the influence of the temporal extent of the lattice. Since no data sets with various number of time slices were available, the situation could be simulated in leaving out data points for larger time separations in the MEM analysis. This would correspond to data with the same lattice spacing, but a smaller number of time slices. The resulting ground state peaks for the pion can be found in figure 4.2(b). The position of the peak is only shifted for the smallest N_τ. In general the peak broadens and is reduced in its height for decreasing number of time slices. This effect is especially visible for $N_\tau = 20$.

The MEM analysis works with a spectral function determined at discrete frequencies. Since the computer time rises exponentially with the number of points N_ω in the ω-range explored, it is necessary to compromise between a fast computation and a good resolution. This is of particular importance for the exact analysis of peak positions. Keeping the maximal frequency on the lattice fixed at about π/a, the frequency range was divided into 70-700 discrete points. The ground state peak of the pion can easily be resolved for the two smallest frequency separations in figure 4.2(c). For larger $\Delta\omega$ the correct determination of the peak position becomes increasingly complicated and would result in an overestimated error on the particle mass. Therefore it is advisable to use several hundred points for the discretization of the frequency range.

Another important aspect of the MEM analysis is the choice of the integral kernel in equation (4.4). At zero temperature, respectively $N_\tau \to \infty$, the periodic continuum kernel reduces to the simple exponential kernel $\exp(-\tau\omega)$. Note that this kernel does not take into account the periodicity on a lattice with finite N_τ. The peak of the spectral function obtained with the continuum kernel is well positioned on the black line of the conventional fit in figure 4.2(d), whereas the one from the exponential kernel is clearly shifted to the right. The correct peak position for this kernel could only be obtained with the smoothing technique for the covariance matrix (see section 2.5 for details). A further possibility to choose the integral kernel arises from the special lattice kernel, which should compensate the effects of the finite lattice spacing. The discrete frequencies for a boson propagator on the lattice $\omega_{n,lat} = 2\sin(n\pi/N_\tau)$ can be inserted in formula (4.4)

$$D(\tau) = \int_0^\infty T \sum_n \frac{2\omega}{\omega_{n,lat}^2 + \omega^2}\, e^{-i\omega_n \tau}\, A(\omega)\, d\omega. \tag{4.26}$$

Then the lattice kernel is determined through

$$K^{lat}(\tau,\omega) = 2\omega/N_\tau \sum_{n=0}^{N_\tau - 1} \frac{\exp(-i\; 2n\pi\tau/N_\tau)}{4\, \sin^2(n\pi/N_\tau) + \omega^2}. \tag{4.27}$$

Using the lattice kernel in the MEM procedure results in a spectral function very similar to the one obtained with the continuum kernel, which can be observed in figure 4.2(d).

The effect of the lattice kernel is more important for the finite temperature spectral functions, where the continuum part gets more dominant compared to the ground state peak. Short distance distortions in the correlation function due to the lattice discretization thus are enhanced. Since the number of time slices is usually smaller at high temperature $T = (N_\tau a)^{-1}$, the height of the peaks is reduced additionally in analogy to figure 4.2(b). At finite temperature it is convenient to express the spectral functions in units of $\omega' = \omega/T$. Accordingly the correlation functions should be divided by a factor T^3. The influence of the different integral kernels is shown in figure 4.3(a/b). The spectral function of the pion at 0.6 T_c is a bit smoother for the lattice kernel, in particular the broad continuum bump has flattened out, whereas the ground state peak nearly remains the same. The effect of the lattice kernel is even more pronounced for the spectral function of a free meson. In this case all unphysical bumps and hills disappear and the well-known tanh-like spectral shape is obtained. Further details about the free spectral functions are described in section 4.7.

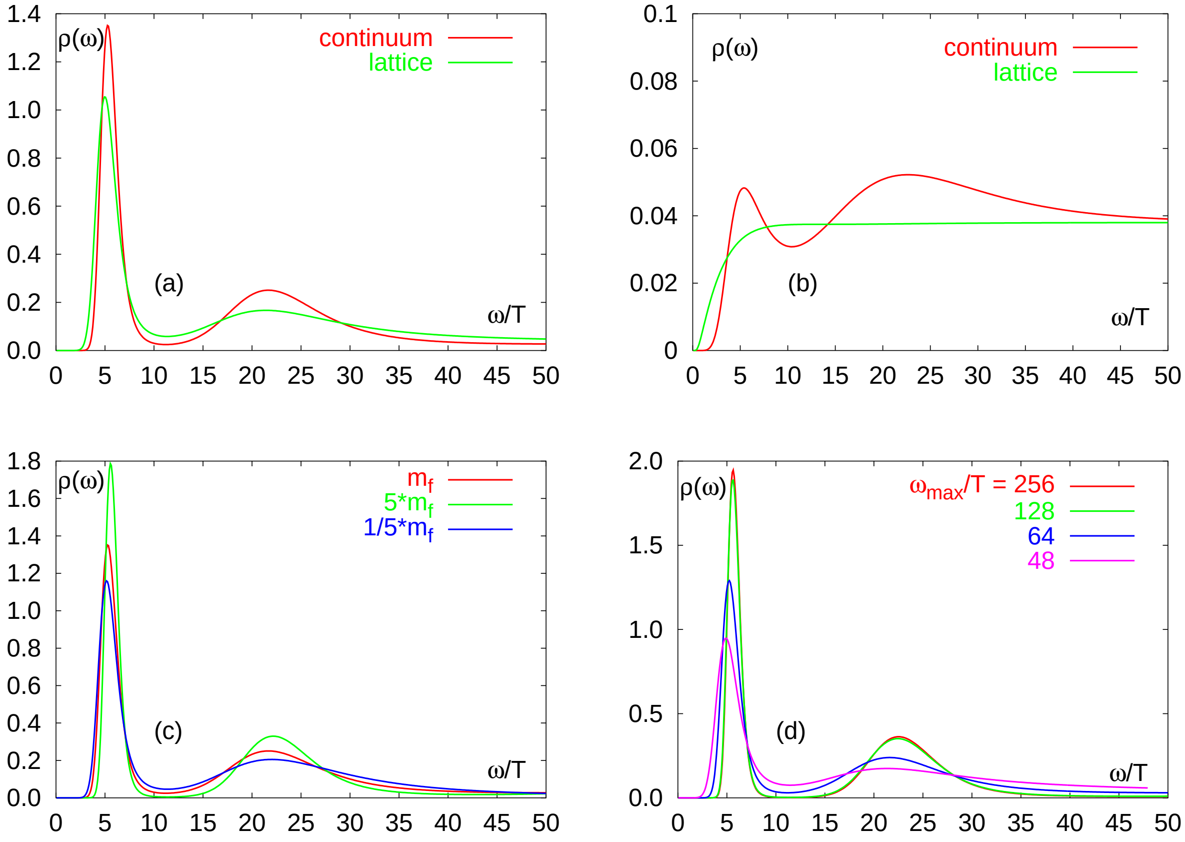

Figure 4.3: Influence of the input parameters on the spectral function at finite temperature, kernel dependence for the pion at 0.6 Tc (a) and for the free scalar meson (b); dependence on the default model parameter $m_0 = f m_f$ (c) and $\omega_{max} = N_\omega \; \Delta\omega$ (d).

The last two parameters which influence the finite temperature spectral functions are the factor m_0 of the default model and the maximal frequency ω_{max}. Since the default model is assumed to have the functional form $m(\omega) = m_0 \omega^2$, which is motivated by perturbative calculations [18], the only freedom is contained in the variation of m_0. Therefore the influence of a factor f on $m_0 = f m_f$ with $1/5 \leq f \leq 5$ is explored in figure 4.3(c). This factor alters only the height of the peaks, but not their position. The correct normalization constant is $m_f = 3/(8\pi^2)$ for the (pseudo-)scalar and $m_f = 1/(4\pi^2)$ for the (axial-)vector meson [92, 102], which yields the free correlation function for a massless meson with $D(N_\tau/2) \equiv 1$. Multiplying the data and the default model with the same factor only results in the enhancement of the amplitude of the spectral function by this factor. Furthermore the relevant α-range is shifted towards smaller values for a factor $f > 1$, which could sometimes be advantageous in the numerical calculation.

In figure 4.3(d) it is shown that the spectral functions for smaller ω_{max} exhibit a behavior similar to that obtained with a small m_0. Moreover, the peaks are shifted towards lower frequencies. For values $\omega_{max}/T \simeq 128$ or larger the spectral functions display only neglectable differences. Such a value of ω_{max}/T roughly corresponds to the maximal available momentum on the lattice. In general a reasonably large ω-range should be chosen to obtain reliable spectral functions.

After studying the influence of the various input parameters on the final spectral function, one can proceed to the systematic analysis of correlation functions with the Maximum Entropy Method. The next three sections deal with a detailed analysis of meson and diquark spectral functions at zero temperature as well as meson spectral functions at finite temperature.

4.5 Meson Spectral Functions

Previously produced data samples in quenched QCD with Wilson fermions could be used to analyze meson correlation functions at zero temperature. The gauge field configurations have been generated on a lattice of size $16^3 \times 32$ with a tree-level Symanzik improved action at a gauge coupling $\beta = 6/g^2 = 4.1$. The lattice cut-off $a^{-1} \sim 1.1$ GeV was determined by means of the string tension [4]. In total 73 configurations were fixed to Landau gauge (see sec. 2.4), which opens the possibility to calculate correlation functions for the color carrying diquark operators. For the fermion sector the Sheikholeslami-Wohlert action with a tree-level clover coefficient [46] was used. The fermion matrix has been inverted for eight different quark mass values and with source vectors at four different lattice sites. Therefore the data sample is based on 292 quark propagators, which provides sufficient statistics for the Maximum Entropy analysis. The meson masses obtained from conventional two-exponential fits were already published in [74, 75].

The meson correlation functions at zero temperature (see figure 4.4(a)) show a clean exponential decay, therefore a sharp δ-like peak in the spectral function is expected. This is indeed the case for the pseudo-scalar meson spectral function displayed in figure 4.4(b). A much stronger influence of excited states can be observed for the vector meson, which is already visible in the curvature of the correlation function at small time separations.

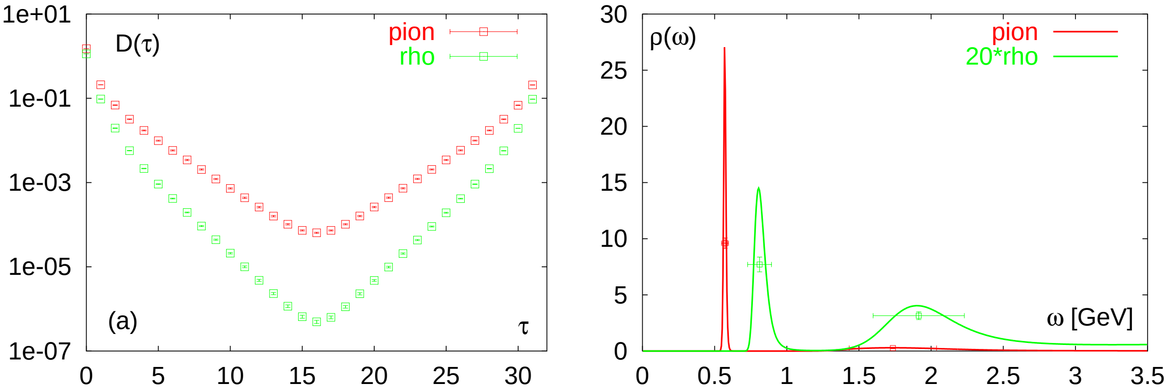

Figure 4.4: Correlation functions (left) and corresponding spectral functions (right) for the zero temperature pseudo-scalar and vector meson at $\kappa = 0.146$

In the spectral function this is reflected by the continuum-like structure at high energies. Recently it has been proposed [98] that this broad peak at high energies (about 1.7 GeV (2 GeV) for the pion (rho)) can be interpreted as bound state of two fermion doublers of the Wilson quark action. Therefore this state may be a lattice artifact with a divergent mass in the continuum limit. Since the data set at zero temperature was only generated for one lattice spacing, this assumption could not be verified in the framework of the present analysis. The error bars shown in figure 4.4 need a little explanation. Each horizontal bar marks the ω-range within which the average of the spectral function was taken and its height reflects this average value. The vertical error bar then indicates the variance of the average spectral function in this range. Mean and variance were calculated by applying equation (4.15).

Another important point is to understand the peak width and height of the reconstructed spectral functions, since the area under the peaks is related to the decay constants of the respective particle [98]. The simulations were carried out in the quenched approximation, which only admits interactions of the fermions with the gluonic background fields. In this case the expected width of the ground state peak would be zero in the pseudo-scalar channel and very small for the vector meson [98], but this assumption holds true only for an infinite number of gauge field configurations and an infinite temporal extent of the lattice. In figure 4.2(a/b) it was already shown that an insufficient number of configurations and a limitation on the number of time slices results in a flattening and broadening of the peaks. Nevertheless the width of the pion ground state peak is much smaller than the one of the rho meson (see fig. 4.4). The statistical noise has more influence for the vector meson operator, therefore a larger number of configurations is needed to obtain a similar accuracy in the rho meson mass. This effect is also visible in the larger error bars for the rho masses obtained in two-exponential fits.

Figure 4.5 displays a whole set of pseudo-scalar and vector meson spectral functions at several quark mass values. They were obtained with the continuum kernel in a frequency range up to $\omega_{max}a = 3.5$ with separations of $\Delta\omega a = 0.01$. The pseudo-scalar spectral functions show very sharp pion ground state peaks and only small contributions of excited

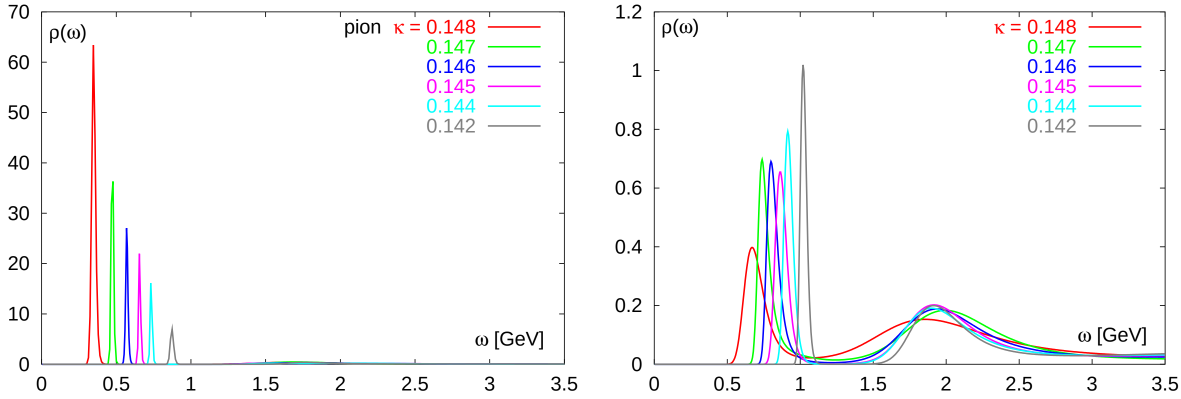

Figure 4.5: Spectral functions for the pseudo-scalar (left) and the vector meson (right) at different κ-values.

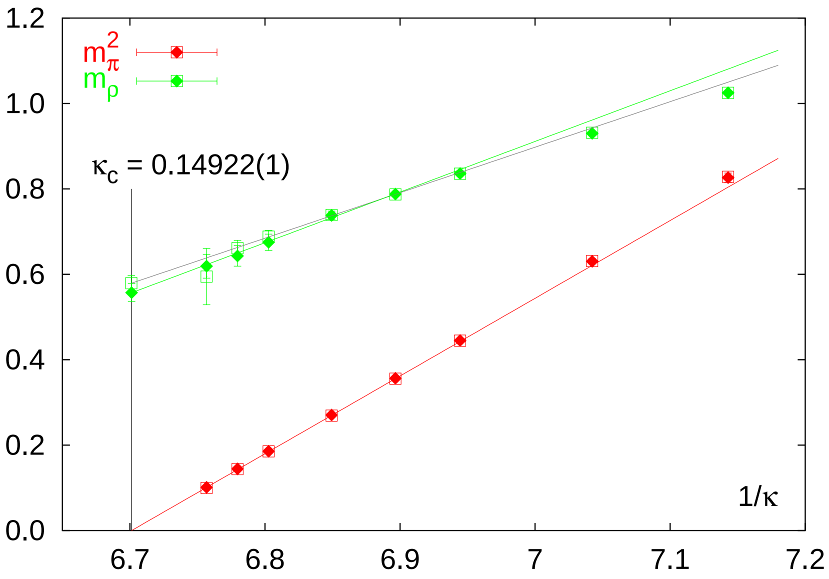

Figure 4.6: Comparison of the MEM results (diamonds) with conventional two-exponential fit results (squares).

states. The peaks for smaller quark masses are more pronounced in this representation of the spectral function, but they are of approximately equal height in the full spectral function $A(\omega) = \rho(\omega)\omega^2$.

On the other hand, the broadening and drop of the low mass contributions seen for the lightest quark masses in the vector spectral function can be addressed to insufficient statistics for this correlator. This is also apparent from conventional exponential fits, which in these cases lead to large errors on the lightest vector meson masses in figure 4.6. In general the pion and rho meson masses obtained with MEM are in very good agreement with the results from two-exponential fits. For the lightest rho meson mass even an improvement could be achieved. Instead of a drop of the mass with a large error bar a much more reasonable point with a smaller error could be obtained with MEM.

An error on the peak position of the spectral functions can be obtained in different ways. One possibility is to employ a fit with a Gaussian form to extract the position and the variance of the peak, but this procedure usually overestimates the error on the particle masses. For the results quoted in this thesis a Jackknife analysis with six blocks was utilized. This method includes the MEM analysis for the whole data set as well as for six reduced data sets. After the determination of the peak position on each of the reconstructed spectral functions, the Jackknife error could easily be obtained as described in section 2.5. A linear extrapolation in $1/\kappa$ leads to a vanishing pion mass at κ_c=0.14922(1), which perfectly coincides with the value 0.14923(2) obtained from a conventional exponential fit. Extrapolating the rho meson mass for the five lowest quark masses to the chiral limit, one obtains m_ρ(MEM)=0.56(2) in lattice units, which is compatible with m_ρ(exp-fit)=0.58(2). The values for each quark mass can be found in table B.6 of appendix B.

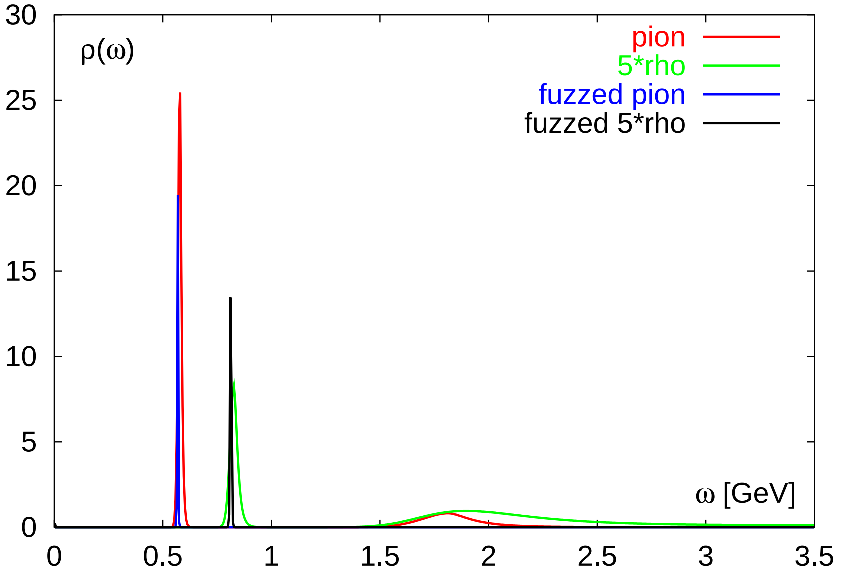

Figure 4.7: Influence of the fuzzing technique on the spectral functions

Concluding this section about meson spectral functions at zero temperature the influence of the fuzzing technique (see section 3.5) on the contributions of excited states to the spectral functions is investigated. In this case a smaller data set of 57 configurations on a $16^3 \times 30$ lattice was available. All other parameters remain the same as described at the beginning of this section.

The fuzzing technique was applied for spatially extended operators with a radius R=0.7 fm. In figure 4.7 the pseudo-scalar and vector meson spectral functions with and without fuzzing can be examined. After the fuzzing procedure the height of the ground state peaks remains almost the same, whereas their width is considerably reduced. Moreover the contributions of excited states at higher energies vanish. As a consequence only the sharp ground state peaks are left in the spectral functions. They thus uncover unambiguously that the application of the fuzzing technique eliminates the excited states almost completely.

4.6 Diquark Spectral Functions

This section deals with diquark correlation and spectral functions at zero temperature obtained from the 292 quark propagators mentioned at the beginning of the previous section. The correlation functions were calculated for four different diquark operators, namely the lighter color anti-triplet states $\bar{3}0\bar{3}$ and $61\bar{3}$ as well as the color sextet states $\bar{3}16$ and 606. These abbreviations correspond to the (flavor, spin, color)-representation as already introduced in section 3.1.

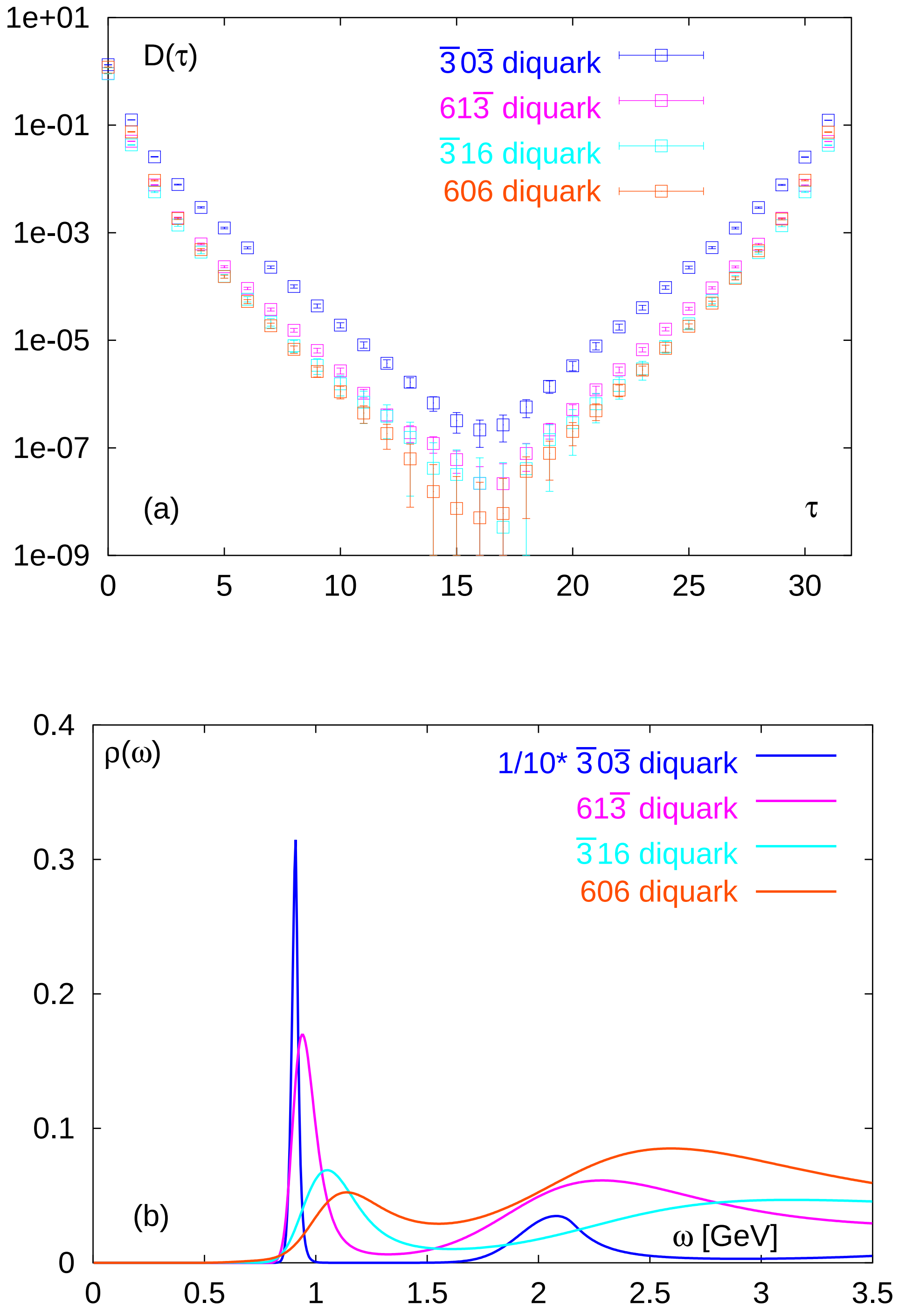

Figure 4.8: Correlation functions (top) and corresponding spectral functions (bottom) for the zero temperature diquarks at $\kappa = 0.146$.

The diquark correlation functions obtained from this data set are shown in figure 4.8(a). It can clearly be observed that the $\bar{3}0\bar{3}$ diquark correlation function exhibits the characteristic exponential decay known from mesons. To a certain extent this is also the case for the $61\bar{3}$ diquark. The correlation functions of the color sextet diquarks are strongly influenced by higher excited states. Furthermore larger error bars are attached to the points, which already indicates the insufficient statistics for these noisy correlators.

The spectral functions for the color anti-triplet diquarks are similar to the ones for mesons (see figure 4.8(b)). In particular the $\bar{3}0\bar{3}$ diquark spectral function shows a pronounced ground state peak and is therefore reduced by a factor 10 in the plot. However, already in the case of the $61\bar{3}$ diquark the ground state peak broadens and becomes comparable in magnitude to the continuum structure found at higher energies. This broad continuum becomes even more dominant in the color sextet channels. Although it is unclear to a certain degree whether a bound state exists in these quantum number channels, this series of diquark states is an excellent example to study the possible variations from bound to probably unbound states in terms of the spectral functions.

Nevertheless the ground state peak position for all diquark states could be determined by a Jackknife error analysis at all quark masses. These results are summarized in table B.7 of appendix B. Note that the smoothing of the covariance matrix becomes increasingly important for the analysis of the color sextet spectral functions. This method was described in detail in section 2.5. Figure 4.9 visualizes the influence of the procedure on the spectral function of the 606 diquark. Since the number of configurations is insufficient for this noisy correlator, the covariance matrix has several too small eigenvalues. Using the full covariance matrix for the MEM analysis results in an unphysical state below the ground state peak. Moreover the ground state peak is shifted to higher frequencies. By retaining only the 5-6 largest eigenvalues, the unphysical peak can be eliminated or at least reduced.

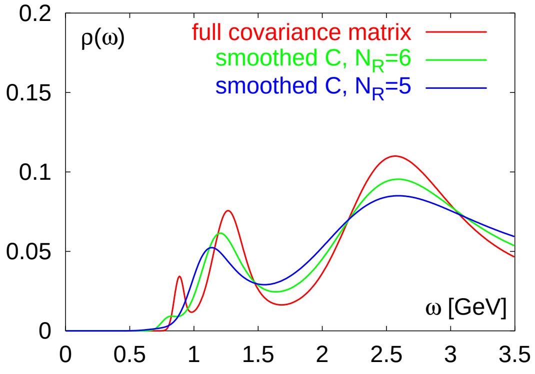

Figure 4.9: Influence of the covariance matrix smoothing procedure; N_R denotes the number of retained eigenvalues (see sec. 2.5).

Having obtained the diquark masses from a Jackknife analysis of the spectral functions, they can directly be compared with the ones obtained from conventional two-exponential fits. For the color anti-triplet diquarks this is displayed at the top of figure 4.10. The MEM values lie systematically a bit lower than the exponential fit results, but they clearly agree within their error bars. This leads to slightly lower masses in the chiral limit, extrapolated from the values at the five lightest quark masses. Table 4.1 can be consulted for the exact values.

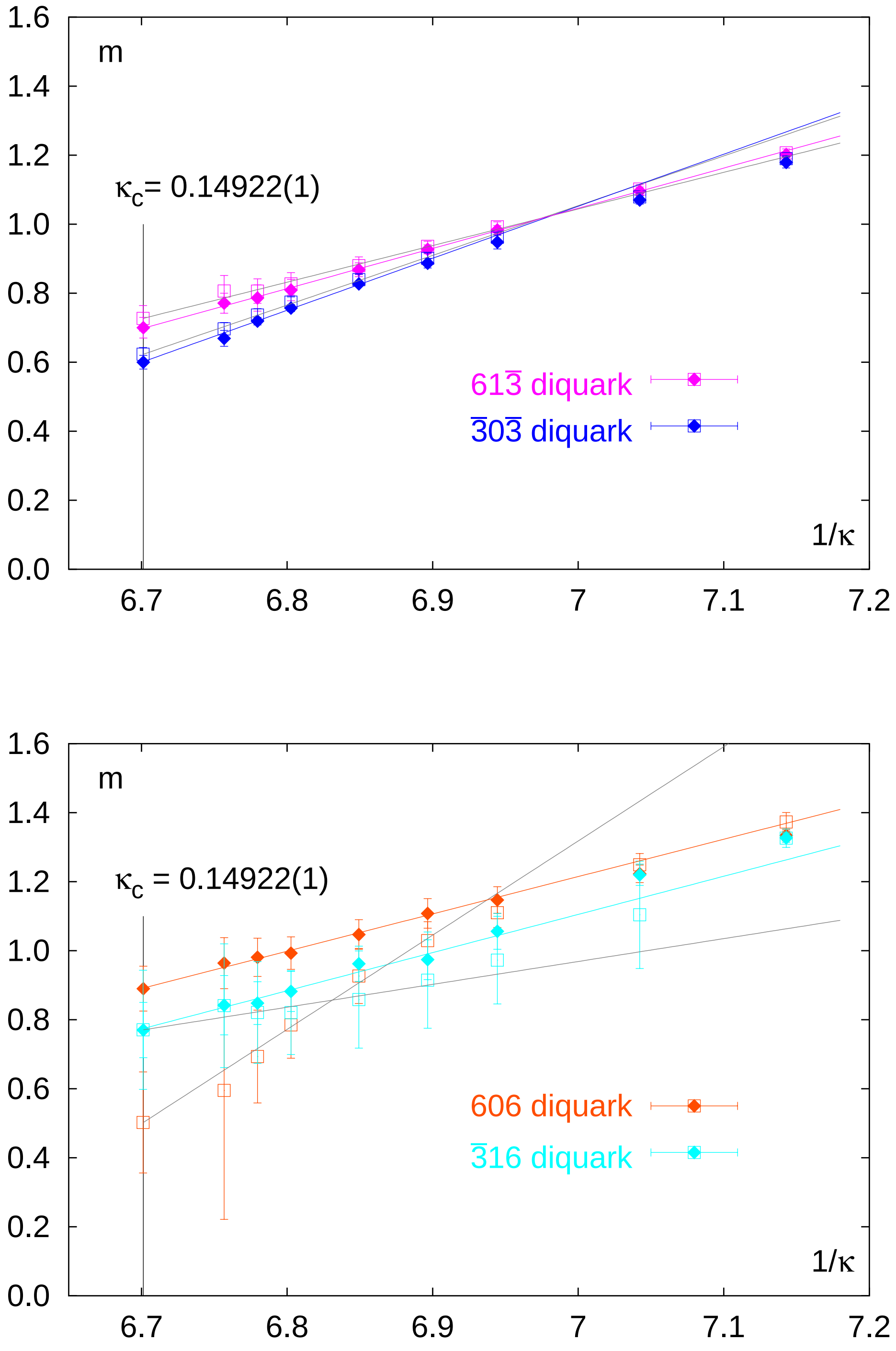

Figure 4.10: Comparison of the MEM results (diamonds) with two-exponential fits (boxes) for the color anti-triplet diquarks (top) and sextet diquarks (bottom).

Diquark state	$\bar{3}0\bar{3}$	$61\bar{3}$	$\bar{3}16$	606
$ma_{(FSC)}$: MEM result	0.60(2)	0.70(3)	0.77(8)	0.89(13)
$ma_{(FSC)}$: 2-exp. fit	0.62(2)	0.73(4)	0.77(17)	0.50(15)

Table 4.1: Comparison of diquark masses in the chiral limit.

The color anti-triplet as well as the sextet states have in common that their masses are close to each other at larger bare quark mass and split up at smaller quark masses due to the flavor-spin interaction. The q-q interaction is attractive (repulsive) for the color anti-triplet (sextet) diquark states (see table 3.1 or in detail [74, 75]). This behavior was covered in statistical noise of the correlators for the heavier sextet states and could not be resolved by exponential fits. The masses of the $\bar{3}16$ diquark state were only slightly underestimated but had large errors, whereas the exponential fit results for the 606 diquark were misled through the unphysical state visible in fig. 4.9. For the color sextet diquarks an enormous improvement could be achieved with the Maximum Entropy Method.

Extrapolating the masses to the chiral limit, the same value as in the exponential fit is obtained for the $\bar{3}16$ diquark, but with an error half as large as before. Note that this value has changed in comparison to the publication [103], where the influence of the covariance matrix smoothing had not yet been explored. The mass values of the 606 diquark now extrapolate to a considerably higher value in the chiral limit, which is in much better agreement with the strong repulsion between the two quarks expected from the flavor-spin q-q interaction in this channel. In general, one may question for all but the $\bar{3}0\bar{3}$ diquark state whether the leading peak in the spectral function at all corresponds to a bound state. The spectral function favors an interpretation in terms of a threshold followed by a broad continuum. This question could be resolved in a more detailed spectral analysis with higher statistics.

4.7 Thermal Spectral Functions

In the last two sections the spectral functions at zero temperature were analyzed and results on masses were compared to conventional two-exponential fits. This gave some insight into the parameter dependence of the maximum entropy analysis and has shown how the spectral functions vary with different content in the correlation function. It could be shown that the MEM analysis correctly detects bound states like the pion as well as the more unbound and continuum-like states in the color sextet diquark channel. Since this experience is very encouraging an application of the method at finite temperature could be ventured. In this case it is absolutely mandatory that MEM needs no previous assumptions about the spectral shape, because very little is known about thermal spectral functions so far.

4.7.1 Free Meson Spectral Functions in the Continuum

In the high temperature limit the meson correlation functions are expected to reflect the dynamics of freely propagating quark anti-quark pairs. This can be described to leading order by the free spectral function in the degenerate (pseudo-)scalar channel [104]

$$A(\omega)=\frac{N_c}{8\pi^2}\,\omega^2\tanh(\omega/4T). \tag{4.28}$$

As a first step it thus is important to test whether such a spectral shape can be reproduced on lattices with finite temporal extent. Using the continuum expression (see equation (4.4))

$$D(\tau)=\int_0^\infty\frac{\cosh(\omega(\tau-1/2T))}{\sinh(\omega/2T)}A(\omega)\,d\omega, \tag{4.29}$$

the free meson correlation function can be calculated for an arbitrary number of time slices N_τ. The prefactor $N_c/8\pi^2$ of the spectral function (4.28) ensures that the obtained correlation function is normalized to one at $\tau=1/2T$. This is shown in figure 4.11(a) for several number of time slices. Note that the correlation functions at finite temperature are displayed in units of T^3; the spectral functions are determined correspondingly in terms of ω/T.

For the purpose of constructing a suitable mock data set for the MEM analysis of free meson correlators, a Gaussian noise with the variance [99]

$$\sigma(\tau)=\begin{cases} b\,D(\tau)\,\tau & \text{for}\quad \tau=0,\dots,N_\tau/2\\ b\,D(\tau)\,(N_\tau-\tau) & \text{for}\quad \tau=N_\tau/2,\dots,N_\tau\end{cases} \tag{4.30}$$

was added to the exact data values obtained from equation (4.28) and 4.29). The prefactor b controls the noise level. In order to guarantee a compatible noise level for data sets with different temporal extent, the product $b\,N_\tau$ should be kept fixed.

The reconstructed spectral functions for different N_τ and noise level are combined in figure 4.11(b). All curves are in good agreement with the free spectral function, except the one with the largest noise level $b=0.1$. They were obtained with the continuum kernel and quite a large frequency range $\omega_{max}/T\simeq 10N_\tau$. The resulting spectral functions with smaller ω_{max}/T would have some bumps in addition to the free curve. For the spectral functions with $N_\tau=32$ it can clearly be observed that the decrease of the noise level from 0.1 to 0.005 results in a reduction of the difference between the reconstructed and the original free spectral function. Even with only $N_\tau=16$ points and comparable low noise level the spectral shape can be reconstructed almost perfectly. Sometimes it may be useful to combine data sets on smaller lattices in order to get additional temporal grid points by varying N_τ. This is illustrated in figure 4.11(b) for a combination of $N_\tau=10,12$ and 16, which also yields a convincing reconstruction of the free spectral function.

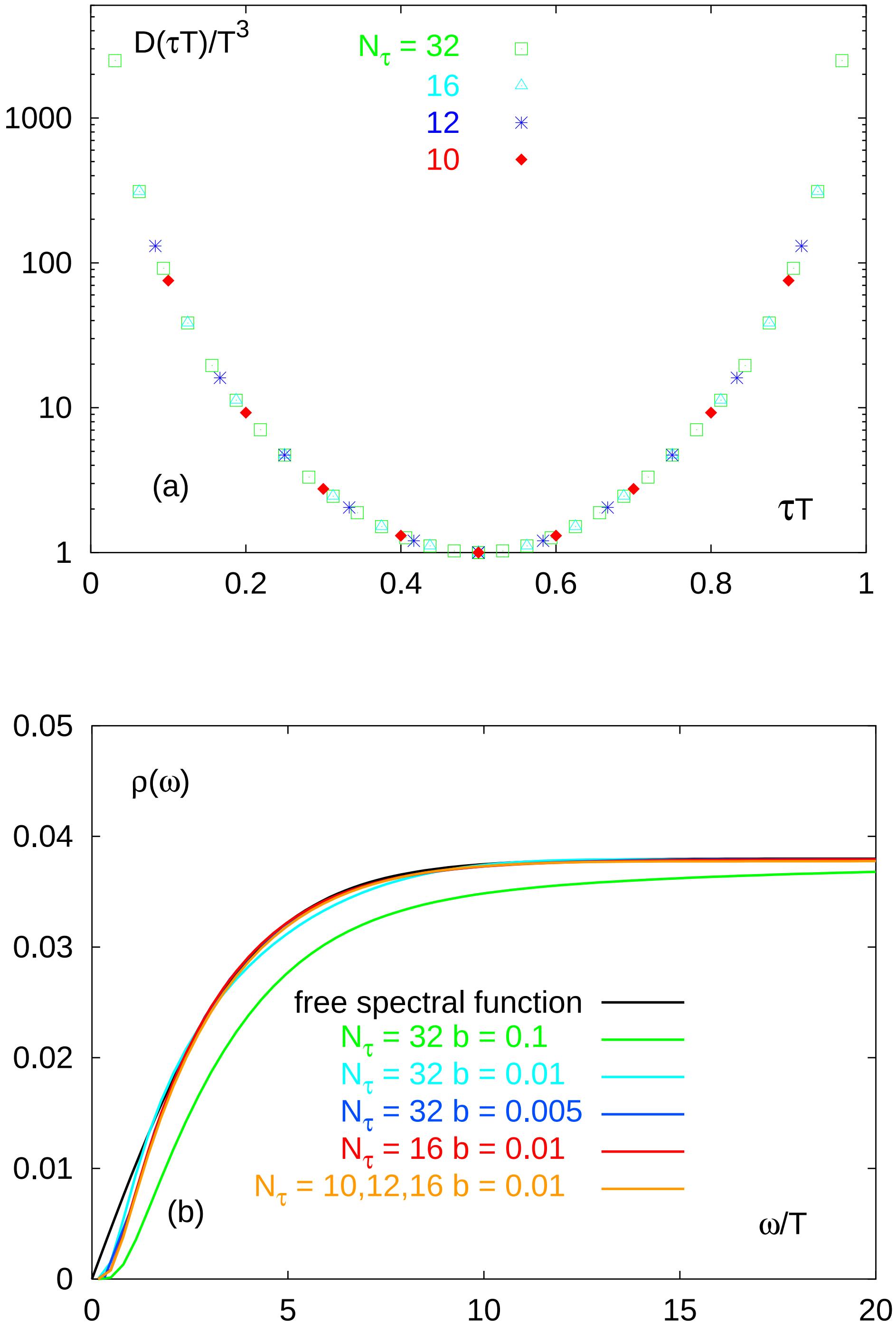

Figure 4.11: Discretized free thermal meson correlation function (top) and reconstructed spectral functions (bottom) with different noise level b.

4.7.2 Free Meson Spectral Functions on the Lattice

A step further towards the examination of thermal spectral functions is the calculation of free meson correlation functions on the lattice, which are restricted to the Euclidean time interval $[0, 1/T]$. In the high temperature limit the coupling g vanishes and the gauge fields approach unit matrices in color space. This allows the analytic calculation of the quark propagators (see eq. (2.13)) and thus the free meson correlators for any given lattice size. Alternatively lattice calculations may be performed with a unit configuration.

These free correlation functions on the lattice can be used to explore the finite volume and cut-off effects which are expected to modify the results obtained on small lattices. Figure 4.12(a) displays the free (pseudo-)scalar correlation functions for various spatial extents of the lattice. At equal spatial and temporal extension the curve is enhanced and flattened in the middle. This leads to modifications at low frequencies in the corresponding spectral function. It can be observed that a ratio of $N_\sigma/N_\tau = 2 - 4$ is needed to eliminate the finite volume effects almost completely.

The influence of the finite lattice cut-off is illustrated in figure 4.12(b) for several lattice sizes. The largest deviations from the continuum free curve are visible for small Euclidean times, in particular for the first two points $\tau = 0, 1/N_\tau$. Unlike in the continuum limit the lattice correlation function is not divergent at $\tau = 0$ for $N_\tau < \infty$. The free meson correlation function on the $N_\tau = 16$ lattice was utilized at first in a MEM analysis with the continuum kernel. However, this attempt to reconstruct the spectral shape failed unexpectedly. Even leaving out the points at $\tau = 0$ and 1, which have the strongest cut-off effects, yields the curve with two bumps visible in figure 4.13. In this case the lattice kernel defined in equation (4.27) is a resource to reproduce the free spectral function correctly. Instead of the fairly large ω-range which is used for the continuum kernel, the maximal frequency is restricted to $\omega_{max}/T \simeq 4N_\tau$ for the lattice kernel, which corresponds to the maximal available momentum on the lattice. The spectral shape could be reproduced

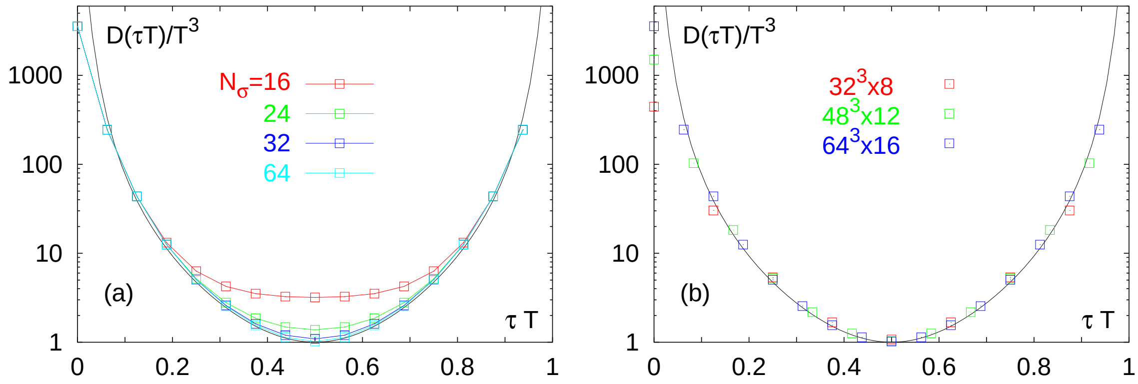

Figure 4.12: Finite volume effects with fixed N_τ=16 (left) and cut-off effects with fixed ratio N_σ/N_τ=4 (right) for the free meson correlation function on the lattice; the black line indicates the continuum free correlator.

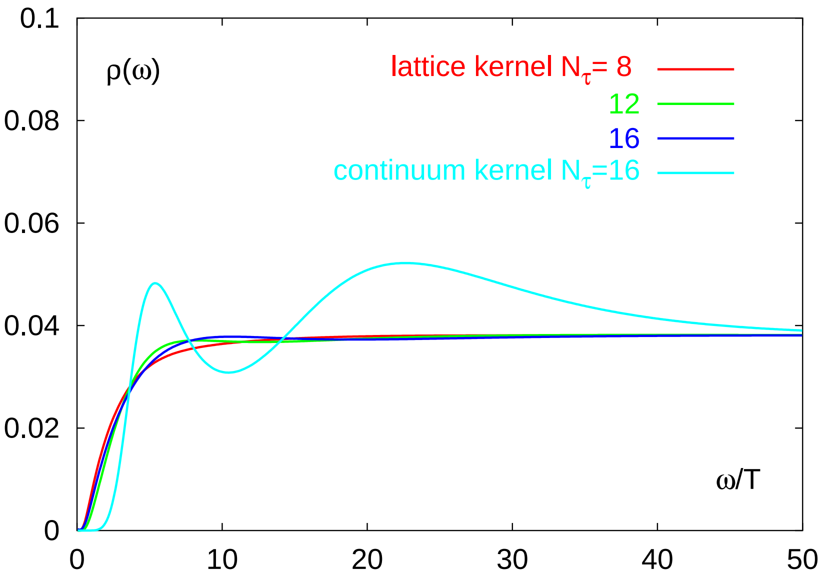

Figure 4.13: Reconstructed free lattice spectral functions with fixed noise level $b\ N_\tau = 0.16$.

well already with the correlators obtained on lattices with small temporal extent, N_τ =8 and 12. Apparently the cut-off effects are compensated efficiently in applying the lattice kernel.

At first sight an accurate reconstruction should also be possible for a combined data set, e.g. for N_τ =12 and 16. This attempt fails unfortunately since only the cut-off effects for a special N_τ-value can be absorbed in the choice of the lattice kernel and an appropriate choice of ω_{max}/T. It is obvious from figure 4.12(b) that correlators with evidently differing points at the same time separation cannot be represented by an unique spectral function. For the combined data set analyzed with the continuum kernel (fig. 4.11) this was no hindrance, since all correlators with different N_τ lay on a single smooth curve.

Considering the success of the fuzzing technique for an optimized projection onto the ground state at zero temperature (see figure 4.7), one might be tempted to use this method also at finite temperature, where the peaks are less pronounced compared to the continuum contribution. However, the entire concept of fuzzing has to fail when a single state is not well separated from higher excited states. The situation will naturally be even worse when only a continuum exists. In the case $T > T_c$ one can no longer be sure to project on an actual ground state, since even the fuzzing of the free meson correlation function leads to sharp peaks instead of the broad continuum. This is illustrated in figure 4.14 for different fuzzing radii R. The fuzzing causes the reduced curvature of the correlator at small time separations, which is correspondingly translated into the definitely unphysical peaks in the spectral function. Therefore it is mandatory for $T > T_c$ to use the unmodified point-point correlator in the MEM analysis to preserve the full information about ground and excited states as well as the continuum contribution.

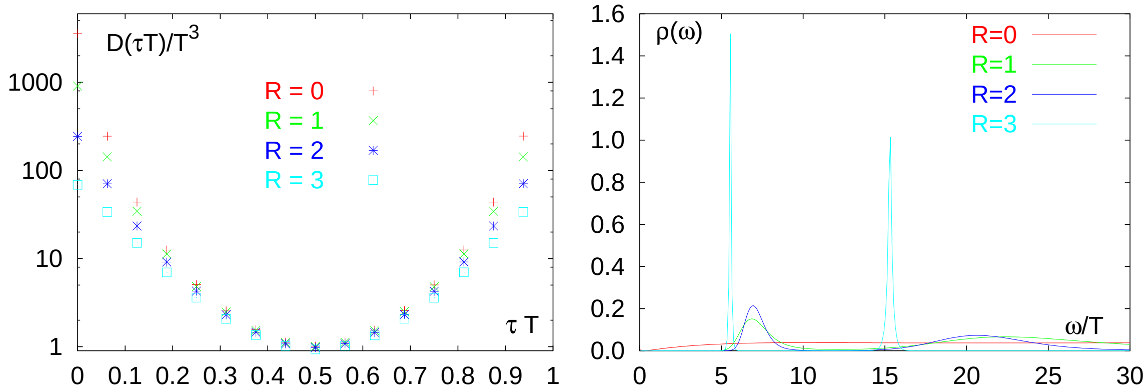

Figure 4.14: Fuzzing of the free spectral function

4.7.3 Meson Spectral Functions at Finite Temperature

Having tested the Maximum Entropy Method with continuum and lattice free meson correlation functions, we can proceed to the analysis of data sets from lattice simulations at finite temperature. Instead of using anisotropic lattices, which involves the precise calibration of the anisotropy parameters [16], we decided to perform simulations on fairly large isotropic lattices in quenched QCD. As shown before for the free meson correlation function on the lattice, already data sets with temporal extents $N_\tau = 12 \ldots 16$ seem sufficient to obtain reliable spectral functions. Table 4.2 summarizes the parameters used for the simulations below the critical temperature, performed on the APE machines in Bielefeld, and those employed above T_c within our project [105] on the Cray T3E in Jülich.

T/T_c	β	a^{-1}[GeV]	$N_\sigma^3 \times N_\tau$	N_C	κ-values	κ_c-value
0.4400	6.000	1.901	$24^3 \times 16$	60	0.1324 0.1332 0.1342 0.1348	0.13520
0.5625	6.136	2.430	$16^3 \times 16$	240	0.1346 0.1354	0.13571
			$24^3 \times 16$	60	0.1330 0.1340 0.1346 0.1354	
			$32^3 \times 16$	30	0.1330 0.1340 0.1346 0.1354	
0.9357	6.499	4.042	$16^3 \times 16$	40	0.1345	0.13558
			$24^3 \times 16$	120	0.1330 0.1340 0.1346 0.1354	
			$32^3 \times 16$	60	0.1330 0.1340 0.1346 0.1354	
1.5000	6.640	4.860	$48^3 \times 12$	25	0.13536	0.13536
	6.872	6.480	$64^3 \times 16$	40	0.13495	0.13495
3.0000	7.192	9.720	$48^3 \times 12$	40	0.13440	0.13437
	7.457	12.96	$64^3 \times 16$	40	0.13390	0.13396

Table 4.2: Summary of simulation parameters, T/T_c and a^{-1} are determined from the string tension on lattices with N_τ=8, 12 [4], κ_c-values interpolated from [47].

The gauge field configurations are separated by 500 sweeps of 5 overrelaxation and one heatbath step each. They were generated with the standard plaquette action, which allows us to apply the improved Clover fermion action with non-perturbatively determined clover coefficients (see sec. 2.1.2). Temporal and spatial meson correlators were calculated for up to four quark mass values below T_c and at almost zero quark mass (at estimated $\kappa_c(T = 0)$) above the critical temperature. The Coulomb gauge was fixed on the configurations above T_c in applying the Los Alamos algorithm combined with the overrelaxation method (see sec. 2.4 for details). This opened the possibility to calculate gauge-variant quark and gluon correlators.

A temperature of 1.5 T_c is reachable in heavy ion collisions, whereas the larger temperature of 3 T_c was chosen to allow a comparison with previous results from HTL-resummed perturbation theory [91]. Furthermore the results in this high temperature region can be compared to the free meson correlation and spectral functions discussed above. The simulations below the critical temperature were performed in order to analyze the changes in meson spectral functions in the whole range between the well known zero temperature case and the deconfining phase transition as well as to study finite volume and cut-off effects.

Mesons at 0.4 T_c in comparison with $T = 0$

Having explored the zero temperature correlators and spectral functions in the sections 4.5 and 4.6, the results can be compared to the ones at 0.4 T_c well below the phase transition. The spectral functions obtained for the pseudo-scalar, scalar and vector meson are displayed in figure 4.15 for several values of the bare quark mass. The behavior of the pseudo-scalar and vector meson spectral functions is qualitatively the same as observed for zero temperature (fig. 4.5). In general the height of the ground state peaks is reduced, their width is increased and the errors on the peaks are enlarged due to the limited statistics and the cut-off effects, since the number of configurations is only a fifth and the number of time slices $N_\tau = 16$ is halved in comparison to the $T = 0$ simulation. These effects were investigated in section 4.4 and are summarized in the figures 4.2(a) and (b). Nevertheless, a slight temperature effect could play a role in the changes of the spectral shape.

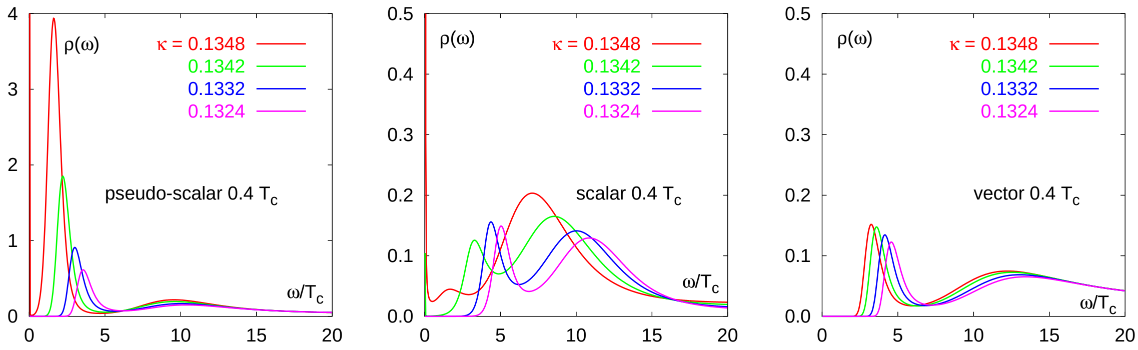

Figure 4.15: Meson spectral functions at 0.4 T_c for different κ-values.

The spectral functions of the scalar meson in the middle of figure 4.15 show a much less systematic behavior. The continuum structure dominates for all bare quark masses, similar to the color sextet diquark states which were investigated in section 4.6 (see e.g. figure 4.8). The spectral shape resembles the scalar spectral function at low temperature in a simulation of the $O(4)$ linear σ model [106]. Since only the connected flavor non-singlet parts of the scalar correlator were calculated in the lattice QCD simulation, the scalar channel corresponds to the δ meson introduced in section 1.2. The present MEM results suggest that no bound state exists in this channel at low temperatures, which needs to be confirmed by additional simulations with larger statistics.

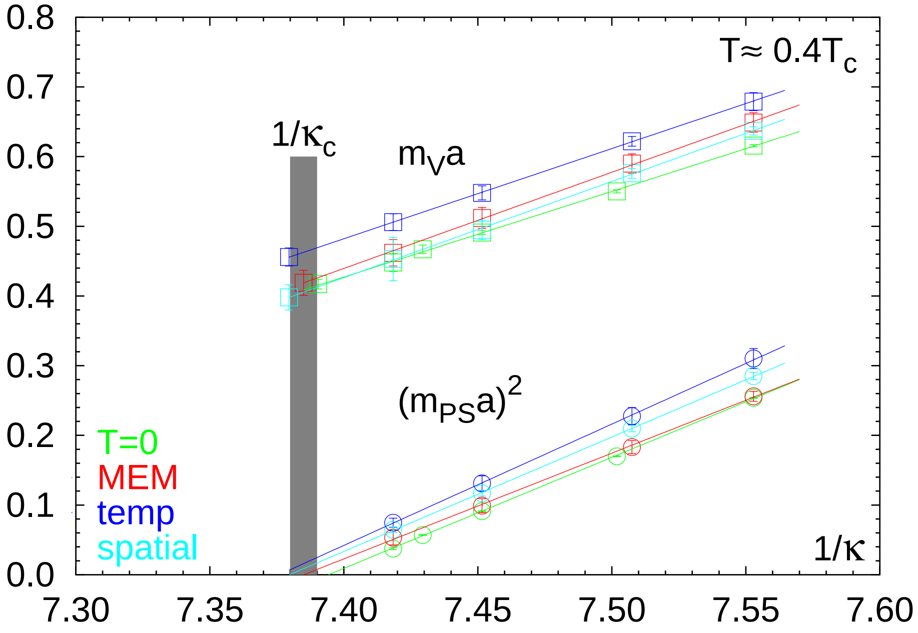

Figure 4.16: Meson masses at 0.4 T_c obtained with MEM and two-exponential fits, the band indicates the $1/\kappa_c$ range obtained for the different data sets.

The ground state peak positions of the pseudo-scalar and vector meson can be estimated in a Jackknife analysis of the spectral function. The MEM results for the meson masses at all temperatures below T_c are combined in table B.8 of the appendix. The extrapolation to the chiral limit is visualized in figure 4.16. The points indicated as $T = 0$ are adopted from a simulation of Göckeler et. al. [107] on a $24^3 \times 32$ lattice at $\beta = 6.0$ and similar κ-values. In addition to the MEM analysis conventional fits with one and two exponentials were performed for the temporal and the spatial correlator (see table B.9). For the pseudo-scalar meson mass a good agreement is obtained between the MEM and $T = 0$ results. The masses from the exponential fits of the spatial and temporal correlator lie slightly above the others, but extrapolate to similar values of the critical hopping parameter. The deviations are more pronounced for the vector meson. The exponential fit of the temporal correlator tends obviously to overestimated values due to the influence of continuum contributions. Since the MEM analysis allows a distinction between the pole and continuum contributions, much more reasonable values can be extracted from the same correlation function. In the chiral limit the extrapolated screening mass obtained from exponential fits in the more extended spatial direction as well as the $T = 0$ data point coincide with the MEM values within the error bars. This leads to the implication that the observed behavior at 0.4 T_c is not different from the one at T = 0.

Finite size effects below T_c

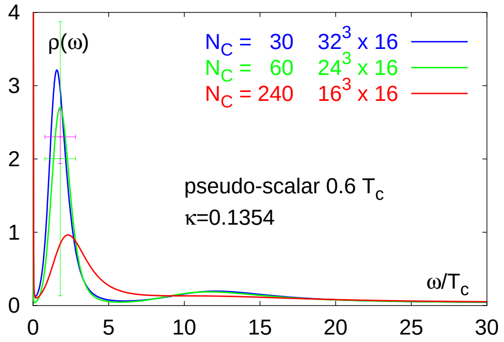

Figure 4.17: Finite size effects on the pseudo-scalar spectral function at 0.6 T_c.

At the somewhat higher temperature of 0.6 T_c data sets on three different lattice sizes open the possibility to study the finite size effects on the lattices investigated below T_c. Figure 4.17 shows the pseudo-scalar spectral functions at the smallest quark mass value $\kappa = 0.1354$ for a lattice size $(16-32)^3 \times 16$ with the indicated number of configurations. The ground state peak gets narrower and is increased by changing the spatial extent of the lattice from $N_\sigma = 16$ to 24. Only marginal differences are observed enlarging $N_\sigma = 24$ to 32, which could be affected by the limited statistics of only 30 configurations on the largest lattice. However, a shift of the ground state peaks towards lighter pion masses can be observed continuously by enlarging the lattice volumes. The indicated error bars belong to the spectral function of the $24^3 \times 16$ lattice data set. The larger one illustrates mean and variance calculated with relation (4.15) in the given ω-range, whereas the smaller one represents solely the statistical error, which is obtained in a Jackknife analysis of the average spectral function in this range. The divergence at very small frequencies can be traced back to insufficient statistics. In such a case the spectral function approaches $\omega \to 0$ not strictly proportional to ω^2, which leads to the unphysical behavior for the displayed spectral function $\rho(\omega) = A(\omega)/\omega^2$.

In the following the spectral functions below T_c refer to the $24^3 \times 16$ lattice. In general good agreement of the meson masses on lattices with N_σ=24 and 32 could be observed, but due to the limited statistics at N_σ=32 the errors are still at least twice as large as with N_σ=24. For example the resulting masses extracted in a Jackknife error analysis of the above mentioned spectral functions yield $m_{PS}^{24} a = 0.20(1)$ and $m_{PS}^{32} a = 0.18(3)$.

Pseudo-scalar and vector mesons at $0.4\,T_c < T < 3\,T_c$

The influence of increasing temperature on the spectral functions in the pseudo-scalar and vector channel can be illustrated more clearly in a combined plot such as figure 4.18. Below the critical temperature the spectral functions are shown at similar quark masses ($m_\pi \simeq 790$ MeV), while the ones above T_c have been obtained at $m_q \simeq 0$ which was checked with the relation (2.15). The spectral functions at 0.4 and 0.6 T_c remain very

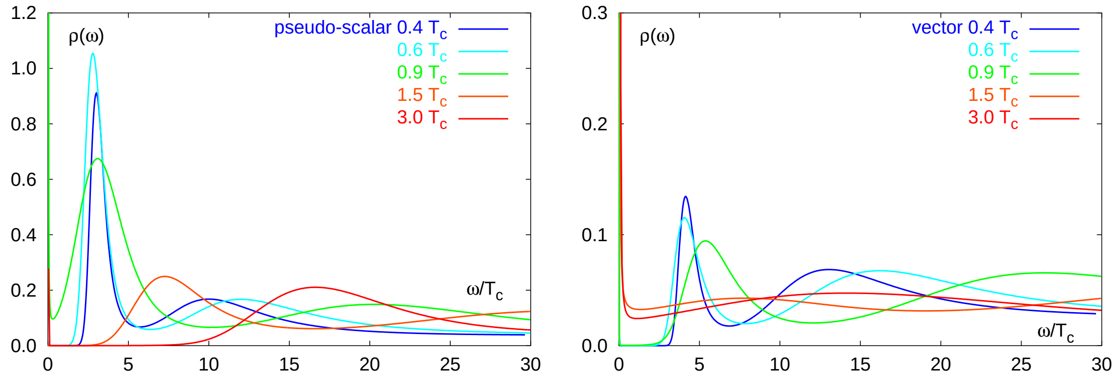

Figure 4.18: Spectral functions of the pseudo-scalar (left) and vector meson (right) for several temperatures.

similar in both channels, whereas a doubling of the width and a reduction in height of the ground state peak is visible at 0.9 T_c. Furthermore the peak of the vector meson is shifted towards larger frequency values. At present it is not clear whether this effect is an actual temperature induced modification of the spectral shape or only an artifact due to limited statistics, since the exponential fit of the spatial correlator yields an almost unchanged screening mass from 0.4 T_c up to 0.9 T_c (see table B.9).

Above the critical temperature the broad peak in the vector channel vanishes almost completely in favor of a continuum structure. However, better statistics is clearly desirable for the spectral functions at 0.9 - 3 T_c. In the pseudo-scalar channel the sharp ground state peak broadens considerably above T_c and is shifted towards larger energies. Nevertheless, deviations from the shape of the free spectral functions can be still observed, which will now be illustrated in more detail.

At high temperatures a scaling of the spectral function with the temperature is expected. Therefore it is more appropriate to investigate the changes of the spectral shape in units of the temperature rather than in physical units like T_c. The correlators and corresponding spectral functions in the pseudo-scalar and vector channel are illustrated in figure 4.19. Note that in the vector channel the sum of the contributions with all γ_k-matrices ($k = 1 \ldots 4$) is shown, which yields twice the (pseudo-)scalar correlator in the free case. At 1.5 and 3 T_c the γ_4-component of the correlation functions is simply a constant $\lesssim$ -1, which eliminates the divergence at $\omega/T = 0$ in the vector meson spectral function. Furthermore the (non-)perturbative renormalization factors for each β-value in the pseudo-scalar (vector) channel were taken into account [108, 109], which are summarized in table B.10. The correlation functions of the vector meson at 1.5 and 3 T_c lie almost on top of each other and agree very well with the free meson correlator indicated as solid black line. Slight deviations can be observed at intermediate time separations, which are also evident from the corresponding spectral functions at smaller frequencies. Such a modification of the spectral shape is expected in HTL-resummed perturbation theory [91]. In this case the spectral function in the vector channel is even linear divergent at low frequencies, which renders the temporal correlator infrared divergent.

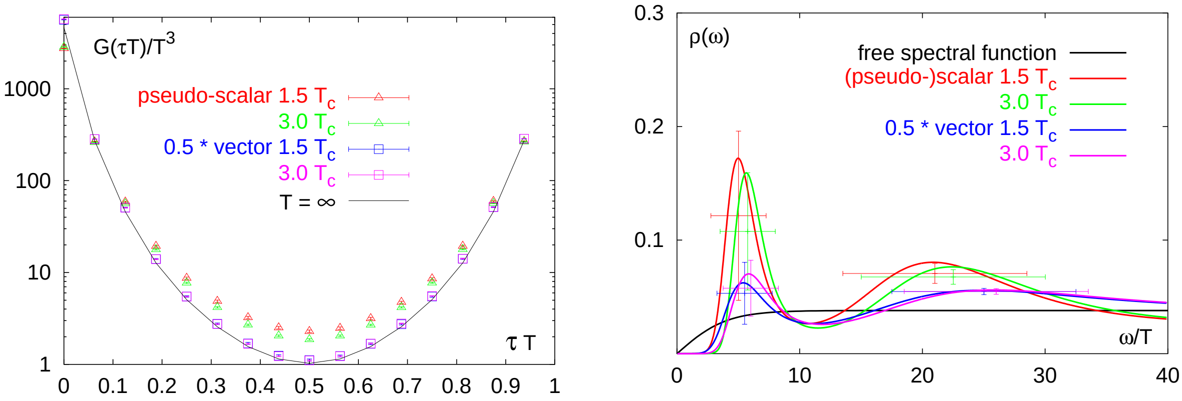

Figure 4.19: Meson correlation (left) and spectral functions (right) above T_c.

For the pseudo-scalar correlator a gradual approach towards the corresponding free meson correlation function can be observed by increasing the temperature from 1.5 to 3 T_c. Nevertheless quite large deviations from the free quark behavior still persist at the highest temperature investigated, which confirms the previous findings of Boyd et. al. [87]. This observation is even more emphasized considering the pseudo-scalar spectral functions in figure 4.19. In addition to a continuum-like structure a broad peak at lower frequencies is still evident. The position of this bump is quite sensitive to the number of retained eigenvalues in the covariance matrix smoothing procedure (see sec. 2.5). Higher statistics thus is needed to clarify this aspect of the spectral function in more detail. The large deviations from the free spectral functions found in the scalar channel cannot be sufficiently explained by HTL medium effects like thermal quark masses and Landau damping [91]. In the (pseudo-)scalar channel this leads to the conclusion that the behavior in the deconfined plasma phase is characterized by strongly correlated quarks and gluons in the temperature range up to 3 T_c. The QCD-TARO collaboration [16] reported similar findings in a recent lattice simulation with Wilson fermions on anisotropic lattices. Since they have used smeared meson propagators the results however might be strongly influenced by the continuum contributions and might project on unphysical ground states as shown in the end of section 4.7.2 with the application of the fuzzing technique for the free meson spectral function.

The temperature dependence of the obtained correlation functions can be investigated more directly after normalizing them with the corresponding free meson correlator on the lattice. Such ratios are displayed in figure 4.20 for the pseudo-scalar, scalar and vector channel and the same quark masses as described before. At low temperatures they can be compared to previous investigations with Wilson fermions [92] and overlap fermions [110] as well as to predictions of the interacting instanton liquid model [111] for $T < T_c$. In general a good qualitative agreement with the reported results can be observed in all channels. The deviations from one at time $\tau = 0$ could be reduced by taking the (non-)perturbative renormalization factors into account. Since the Z-factors are only available in the chiral limit, they cannot be obtained for the correlators below the critical temperature. In order to allow a comparison of the correlator ratios for

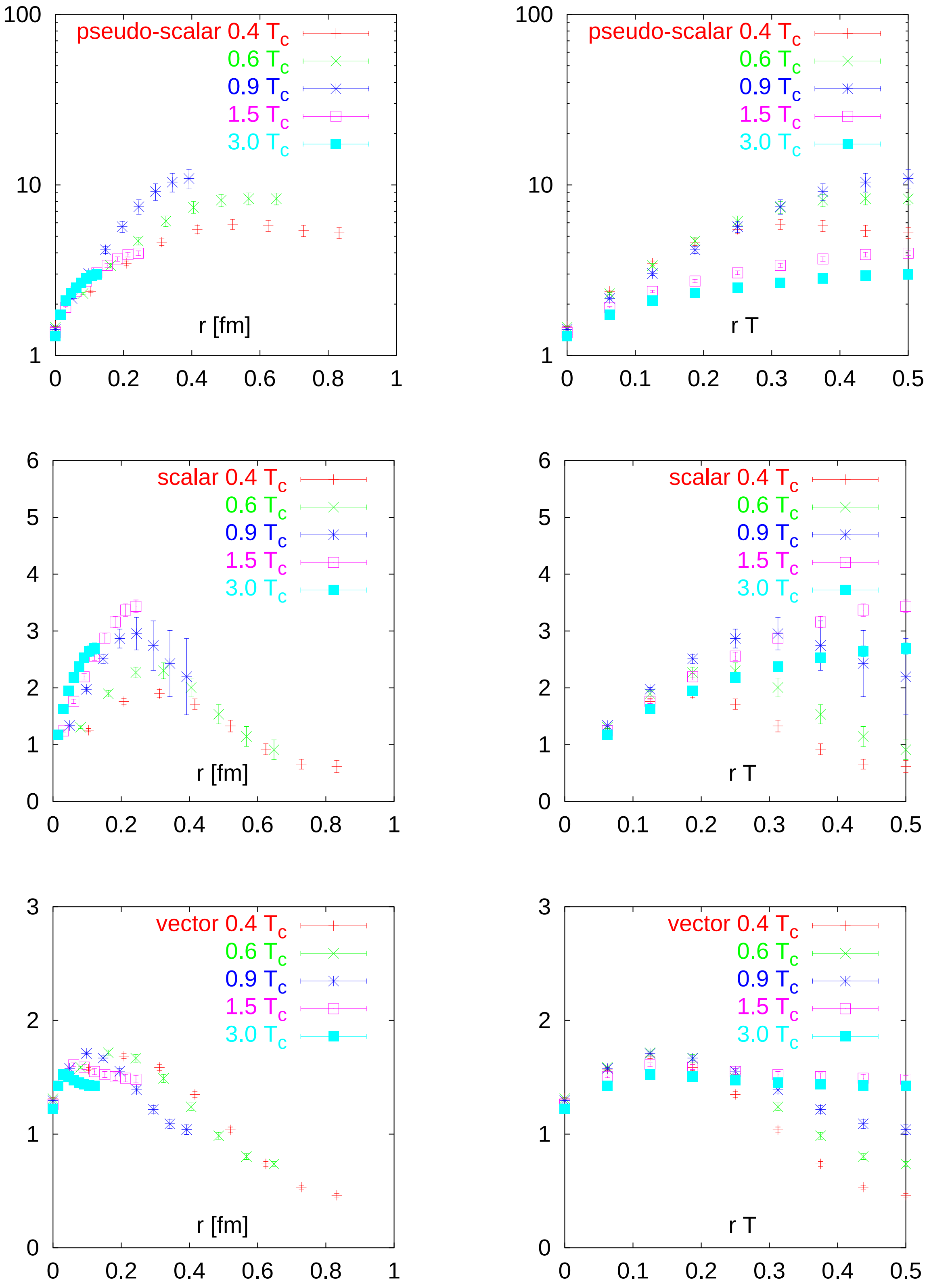

Figure 4.20: Ratio of meson and free thermal meson correlator on the lattice.

different temperatures no renormalization factors were used in figure 4.20. In the following the correlators will be referred to as attractive if the ratio is larger than one, while a ratio smaller than one corresponds to a repulsive interaction. Such an interpretation is inspired by the operator product expansion of these ratios presented in [112].

In the **pseudo-scalar channel** the strong attractive interaction between the quarks is visible in the steep rise of the ratio (note the logarithmic scale), which reflects the property of the pion as Goldstone boson below T_c. The flattening of the ratio at larger distances could also be observed in [110] at a similar value of the quark mass ($m_\pi/m_\rho \simeq 0.75$). Above the critical temperature the ratio is considerably decreased but still well above one, which confirms the expectations of the instanton liquid model [111]. Such a behavior indicates the persistent attractive interaction in this channel even above T_c as already observed in the analysis of the corresponding spectral function. Note that at such high temperatures mainly the short distance behavior of the correlators can be investigated, since the extent of the temporal direction shrinks with increasing temperature, which is obvious from the left panels of figure 4.20.

The situation is clearly different in the **scalar channel**. Apart from a weak attractive interaction similar to the pseudo-scalar channel at small distances the general behavior below T_c can be characterized by a strong repulsion in the range $r \simeq 0.3 - 0.9 fm$, which was also found in [92]. The strength of the repulsive interaction is increasingly reduced when approaching the critical temperature. Above T_c the ratio is very similar to the one in the pseudo-scalar channel, indicating the restoration of the chiral symmetry (see sec. 1.2). This phenomenon is further explored below in terms of the spectral functions.

Although the ratio in the **vector channel** looks similar to the scalar ratio at low temperatures, it remains much closer to one (note the different scale). The ratio flattens even more with increasing temperature and reaches almost a constant at 3 T_c. This behavior is consistent with the picture of a rapidly melting resonance contribution [111], indicating the free propagation of the quarks at $T > T_c$ described solely by the continuum contribution, which is in accordance with the analysis of the vector meson spectral functions at 1.5 and 3 T_c in figure 4.19 and the respective annotations.

Chiral symmetry restoration in the (pseudo-)scalar channel

Finally a somewhat closer look is addressed to the development of the (pseudo-)scalar correlation and spectral function for increasing temperature. For a simulation with dynamical quarks it is expected that the pseudo-scalar (π) and scalar (δ) correlators become degenerate at the critical temperature if the axial $U_A(1)$ symmetry is effectively restored (see sec. 1.2). The correlators and spectral functions are shown in figure 4.21 for nearly equal quark masses at 0.6 and 0.9 T_c as well as for almost zero quark mass at 1.5 T_c. The behavior of the correlation functions at 0.6 T_c resembles the behavior at zero temperature. A clear pion ground state peak can be observed in the corresponding spectral function of the pseudo-scalar meson, while the one of the scalar meson is characterized by a much broader continuum-like structure.

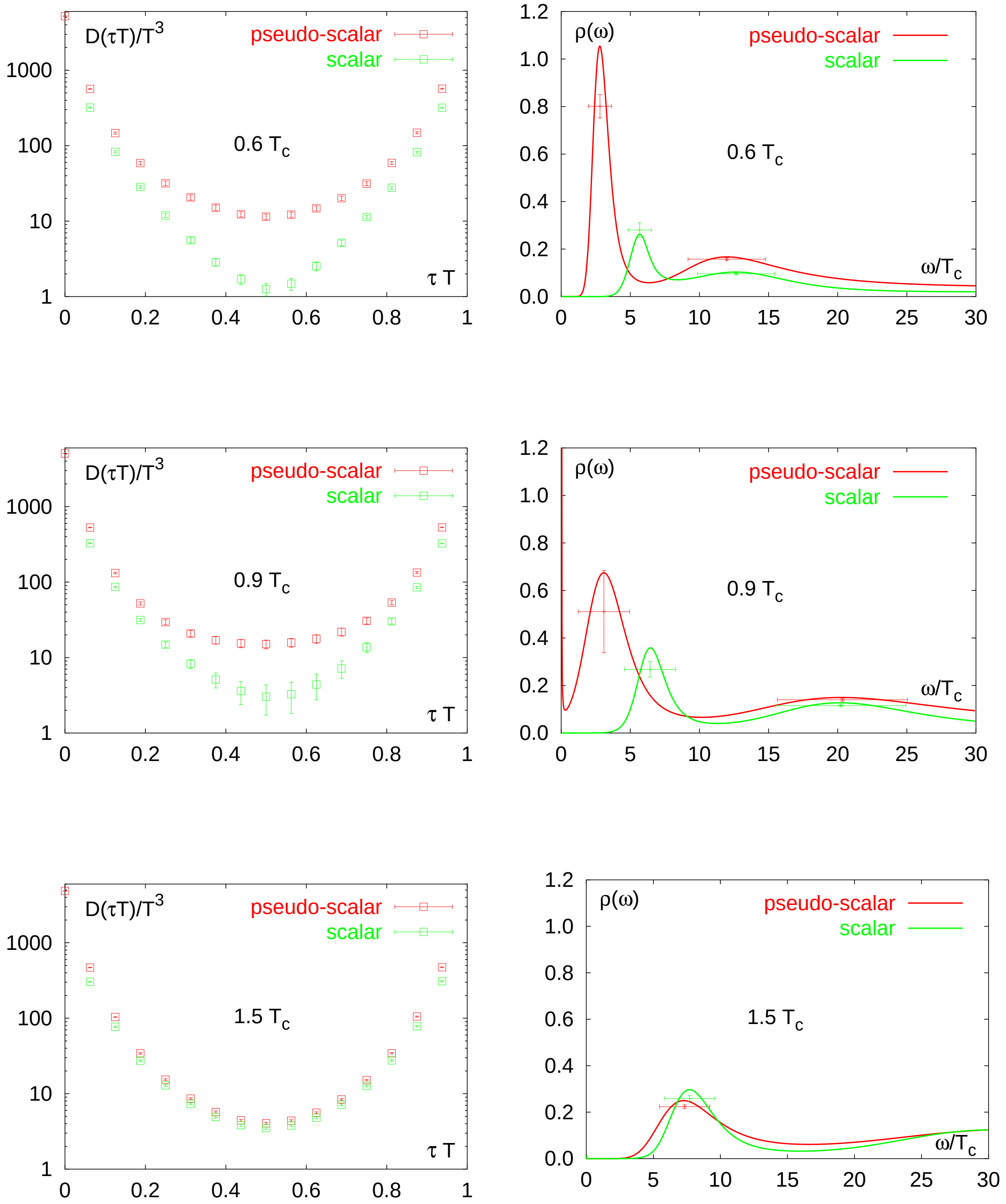

Figure 4.21: Restauration of the chiral symmetry between the scalar and pseudo-scalar meson (error bars indicate statistical errors obtained in a Jackknife analysis).

At 0.9 T_c first changes of the scalar correlator can be recognized, since the values around $\tau T = 0.5$ are increased and approach the pseudo-scalar correlation function. The scalar spectral function remains essentially the same, while the ground state peak of the pseudo-scalar spectral function broadens and is reduced in height. Above the critical temperature at 1.5 T_c the pseudo-scalar and scalar correlator are very similar. One therefore can observe the restoration of the chiral symmetry already in the quenched spectrum calculations. The degeneracy of the (pseudo-)scalar mesons is also reflected in the corresponding spectral functions which show a good agreement. Since only the correlators for the flavor non-singlets mesons π and δ were calculated in the present lattice simulations the observed chiral symmetry restoration at 1.5 T_c actually refers to the axial $U_A(1)$ symmetry in the (pseudo-)scalar channel. Predictions about the $SU(N_f)_L \times SU(N_f)_R$ chiral symmetry restoration could be obtained in simulating the flavor singlet mesons σ and η', which would involve the calculation of disconnected propagators. Such investigations are still at an exploratory stage [113, 114], since the signal is hidden in a high level of statistical noise and thus requires the application of stochastic variance reduction techniques.

Outlook on future applications

The quark and gluon propagators above the critical temperature calculated with the gauge field configurations in Coulomb gauge (see table 4.2) are currently under investigation. Preliminary results obtained for temporal correlators at zero and finite momenta will be presented in the near future [115]. Although the propagators are quite noisy MEM is capable to extract the position of the poles. In addition it would be desirable to explore their properties in other gauges, e.g. the Landau gauge, where the propagators are less influenced by the statistical noise. Such a study would require the adaptation of MEM for non-positive spectral functions. First suggestions for modified versions of the entropy (4.9) were reported recently [116].

Another interesting field of application for MEM would be lattice simulations in full QCD. In this case the properties of the peaks in the reconstructed spectral functions are directly related to the resonance widths and decay constants in experimental spectra, such as $\rho \to \pi\pi$. For this purpose it is mandatory to understand the non-zero width of the ground state peaks obtained in the MEM analysis of quenched lattice data. It is evident from the present investigation that insufficient statistics and a limited temporal extent of the lattice influence the height and width of the peaks considerably. A more quantitative analysis of these dependencies is certainly still needed in quenched lattice QCD calculations before one can proceed to QCD simulations with light dynamical quarks.

Conclusions

Two aspects of QCD were considered in the present thesis. In the first part the strange hadron spectrum was investigated, which was calculated in quenched QCD on four different lattice sizes covering a large physical volume of $(1.4 - 4.2\ \mathrm{fm})^3 \times 5.3$ fm. Strong finite size effects could be observed for the smallest lattice, which was manifest in overestimated hadron masses especially for the strange baryons and the H-dibaryon.

A good agreement of the strange hadron masses could be found on the three larger lattices. Compared to experimental values the obtained K^*, Σ and Λ masses show a maximal deviation below 10%, dependent on the particle used to set the physical scale. Such a behavior is common for simulations in the quenched approximation.

The mass of the H-dibaryon is compatible with twice the mass of the Λ baryon on all investigated lattice sizes. Moreover a quantitative agreement with previous studies on a similarly large lattice could be reached. No evidence for a bound H-dibaryon is apparent from the current calculations in quenched QCD, therefore such six quark state may be considered as unbound assembly of two Λ baryons.

The experience gained with the spectrum calculations at $T = 0$ also form the basis for studies of the hadron spectrum at finite temperature, which has been performed in the second part of this thesis. An essential new feature of this study is the application of the Maximum Entropy Method, which made an investigation of hadron spectral functions obtained from correlators on the lattice possible for the first time. This approach included the implementation, test and application of the method for the spectral analysis of hadron correlation functions in the vacuum as well as in a thermal medium.

For the meson correlators at zero temperature it could be demonstrated that the position of the pole mass is reproduced correctly in the corresponding spectral function. Moreover, the application of MEM yields useful additional information in comparison to conventional exponential fits as is evident from the analysis of the diquark correlators. The color anti-triplet diquark states exhibit similar clean ground state peaks as the mesons, but for the color sextet diquarks the continuum contribution dominates the spectral function, which explains the severe problems observed in fits with two exponentials.

The applicability of MEM for finite temperature correlation functions was examined for the first time. It could be shown for the free thermal meson correlator that the continuum structure is indeed reproducible. For the analysis of the thermal correlation function calculated on the lattice a specially adapted lattice kernel is required to absorb the cut-off effects.

The investigation of pole and screening masses obtained from temporal and spatial correlators revealed that MEM is capable to extract the correct pole mass value even when the conventional exponential fits tend to overestimate the mass due to the short extent of the time direction in simulations at finite temperature. The spectral representation facilitates the distinction between the pole and continuum contributions, which makes the MEM analysis superior to conventional fit methods.

At the lowest investigated temperatures 0.4 and 0.6 T_c the properties of the meson spectral functions remain qualitatively the same as at zero temperature. Deviations of the spectral shape can be explained by the short extent of the time direction and limited statistics. First changes in the spectral functions like a broadening of the peaks and a shift towards higher masses could be observed at 0.9 T_c in the vector channel. Whether this effect persists with larger statistics is still unclear and should be further clarified on larger lattices with reduced finite volume and cut-off effects.

The spectral function of the scalar meson is dominated by the continuum contribution at low temperatures, which might indicate that no bound state exists in this channel at least at low temperatures. At 0.9 T_c the scalar correlator approaches already the one of the pseudo-scalar meson, giving first evidence of chiral symmetry restoration. Finally at 1.5 T_c the spectral functions in the (pseudo-)scalar channel are almost perfectly in agreement. This observation leads to the prediction that the $U_A(1)$ symmetry between the π and δ meson gets approximately restored in this temperature range.

At the highest temperature of 3 T_c the behavior of the correlation and spectral functions in the vector channel are comparable with the propagation of almost free quarks. Only a slight enhancement is visible at large time separations and correspondingly small frequencies. In contrast to that considerable deviations from the free spectral function can be observed in the (pseudo-)scalar channel. A broad bump in the low energy regime still persists at 1.5 and even 3 T_c, indicating only a gradual approach towards the free quark behavior. The spectral functions obtained with MEM confirm the earlier findings in lattice simulations and are in qualitative agreement with the predictions of the interacting instanton liquid model. On a more quantitative level their structure cannot be sufficiently explained by medium effects taken into account in HTL-resummed perturbation theory.

In this exploratory application of the Maximum Entropy Method at finite temperature it could clearly be shown that such an analysis of lattice correlators leads to new insights into the thermal modification of hadronic properties. MEM provides a sensitive tool to study thermal effects in hadron spectra without making a priori assumptions on the spectral shapes. Nevertheless, more statistics and larger lattices are needed to gain more experience with this new approach. Furthermore it would be desirable to study the interacting physical medium effects more quantitatively.

Appendix A

Conventions

Dirac Matrices

The euclidian γ matrices in the non-relativistic representation are selfadjoint ($\gamma_\mu = \gamma_\mu^\dagger$) and obey the anti-commutation relation $\{\gamma_\nu, \gamma_\nu\} = 2\delta_{\mu\nu}$.

$$\gamma_1 = \begin{pmatrix} 0 & 0 & 0 & i \\ 0 & 0 & i & 0 \\ 0 & -i & 0 & 0 \\ -i & 0 & 0 & 0 \end{pmatrix} \quad \gamma_2 = \begin{pmatrix} 0 & 0 & 0 & 1 \\ 0 & 0 & -1 & 0 \\ 0 & -1 & 0 & 0 \\ 1 & 0 & 0 & 0 \end{pmatrix} \quad \gamma_3 = \begin{pmatrix} 0 & 0 & i & 0 \\ 0 & 0 & 0 & -i \\ -i & 0 & 0 & 0 \\ 0 & i & 0 & 0 \end{pmatrix}$$

$$\gamma_4 = \begin{pmatrix} 1 & 0 & 0 & 0 \\ 0 & 1 & 0 & 0 \\ 0 & 0 & -1 & 0 \\ 0 & 0 & 0 & -1 \end{pmatrix} \quad \gamma_5 = \begin{pmatrix} 0 & 0 & 1 & 0 \\ 0 & 0 & 0 & 1 \\ 1 & 0 & 0 & 0 \\ 0 & 1 & 0 & 0 \end{pmatrix} \quad = \quad \gamma_1\gamma_2\gamma_3\gamma_4$$

Charge Conjugation Matrix

For the diquark, baryon and dibaryon operators the charge conjugation matrix C is needed in combination with γ_5 to ensure the appropriate combination of the spinor indices (see section 3.2).

$$C = \begin{pmatrix} 0 & 0 & 0 & 1 \\ 0 & 0 & -1 & 0 \\ 0 & 1 & 0 & 0 \\ -1 & 0 & 0 & 0 \end{pmatrix} \quad = \quad \gamma_4\gamma_2 \quad = \quad -\gamma_1\gamma_3\gamma_5$$

$$C\gamma_5 = \begin{pmatrix} 0 & 1 & 0 & 0 \\ -1 & 0 & 0 & 0 \\ 0 & 0 & 0 & 1 \\ 0 & 0 & -1 & 0 \end{pmatrix}$$

Appendix B

Numerical Results

K-Meson

$\kappa_u \backslash \kappa_s$	0.147	0.146	0.145	0.1425	0.140
0.146	0.510(6)	0.550(5)	0.588(5)	0.678(5)	0.760(4)
0.147	0.467(6)	0.510(6)	0.552(5)	0.644(5)	0.730(4)
0.1475	0.443(6)	0.490(6)	0.532(6)	0.628(5)	0.715(5)
0.149	0.366(15)	0.424(15)	0.472(14)	0.575(12)	0.667(10)

K*-Meson

$\kappa_u \backslash \kappa_s$	0.147	0.146	0.145	0.1425	0.140
0.146	0.752(14)	0.776(12)	0.800(10)	0.859(8)	0.917(7)
0.147	0.728(17)	0.752(14)	0.776(12)	0.836(10)	0.895(8)
0.1475	0.717(18)	0.739(15)	0.763(14)	0.824(11)	0.884(10)
0.149	0.683(34)	0.703(29)	0.727(25)	0.790(20)	0.852(18)

Sigma-Baryon

$\kappa_u \backslash \kappa_s$	0.147	0.146	0.145	0.1425	0.140
0.146	1.15(3)	1.17(2)	1.20(2)	1.28(2)	1.35(1)
0.147	1.09(3)	1.12(3)	1.15(3)	1.23(2)	1.30(2)
0.1475	1.06(4)	1.09(3)	1.13(3)	1.20(2)	1.27(2)
0.149	0.98(7)	1.01(6)	1.05(5)	1.13(4)	1.20(3)

Lambda-Baryon

$\kappa_u \backslash \kappa_s$	0.147	0.146	0.145	0.1425	0.140
0.146	1.15(3)	1.17(3)	1.20(3)	1.26(3)	1.33(2)
0.147	1.09(4)	1.12(4)	1.15(3)	1.21(3)	1.27(3)
0.1475	1.06(4)	1.09(4)	1.11(4)	1.17(4)	1.24(4)
0.149	0.98(8)	1.01(7)	1.03(7)	1.09(7)	1.15(7)

H-Dibaryon

$\kappa_u \backslash \kappa_s$	0.147	0.146	0.145	0.1425	0.140*
0.146	2.45(18)	2.49(12)	2.54(10)	2.61(8)	2.70(15)
0.147	2.54(36)	2.52(29)	2.50(21)	2.53(12)	2.54(24)
0.1475	2.72(67)	2.60(46)	2.60(39)	2.61(21)	2.59(43)
0.149	2.83(88)	2.64(65)	2.52(51)	2.48(30)	2.33(60)

* extrapolated values

Table B.1: Particle masses on the $8^3 \times 30$ lattice (120 configurations).

K-Meson

$\kappa_u \backslash \kappa_s$	0.147	0.146	0.145	0.1425	0.140*
0.146	0.479(5)	0.521(5)	0.560(4)	0.651(4)	0.733(6)
0.147	0.432(5)	0.479(5)	0.521(5)	0.617(4)	0.702(6)
0.1475	0.407(5)	0.456(5)	0.501(5)	0.599(5)	0.687(6)
0.149	0.321(14)	0.383(12)	0.435(11)	0.544(11)	0.640(14)

K*-Meson

$\kappa_u \backslash \kappa_s$	0.147	0.146	0.145	0.1425	0.140*
0.146	0.735(13)	0.758(11)	0.781(9)	0.838(7)	0.899(12)
0.147	0.712(15)	0.735(13)	0.758(11)	0.817(7)	0.878(14)
0.1475	0.702(16)	0.723(14)	0.746(12)	0.805(8)	0.865(14)
0.149	0.668(30)	0.690(26)	0.713(22)	0.772(15)	0.833(28)

Sigma-Baryon

$\kappa_u \backslash \kappa_s$	0.147	0.146	0.145	0.1425	0.140*
0.146	1.09(2)	1.13(1)	1.16(1)	1.24(1)	1.33(2)
0.147	1.02(2)	1.06(2)	1.10(2)	1.18(1)	1.28(2)
0.1475	0.98(3)	1.02(2)	1.06(2)	1.15(2)	1.25(3)
0.149	0.86(4)	0.92(4)	0.96(4)	1.06(3)	1.17(5)

Lambda-Baryon

$\kappa_u \backslash \kappa_s$	0.147	0.146	0.145	0.1425	0.140*
0.146	1.10(2)	1.14(2)	1.16(2)	1.23(2)	1.31(3)
0.147	1.03(2)	1.07(2)	1.10(2)	1.17(2)	1.26(3)
0.1475	0.98(3)	1.02(2)	1.06(2)	1.13(2)	1.22(3)
0.149	0.86(5)	0.91(4)	0.96(4)	1.04(4)	1.15(7)

H-Dibaryon

$\kappa_u \backslash \kappa_s$	0.147	0.146	0.145	0.1425	0.140*
0.146	2.22(9)	2.28(8)	2.34(7)	2.49(5)	2.65(9)
0.147	2.16(13)	2.21(12)	2.25(10)	2.37(5)	2.49(10)
0.1475	2.10(16)	2.13(13)	2.18(12)	2.30(6)	2.42(12)
0.149	2.00(27)	2.01(23)	2.04(21)	2.12(11)	2.20(22)

Table B.2: Particle masses on the $12^3 \times 30$ lattice (60 configurations).

K-Meson

$\kappa_u \backslash \kappa_s$	0.147	0.146	0.145	0.1425	0.140
0.146	0.481(4)	0.523(3)	0.562(3)	0.654(3)	0.737(3)
0.147	0.435(4)	0.481(4)	0.524(4)	0.620(4)	0.706(4)
0.1475	0.410(4)	0.459(4)	0.503(4)	0.602(4)	0.690(4)
0.149	0.327(11)	0.387(10)	0.438(9)	0.547(9)	0.641(9)

K*-Meson

$\kappa_u \backslash \kappa_s$	0.147	0.146	0.145	0.1425	0.140
0.146	0.730(7)	0.754(7)	0.778(6)	0.837(6)	0.895(5)
0.147	0.704(8)	0.730(7)	0.754(7)	0.815(6)	0.874(6)
0.1475	0.690(8)	0.716(8)	0.742(7)	0.803(7)	0.862(7)
0.149	0.652(15)	0.680(15)	0.707(13)	0.770(13)	0.830(13)

Sigma-Baryon

$\kappa_u \backslash \kappa_s$	0.147	0.146	0.145	0.1425	0.140
0.146	1.06(1)	1.09(1)	1.12(1)	1.20(1)	1.27(1)
0.147	0.99(2)	1.02(1)	1.06(1)	1.14(1)	1.22(1)
0.1475	0.95(2)	0.98(2)	1.02(2)	1.11(2)	1.19(2)
0.149	0.84(3)	0.88(3)	0.93(3)	1.02(3)	1.10(3)

Lambda-Baryon

$\kappa_u \backslash \kappa_s$	0.147	0.146	0.145	0.1425	0.140
0.146	1.06(1)	1.09(1)	1.13(1)	1.20(1)	1.27(1)
0.147	0.99(2)	1.02(2)	1.06(2)	1.14(1)	1.21(1)
0.1475	0.95(2)	0.98(2)	1.02(2)	1.10(2)	1.17(2)
0.149	0.84(4)	0.88(4)	0.92(3)	1.01(3)	1.08(3)

H-Dibaryon

$\kappa_u \backslash \kappa_s$	0.147	0.146	0.145	0.1425	0.140*
0.146	2.17(9)	2.24(9)	2.34(8)	2.49(7)	2.68(12)
0.147	1.95(11)	2.06(10)	2.14(9)	2.33(7)	2.55(12)
0.1475	1.78(15)	1.91(12)	2.02(10)	2.24(7)	2.50(13)
0.149	1.45(25)	1.63(22)	1.72(19)	2.00(14)	2.31(26)

Table B.3: Particle masses on the $16^3 \times 30$ lattice (57 configurations).

K-Meson

$\kappa_u \backslash \kappa_s$	0.1475	0.146	0.145	0.1425	0.140*
0.146	0.458(6)	0.522(6)	0.561(6)	0.654(6)	0.735(8)
0.1475	0.384(6)	0.458(6)	0.503(6)	0.602(6)	0.690(8)
0.148	0.355(6)	0.435(6)	0.482(6)	0.585(6)	0.675(8)
0.149	0.291(10)	0.385(9)	0.438(9)	0.548(9)	0.644(11)

K*-Meson

$\kappa_u \backslash \kappa_s$	0.1475	0.146	0.145	0.1425	0.140*
0.146	0.705(16)	0.743(12)	0.768(11)	0.828(9)	0.892(16)
0.1475	0.662(19)	0.705(16)	0.732(16)	0.796(15)	0.867(25)
0.148	0.647(19)	0.692(19)	0.720(19)	0.785(19)	0.860(30)
0.149	0.619(25)	0.667(23)	0.696(22)	0.765(22)	0.843(35)

Sigma-Baryon

$\kappa_u \backslash \kappa_s$	0.1475	0.146	0.145	0.1425	0.140*
0.146	1.05(2)	1.10(2)	1.13(2)	1.21(2)	1.29(3)
0.1475	0.96(2)	1.02(2)	1.05(2)	1.13(2)	1.23(3)
0.148	0.92(2)	0.99(2)	1.03(2)	1.11(2)	1.21(3)
0.149	0.86(2)	0.93(2)	0.97(2)	1.06(2)	1.17(4)

Lambda-Baryon

$\kappa_u \backslash \kappa_s$	0.1475	0.146	0.145	0.1425	0.140*
0.146	1.07(2)	1.10(2)	1.13(2)	1.20(2)	1.27(3)
0.1475	0.96(2)	1.00(2)	1.03(2)	1.09(2)	1.16(3)
0.148	0.92(2)	0.96(2)	0.98(2)	1.05(2)	1.12(3)
0.149	0.85(2)	0.89(2)	0.92(2)	0.98(2)	1.05(4)

H-Dibaryon

$\kappa_u \backslash \kappa_s$	0.1475	0.146	0.145	0.1425	0.140*
0.146	2.25(8)	2.35(7)	2.42(6)	2.58(5)	2.75(9)
0.1475	2.05(12)	2.17(10)	2.22(8)	2.37(8)	2.54(13)
0.148	1.97(13)	2.08(11)	2.14(10)	2.28(9)	2.44(15)
0.149	1.84(16)	1.97(14)	2.01(12)	2.15(11)	2.30(18)

Table B.4: Particle masses on the $24^3 \times 30$ lattice (20 configurations).

$8^3 \times 30$ lattice (120 configurations)

	Λ input $\kappa_s = 0.1464$	Σ input $\kappa_s = 0.1442$	K^* input $\kappa_s = 0.1420$	mean $\kappa_s = 0.1417$
H	2976(450)	2852(267)	2725(283)	2708(304)
2Λ	[2231(103)]	2344(74)	2460(90)	2476(95)
Σ	1120(39)	[1193(26)]	1269(24)	1279(24)
K^*	774(20)	833(13)	[894(12)]	902(13)
K	446(10)	564(6)	663(7)	676(8)

$12^3 \times 30$ lattice (60 configurations)

	Λ input $\kappa_s = 0.1437$	Σ input $\kappa_s = 0.1423$	K^* input $\kappa_s = 0.1413$	mean $\kappa_s = 0.1417$
H	2326(92)	2371(101)	2405(128)	2391(115)
2Λ	[2231(46)]	2355(62)	2446(79)	2407(72)
Σ	1126(19)	[1193(23)]	1243(29)	1222(27)
K^*	830(11)	867(13)	[894(16)]	882(15)
K	551(6)	617(8)	661(9)	642(9)

$16^3 \times 30$ lattice (57 configurations)

	Λ input‡ $\kappa_s = 0.1425$	Σ input‡ $\kappa_s = 0.1411$	K^* input‡ $\kappa_s = 0.1412$	mean $\kappa_s = 0.1417$
H	2240(118)	2432(164)	2415(159)	2342(140)
2Λ	[2231(34)]	2343(44)	2333(43)	2290(38)
Σ	1132(18)	[1193(24)]	1188(24)	1164(21)
K^*	857(8)	897(10)	[894(10)]	878(9)
K	612(5)	673(7)	668(7)	645(6)

$24^3 \times 30$ lattice (20 configurations)

	Λ input‡ $\kappa_s = 0.1418$	Σ input‡ $\kappa_s = 0.1424$	K^* input‡ $\kappa_s = 0.1414$	mean $\kappa_s = 0.1417$
H	2445(97)	2405(85)	2477(108)	2452(100)
2Λ	[2231(47)]	2195(41)	2261(52)	2238(48)
Σ	1220(20)	[1193(18)]	1242(22)	1226(21)
K^*	878(19)	858(17)	[894(21)]	882(19)
K	641(7)	615(6)	662(7)	646(7)

$^\ddagger\kappa_s$-values averaged to mean value κ_s=0.1417(2)

Table B.5: Physical particle masses on all lattice sizes in $[MeV]$.

	MEM		2-exp. fit	
κ_{ud}	m_π	m_ρ	m_π	m_ρ
0.140	0.909(6)	1.025(3)	0.910(1)	1.025(2)
0.142	0.794(4)	0.930(3)	0.794(1)	0.932(2)
0.144	0.667(2)	0.836(4)	0.667(1)	0.836(3)
0.145	0.597(1)	0.788(4)	0.596(1)	0.787(4)
0.146	0.520(1)	0.738(10)	0.519(1)	0.739(7)
0.147	0.431(1)	0.675(19)	0.430(2)	0.688(15)
0.1475	0.380(1)	0.643(24)	0.379(2)	0.661(18)
0.148	0.318(1)	0.619(28)	0.316(3)	0.595(66)
κ_c		0.557(21)		0.579(18)

Table B.6: Comparison of meson masses obtained from MEM and two-exponential fits; vanishing pion mass m_π^2 at κ_c(MEM)=0.14922(1) and κ_c(exp)=0.14923(2).

	MEM				2-exp. fit			
κ_{ud}	$m_{\bar{3}0\bar{3}}$	$m_{61\bar{3}}$	$m_{\bar{3}16}$	m_{606}	$m_{\bar{3}0\bar{3}}$	$m_{61\bar{3}}$	$m_{\bar{3}16}$	m_{606}
0.140	1.18(2)	1.20(1)	1.33(1)	1.33(3)	1.19(1)	1.21(1)	1.33(3)	1.37(3)
0.142	1.07(1)	1.10(1)	1.22(3)	1.22(5)	1.08(1)	1.10(1)	1.10(16)	1.25(3)
0.144	0.95(2)	0.98(1)	1.06(5)	1.15(8)	0.96(1)	0.99(1)	0.97(13)	1.11(4)
0.145	0.89(1)	0.93(1)	0.97(6)	1.11(9)	0.90(2)	0.94(2)	0.92(14)	1.03(6)
0.146	0.83(1)	0.87(2)	0.96(5)	1.05(9)	0.84(2)	0.88(3)	0.86(14)	0.93(8)
0.147	0.76(1)	0.81(3)	0.88(6)	0.99(9)	0.77(2)	0.83(3)	0.82(12)	0.79(10)
0.1475	0.72(1)	0.79(4)	0.85(6)	0.98(11)	0.74(2)	0.81(4)	0.82(15)	0.69(13)
0.148	0.67(2)	0.77(3)	0.84(9)	0.96(15)	0.70(2)	0.81(5)	0.84(18)	0.60(37)
κ_c	0.60(2)	0.70(3)	0.77(8)	0.89(13)	0.62(2)	0.73(4)	0.77(17)	0.50(15)

Table B.7: Comparison of diquark masses obtained from MEM and two-exponential fits.

0.94 T_c, a=0.049 fm, a^{-1}=4.042 GeV, L=1.176 fm, N_C=120						
κ_{ud}	$m_\pi[a]$	$m_\pi[GeV]$	$m_\delta[a]$	$m_\delta[GeV]$	$m_\rho[a]$	$m_\rho[GeV]$
0.1330	0.442(7)	1.787(28)	0.591(14)	2.389(57)	0.523(5)	2.113(21)
0.1340	0.347(8)	1.403(33)	0.488(14)	1.972(57)	0.463(9)	1.873(38)
0.1346	0.281(11)	1.136(44)	0.422(14)	1.706(57)	0.424(13)	1.715(52)
0.1354	0.201(11)	0.812(44)	[0.429(35)]	[1.734(141)]	0.355(17)	1.437(68)
κ_c = 0.13589(8)			0.290(26)	1.172(105)	0.336(14)	1.360(55)

0.56 T_c, a=0.081 fm, a^{-1}=2.430 GeV, L=1.944 fm, N_C=60						
κ_{ud}	$m_\pi[a]$	$m_\pi[GeV]$	$m_\delta[a]$	$m_\delta[GeV]$	$m_\rho[a]$	$m_\rho[GeV]$
0.1330	0.473(11)	1.149(26)	0.697(35)	1.694(85)	0.562(8)	1.365(20)
0.1340	0.379(11)	0.921(26)	0.647(30)	1.572(73)	0.490(9)	1.190(22)
0.1346	0.311(12)	0.756(29)	0.634(26)	1.541(63)	0.446(12)	1.084(28)
0.1354	0.198(7)	0.481(18)	[0.737(41)]	[1.791(100)]	0.391(17)	0.951(41)
κ_c = 0.13592(5)			0.580(54)	1.409(131)	0.354(14)	0.860(35)

0.44 T_c, a=0.104 fm, a^{-1}=1.901 GeV, L=2.496 fm, N_C=60						
κ_{ud}	$m_\pi[a]$	$m_\pi[GeV]$	$m_\delta[a]$	$m_\delta[GeV]$	$m_\rho[a]$	$m_\rho[GeV]$
0.1324	0.506(7)	0.962(13)	0.718(53)	1.365(101)	0.649(12)	1.234(23)
0.1332	0.428(11)	0.814(21)	0.623(77)	1.184(146)	0.590(12)	1.121(23)
0.1342	0.315(16)	0.599(30)	0.468(98)	0.890(186)	0.512(15)	0.973(27)
0.1348	0.231(23)	0.439(44)	[0.240(140)]	[0.456(266)]	0.462(19)	0.878(36)
κ_c = 0.13541(13)			0.316(153)	0.601(291)	0.419(18)	0.797(34)

Table B.8: MEM results below T_c on the $24^3 \times 16$ lattice.

0.94 T_c, a=0.049 fm, a^{-1}=4.042 GeV, L=1.176 fm, N_C=120						
κ_{ud}	$m^t_\pi[a]$	$m^z_\pi[a]$	$m^t_\delta[a]$	$m^z_\delta[a]$	$m^t_\rho[a]$	$m^z_\rho[a]$
0.1330	0.481(7)	0.412(7)	0.598(28)	0.543(18)	0.528(9)	0.452(7)
0.1340	0.397(8)	0.326(8)	0.543(22)	0.438(16)	0.474(9)	0.378(6)
0.1346	0.356(8)	0.273(8)	0.462(18)	0.385(16)	0.440(10)	0.339(9)
0.1354	0.278(16)	0.177(17)	[0.648(92)]	[0.353(121)]	0.417(17)	0.284(15)
κ_c^z = 0.13592(11)			0.358(39)	0.255(31)	0.380(14)	0.246(12)

0.56 T_c, a=0.081 fm, a^{-1}=2.430 GeV, L=1.944 fm, N_C=60						
κ_{ud}	$m^t_\pi[a]$	$m^z_\pi[a]$	$m^t_\delta[a]$	$m^z_\delta[a]$	$m^t_\rho[a]$	$m^z_\rho[a]$
0.1330	0.526(17)	0.488(3)	0.763(21)	0.716(26)	0.603(11)	0.572(7)
0.1340	0.440(8)	0.398(5)	0.703(23)	0.622(35)	0.549(12)	0.506(11)
0.1346	0.368(11)	0.337(6)	0.680(30)	0.579(47)	0.497(12)	0.464(10)
0.1354	0.269(12)	0.237(9)	[0.719(49)]	[0.695(107)]	0.462(21)	0.424(21)
κ_c^z = 0.13613(6)			0.599(52)	0.442(78)	0.411(19)	0.369(16)

0.44 T_c, a=0.104 fm, a^{-1}=1.901 GeV, L=2.496 fm, N_C=60						
κ_{ud}	$m^t_\pi[a]$	$m^z_\pi[a]$	$m^t_\delta[a]$	$m^z_\delta[a]$	$m^t_\rho[a]$	$m^z_\rho[a]$
0.1324	0.557(13)	0.534(5)	0.769(47)	0.733(52)	0.679(13)	0.637(6)
0.1332	0.477(14)	0.458(5)	0.721(51)	0.633(81)	0.621(8)	0.576(7)
0.1342	0.362(15)	0.342(6)	0.704(70)	0.545(167)	0.548(10)	0.495(14)
0.1348	0.273(12)	0.254(8)	[0.638(189)]	[0.808(101)]	0.506(12)	0.453(31)
κ_c^z = 0.13551(5)			0.645(116)	0.387(226)	0.456(13)	0.398(18)

Table B.9: Two-exponential fit results below T_c on the $24^3 \times 16$ lattice.

Temperature	β-value	Z_{PS}	Z_V
1.5 T_c	6.872	0.7523	0.8292
3.0 T_c	7.457	0.7833	0.8512

Table B.10: Renormalization factors calculated non-perturbatively for the vector channel and in tadpole-improved perturbation theory ($c_{SW} = 1$) for the pseudo-scalar channel [108, 109].

Bibliography

[1] H. Meyer-Ortmanns, "Phase transitions in quantum chromodynamics", *Rev. Mod. Phys.* **68** (1996) 473–598.

[2] F. Karsch and M. Lütgemeier, "Deconfinement and chiral symmetry restoration in an SU(3) gauge theory with adjoint fermions", *Nucl. Phys.* **B550** (1999) 449–464, `hep-lat/9812023`.

[3] M. Fukugita, M. Okawa, and A. Ukawa, "Finite size scaling study of the deconfining phase transition in pure SU(3) lattice gauge theory", *Nucl. Phys.* **B337** (1990) 181.

[4] B. Beinlich, F. Karsch, E. Laermann, and A. Peikert, "String tension and thermodynamics with tree level and tadpole improved actions", *Eur. Phys. J.* **C6** (1999) 133–140, `hep-lat/9707023`.

[5] F. Karsch, E. Laermann, A. Peikert, C. Schmidt, and S. Stickan, "Flavor and quark mass dependence of QCD thermodynamics", *Nucl. Phys. Proc. Suppl.* **94** (2001) 411–414, `hep-lat/0010040`.

[6] M. Stephanov, K. Rajagopal, and E. Shuryak, "Event-by-event fluctuations in heavy ion collisions and the QCD critical point", *Phys. Rev.* **D60** (1999) 114028.

[7] E. Laermann, "Chiral transition in 2 flavor staggered QCD", *Nucl. Phys. Proc. Suppl.* **60A** (1998) 180–187.

[8] R. D. Pisarski and F. Wilczek, "Remarks on the chiral phase transition in chromodynamics", *Phys. Rev.* **D29** (1984) 338.

[9] G. Boyd, F. Karsch, E. Laermann, and M. Oevers, "Two flavour QCD phase transition", `hep-lat/9607046`.

[10] J. B. Kogut, J. F. Lagae, and D. K. Sinclair, "Topology, fermionic zero modes and flavor singlet correlators in finite temperature QCD", *Phys. Rev.* **D58** (1998) 054504, `hep-lat/9801020`.

[11] R. V. Gavai, S. Gupta, and R. Lacaze, "Quenched QCD at finite temperature with chiral fermions", `hep-lat/0107022`.

[12] P. Vranas, "Dynamical lattice QCD thermodynamics and the U(1)A symmetry with domain wall fermions", `hep-lat/9903024`.

[13] G. Boyd *et al.*, "Hadron properties just before deconfinement", *Phys. Lett.* **B349** (1995) 170–176, `hep-lat/9501029`.

[14] E. Laermann and P. Schmidt, "Meson screening masses at high temperature in quenched QCD with improved Wilson quarks", `hep-lat/0103037`.

[15] C. DeTar and J. B. Kogut, "Measuring the hadronic spectrum of the quark plasma", *Phys. Rev.* **D36** (1987) 2828.

[16] **QCD-TARO** Collaboration, P. de Forcrand *et al.*, "Meson correlators in finite temperature lattice QCD", *Phys. Rev.* **D63** (2001) 054501, `hep-lat/0008005`.

[17] M. Jarrel and J. E. Gubernatis, "Bayesian inference and the analytic continuation of imaginary-time quantum Monte Carlo data", *Phys. Rep.* **269** (1996) 133–195.

[18] M. Asakawa, T. Hatsuda, and Y. Nakahara, "Maximum entropy analysis of the spectral functions in lattice QCD", *Prog. Part. Nucl. Phys.* **46** (2001) 459–508, `hep-lat/0011040`.

[19] M. A. Halasz, A. D. Jackson, R. E. Shrock, M. A. Stephanov, and J. J. M. Verbaarschot, "On the phase diagram of QCD", *Phys. Rev.* **D58** (1998) 096007.

[20] J. Pochodzalla *et al.*, "Probing the nuclear liquid - gas phase transition", *Phys. Rev. Lett.* **75** (1995) 1040.

[21] J. Bardeen, L. N. Cooper, and J. R. Schrieffer, "Theory of superconductivity", *Phys. Rev.* **108** (1957) 1175–1204.

[22] A. D. Rujula, H. Georgi, and S. L. Glashow, "Hadron masses in a gauge theory", *Phys. Rev.* **D12** (1975) 147–162.

[23] T. Schäfer, E. V. Shuryak, and J. J. M. Verbaarschot, "Baryonic correlators in the random instanton vacuum", *Nucl. Phys.* **B412** (1994) 143–168, `hep-ph/9306220`.

[24] R. Rapp, T. Schäfer, E. V. Shuryak, and M. Velkovsky, "Diquark Bose condensates in high density matter and instantons", *Phys. Rev. Lett.* **81** (1998) 53–56, `hep-ph/9711396`.

[25] D. Bailin and A. Love, "Superfluidity and superconductivity in relativistic fermion systems", *Phys. Rept.* **107** (1984) 325.

[26] M. Alford, K. Rajagopal, and F. Wilczek, "Color-flavor locking and chiral symmetry breaking in high density QCD", *Nucl. Phys.* **B537** (1999) 443.

[27] T. Schäfer and F. Wilczek, "Continuity of quark and hadron matter", *Phys. Rev. Lett.* **82** (1999) 3956–3959, `hep-ph/9811473`.

[28] E. Farhi and R. L. Jaffe, "Strange matter", *Phys. Rev.* **D30** (1984) 2379.

[29] C. Greiner and J. Schaffner-Bielich, “Physics of Strange Matter”, `nucl-th/9801062`.

[30] C. Alcock, E. Farhi, and A. Olinto, “Strange stars”, *Nucl. Phys. Proc. Suppl.* **24B** (1991) 93–102.

[31] E. Witten, “Cosmic separation of phases”, *Phys. Rev.* **D30** (1984) 272–285.

[32] W. Busza, R. L. Jaffe, J. Sandweiss, and F. Wilczek, “Review of speculative ’disaster scenarios’ at RHIC”, *Rev. Mod. Phys.* **72** (2000) 1125–1140, `hep-ph/9910333`.

[33] R. Jaffe, “Perhaps a stable dihyperon”, *Phys. Rev. Lett.* **38** (1977) 195–198.

[34] T. Sakai, K. Shimizu, and K. Yazaki, “H dibaryon”, *Prog. Theor. Phys. Suppl.* **137** (2000) 121, `nucl-th/9912063`.

[35] S. V. Bashinsky and R. L. Jaffe, “Quark states near a threshold and the unstable H-dibaryon”, *Nucl. Phys.* **A625** (1997) 167–191, `hep-ph/9705407`.

[36] P. B. Mackenzie and H. B. Thacker, “Evidence against a stable dibaryon from lattice QCD”, *Phys. Rev. Lett.* **55** (1985) 2539.

[37] Y. Iwasaki, T. Yoshie, and Y. Tsuboi, “The H dibaryon in lattice QCD”, *Phys. Rev. Lett.* **60** (1988) 1371–1374.

[38] T. Yoshie, Y. Iwasaki, and S. Sakai, “Hadron spectrum on a 24**3 x 60 lattice”, *Nucl. Phys. Proc. Suppl.* **17** (1990) 413–416.

[39] A. Pochinsky, J. W. Negele, and B. Scarlet, “Lattice study of the H dibaryon”, *Nucl. Phys. Proc. Suppl.* **B73** (1999) 255–257, `hep-lat/9809077`.

[40] I. Wetzorke, F. Karsch, and E. Laermann, “Further evidence for an unstable H-dibaryonΓ”, *Nucl. Phys. Proc. Suppl.* **83** (2000) 218–220, `hep-lat/9909037`.

[41] H. J. Rothe, “Lattice gauge theories: An introduction”,. Singapore, Singapore: World Scientific (1992) 381 p.

[42] I. Montvay and G. Münster, “Quantum fields on a lattice”,. Cambridge, UK: Univ. Pr. (1994) 491 p. (Cambridge monographs on mathematical physics).

[43] K. Symanzik, “Mathematical Problems in Theoretical Physics”, *Lecture notes in Physics*. Springer-Verlag, Berlin (1982) 153.

[44] **CP-PACS** Collaboration, S. Aoki *et al.*, “Quenched light hadron spectrum”, *Phys. Rev. Lett.* **84** (2000) 238–241, `hep-lat/9904012`.

[45] H. B. Nielsen and M. Ninomiya, “No go theorem for regularizing chiral fermions”, *Phys. Lett.* **B105** (1981) 219.

[46] B. Sheikholeslami and R. Wohlert, “Improved continuum limit lattice action for QCD with Wilson fermions”, *Nucl. Phys.* **B259** (1985) 572.

[47] M. Lüscher, S. Sint, R. Sommer, P. Weisz, and U. Wolff, "Non-perturbative O(a) improvement of lattice QCD", *Nucl. Phys.* **B491** (1997) 323–343, `hep-lat/9609035`.

[48] K. Jansen and R. Sommer, "The non-perturbative O(alpha) improved action for dynamical Wilson fermions", *Nucl. Phys. Proc. Suppl.* **63** (1998) 853–855, `hep-lat/9709022`.

[49] J. Kogut and L. Susskind, "Hamiltonian formulation of Wilson's lattice gauge theories", *Phys. Rev.* **D11** (1975) 395.

[50] P. H. Ginsparg and K. G. Wilson, "A remnant of chiral symmetry on the lattice", *Phys. Rev.* **D25** (1982) 2649.

[51] M. Lüscher, "Abelian chiral gauge theories on the lattice with exact gauge invariance", *Nucl. Phys.* **B549** (1999) 295–334, `hep-lat/9811032`.

[52] D. B. Kaplan, "A method for simulating chiral fermions on the lattice", *Phys. Lett.* **B288** (1992) 342–347, `hep-lat/9206013`.

[53] R. Narayanan and H. Neuberger, "A construction of lattice chiral gauge theories", *Nucl. Phys.* **B443** (1995) 305–385, `hep-th/9411108`.

[54] H. Neuberger, "Chiral fermions on the lattice", *Nucl. Phys. Proc. Suppl.* **83** (2000) 67–76, `hep-lat/9909042`.

[55] R. Gupta, "Introduction to lattice QCD", `hep-lat/9807028`.

[56] N. Metropolis, A. W. Rosenbluth, M. N. Rosenbluth, A. H. Teller, and E. Teller, "Equation of state calculations by fast computing machines", *J. Chem. Phys.* **21** (1953) 1087–1092.

[57] N. Cabibbo and E. Marinari, "A new method for updating SU(N) matrices in computer simulations of gauge theories", *Phys. Lett.* **B119** (1982) 387.

[58] A. D. Kennedy and B. J. Pendleton, "Improved heat bath method for Monte Carlo calculations in lattice gauge theories", *Phys. Lett.* **B156** (1985) 393.

[59] S. L. Adler, "An overrelaxation method for the Monte Carlo evaluation of the partition function for multiquadratic actions", *Phys. Rev.* **D23** (1981) 2901.

[60] M. Creutz, "Overrelaxation and Monte Carlo Simulation", *Phys. Rev.* **D36** (1987) 515.

[61] S. L. Eisenstat *et. al., J. Num. Anal.* **20** (1983) 345.

[62] Y. Oyanagi, "An incomplete LDU decomposition of lattice fermions and its application to conjugate residual methods", *Comp. Phys. Comm.* **42** (1986) 333.

[63] H. van der Vorst, *SIAM J. Sc. Stat. Comp.* **13** (1992) 631.

[64] M. R. Hestenes and E. Stiefel, *J. Res. Nat. Bur. Standards* **49** (1952) 409.

[65] A. Frommer, V. Hannemann, B. Nockel, T. Lippert, and K. Schilling, "Accelerating Wilson fermion matrix inversions by means of the stabilized biconjugate gradient algorithm", *Int. J. Mod. Phys.* **C5** (1994) 1073–1088, `hep-lat/9404013`.

[66] T. A. DeGrand and P. Rossi, "Conditioning techniques for dynamical fermions", *Comput. Phys. Commun.* **60** (1990) 211.

[67] L. Giusti, M. L. Paciello, C. Parrinello, S. Petrarca, and B. Taglienti, "Problems in Lattice Gauge Fixing", `hep-lat/0104012`.

[68] C. Bernard, D. Murphy, A. Soni, and K. Yee, "Lattice quark propagator in fixed gauges", *Nucl. Phys. Proc. Suppl.* **B17** (1990) 593–598.

[69] A. Cucchieri and T. Mendes, "Gauge fixing and gluon propagator in lambda-gauges", `hep-lat/9902024`.

[70] C. T. H. Davies *et al.*, "Fourier acceleration in lattice gauge theories. 1. Landau gauge fixing", *Phys. Rev.* **D37** (1988) 1581.

[71] P. de Forcrand and R. Gupta, "Multigrid Techniques for Quark Propagator", *Nucl. Phys. Proc. Suppl.* **B9** (1989) 516.

[72] R. Gupta *et al.*, "The hadron spectrum on a 18**3 x 42 lattice", *Phys. Rev.* **D36** (1987) 2813.

[73] J. E. Mandula and M. Ogilvie, "Efficient gauge fixing via overrelaxation", *Phys. Lett.* **B248** (1990) 156–158.

[74] I. Wetzorke, "Quarks, Diquarks und Hadronen in der Gitter QCD", *Diploma Thesis,* **Bielefeld** (1998).

[75] M. Hess, F. Karsch, E. Laermann, and I. Wetzorke, "Diquark Masses from Lattice QCD", *Phys. Rev.* **D58** (1998) 111502, `hep-lat/9804023`.

[76] C. Michael and A. McKerrell, "Fitting correlated hadron mass spectrum data", *Phys. Rev.* **D51** (1995) 3745–3750, `hep-lat/9412087`.

[77] J. F. Donoghue and K. S. Sateesh, "Diquark clusters in the quark gluon plasma", *Phys. Rev.* **D38** (1988) 360.

[78] L. Y. Glozman and D. O. Riska, "The spectrum of the nucleons and the strange hyperons and chiral dynamics", *Phys. Rept.* **268** (1996) 263–303, `hep-ph/9505422`.

[79] F. E. Close, "An Introduction to Quarks and Partons",. Academic Press, London (1979) 481 p.

[80] R. L. Jaffe, "Color, spin, and flavor-dependent forces in quantum chromodynamics", `hep-ph/0001123`.

[81] E. Golowich and T. Sotirelis, "O(alpha-s**2) mass contributions to the H dibaryon in a truncated bag model", *Phys. Rev.* **D46** (1992) 354–363.

[82] **CP-PACS** Collaboration, A. A. Khan *et al.*, "Light Hadron Spectroscopy with Two Flavors of Dynamical Quarks on the Lattice", `hep-lat/0105015`.

[83] R. Gupta, D. Daniel, and J. Grandy, "Bethe-salpeter amplitudes and density correlations for mesons with Wilson fermions", *Phys. Rev.* **D48** (1993) 3330–3339, `hep-lat/9304009`.

[84] **UKQCD** Collaboration, P. Lacock, A. McKerrell, C. Michael, I. M. Stopher, and P. W. Stephenson, "Efficient hadronic operators in lattice gauge theory", *Phys. Rev.* **D51** (1995) 6403–6410, `hep-lat/9412079`.

[85] **APE** Collaboration, M. Albanese *et al.*, "Glueball masses and string tension in lattice QCD", *Phys. Lett.* **B192** (1987) 163.

[86] S. Aoki, "Unquenched QCD simulation results", *Nucl. Phys. Proc. Suppl.* **94** (2001) 3–18, `hep-lat/0011074`.

[87] G. Boyd, S. Gupta, F. Karsch, and E. Laermann, "Spatial and temporal hadron correlators below and above the chiral phase transition", *Z. Phys.* **C64** (1994) 331–338, `hep-lat/9405006`.

[88] R. Rapp and J. Wambach, "Chiral symmetry restoration and dileptons in relativistic heavy-ion collisions", *Adv. Nucl. Phys.* **25** (2000) 1, `hep-ph/9909229`.

[89] H. Satz, "Colour deconfinement in nuclear collisions", *Rept. Prog. Phys.* **63** (2000) 1511.

[90] E. Braaten and R. D. Pisarski, "Soft amplitudes in hot gauge theories: A general analysis", *Nucl. Phys.* **B337** (1990) 569.

[91] F. Karsch, M. G. Mustafa, and M. H. Thoma, "Finite temperature meson correlation functions in HTL approximation", *Phys. Lett.* **B497** (2001) 249–258, `hep-ph/0007093`.

[92] M. C. Chu, J. M. Grandy, S. Huang, and J. W. Negele, "Correlation functions of hadron currents in the QCD vacuum calculated in lattice QCD", *Phys. Rev.* **D48** (1993) 3340–3353, `hep-lat/9306002`.

[93] D. B. Leinweber, "Testing QCD sum rule techniques on the lattice", *Phys. Rev.* **D51** (1995) 6369–6382, `nucl-th/9405002`.

[94] C. Allton and S. Capitani, "Study of lattice correlation functions at small times using the QCD sum rules continuum model", *Nucl. Phys.* **B526** (1998) 463–486, `hep-lat/9712006`.

[95] N. Wu, "The Maximum Entropy Method",. Springer-Verlag, Berlin (1997) 328 p.

[96] S. F. Gull, "Developments in Maximum Entropy Data Analysis", in *Maximum Entropy and Bayesian Methods* (Kluwer Academic Publishers, London, 1989) 53–71.

[97] M. Oevers, C. Davies, and J. Shigemitsu, “Towards the application of the maximum entropy method to finite temperature Upsilon spectroscopy”, *Nucl. Phys. Proc. Suppl.* **94** (2001) 423–426, `hep-lat/0009031`.

[98] **CP-PACS** Collaboration, T. Yamazaki *et al.*, “Spectral function and excited states in lattice QCD with maximum entropy method”, `hep-lat/0105030`.

[99] Y. Nakahara, M. Asakawa, and T. Hatsuda, “Hadronic spectral functions in lattice QCD”, *Phys. Rev.* **D60** (1999) 091503, `hep-lat/9905034`.

[100] J. Skilling, “Classic Maximum Entropy”, in *Maximum Entropy and Bayesian Methods* (Kluwer Academic Publishers, London, 1989) 45–52.

[101] R. K. Bryan, “Maximum entropy analysis of oversampled data problems”, *Eur. Biophys. J.* **18** (1990) 165–174.

[102] L. J. Reinders, H. Rubinstein, and S. Yazaki, “Hadron properties from QCD sum rules”, *Phys. Rept.* **127** (1985) 1.

[103] I. Wetzorke and F. Karsch, “Testing MEM with diquark and thermal meson correlation functions”, *Proceedings of the International Workshop on Strong and Electroweak Matter 2000 (Edt. C.P. Korthals-Altes)* **World Scientific** (2001) p.193, `hep-lat/0008008`.

[104] W. Florkowski and B. L. Friman, “Spatial dependence of meson correlation functions at high temperature”, *Z. Phys.* **A347** (1994) 271–276.

[105] F. Karsch, E. Laermann, P. Petreczky, S. Stickan, and I. Wetzorke, “Finite Temperature Meson Correlation Functions”, *in preparation.*

[106] T. Hatsuda, “Spectral change of hadrons and chiral symmetry”, `hep-ph/0104139`.

[107] M. Göckeler *et al.*, “Scaling of non-perturbatively O(a) improved Wilson fermions: Hadron spectrum, quark masses and decay constants”, *Phys. Rev.* **D57** (1998) 5562–5580, `hep-lat/9707021`.

[108] M. Göckeler *et al.*, “Perturbative renormalisation of bilinear quark and gluon operators”, *Nucl. Phys. Proc. Suppl.* **53** (1997) 896–898, `hep-lat/9608033`.

[109] M. Göckeler *et al.*, “Nonperturbative renormalisation of composite operators in lattice QCD”, *Nucl. Phys.* **B544** (1999) 699–733, `hep-lat/9807044`.

[110] T. DeGrand, “Short distance current correlators: Comparing lattice simulations to the instanton liquid”, `hep-lat/0106001`.

[111] T. Schäfer and E. V. Shuryak, “Hadronic correlation functions in the interacting instanton liquid”, *Phys. Rev.* **D54** (1996) 1099–1111, `hep-ph/9512384`.

[112] E. V. Shuryak, “Correlation functions in the QCD vacuum”, *Rev. Mod. Phys.* **65** (1993) 1–46.

[113] **SESAM** Collaboration, T. Struckmann *et al.*, “Flavor singlet pseudoscalar masses in N(f) = 2 QCD”, *Phys. Rev.* **D63** (2001) 074503, `hep-lat/0010005`.

[114] **UKQCD** Collaboration, C. McNeile and C. Michael, “The eta and eta’ mesons in QCD”, *Phys. Lett.* **B491** (2000) 123–129, `hep-lat/0006020`.

[115] P. Petreczky *et al.*, “Temporal quark and gluon propagators: measuring the quasiparticle masses”, *to appear in the proceedings of ’Lattice 2001’*.

[116] K. Langfeld, H. Reinhardt, and J. Gattnar, “Gluon propagators and quark confinement”, `hep-ph/0107141`.

Acknowledgements

Meinem Doktorvater Prof. Dr. Frithjof Karsch danke ich für die hervorragende Betreuung während der vier Jahre wissenschaftlicher Forschung, die zu meiner Diplomarbeit und schließlich zur vorliegenden Dissertation geführt haben. Besonders hervorheben möchte ich dabei seine ständige Diskussionsbereitschaft und die Anregungen und Ideen, die zum Gelingen dieser Arbeit beigetragen haben. Außerdem möchte ich Prof. Dr. Edwin Laermann für seine Bereitwilligkeit danken, sich jederzeit mit offenen Fragen auseinanderzusetzen und auftretenden Problemen auf den Grund zu gehen.

Weiterhin danke ich Peter Petreczky und insbesondere Sven Stickan für die optimale Zusammenarbeit im Rahmen unseres Projektes 'Finite Temperature Meson Correlation Functions'. Darüber hinaus sei den vielen früheren und heutigen Diplomanden und Doktoranden der Arbeitsgruppe gedankt, die die Mittags- und Kaffeepausen mit physikalischen und nicht-physikalischen Diskussionen bereichert haben. Nicht zuletzt ein Dankeschön an die Sektretärinnen Gundrun Eickmeyer und Susi von Reder, die ebenfalls zur angenehmen Arbeitsatmosphäre beigetragen haben.

Abschließend geht ein besonderer Dank an meine Eltern und meinen Bruder für die Unterstützung und Motivation während meines gesamten Studiums.